Thesis for the degree of Doctor of Philosophy
in the Natural Sciences

Microtubule structure and function as perturbed by electromagnetic fields

---

Greger Hammarin

UNIVERSITY OF GOTHENBURG

Department of Chemistry and Molecular Biology
Gothenburg, 2022

Thesis for the degree of Doctor of Philosophy
in the Natural Sciences

Microtubule structure and function as perturbed by electromagnetic fields

Greger Hammarin

Front cover: Density projection recovered from CDI data
Back cover: Simulated diffraction of helical fibre

ISBN 978-91-8069-071-3 (Print)
ISBN 978-91-8069-072-0 (PDF)
Available online at http://hdl.handle.net/2077/73893

Department of Chemistry and Molecular Biology
Division of Biochemistry and Structural Biology
University of Gothenburg
SE-405 30, Göteborg, Sweden
Printed by Stema Specialtryck AB
Borås, Sweden, 2022

Abstract

The front line of structural biology research lies in imaging proteins in motion. In order to understand how protein function is related to it's structure, methods with an appropriate temporal and spatial resolution for the specific function being investigated are required. Earlier research on light-sensitive protein complexes have achieved extraordinary temporal resolution, but there are no general methods available for the initiation and coordination of protein functional movements. Earlier research have also indicated that electromagnetic fields can induce proteins functionally relevant motions.

Microtubules are essential components of the cytoskeleton in all eukaryote life. They are predominantly constructed by two proteins α and β tubulin. Together these proteins forms a heterodimer which can organize itself in a tube-shaped microtubule. This thesis includes three scientific investigations of microtubule structure and function.

The highest resolution structures of microtubules, and proteins generally, have been determined using methods that rely on the sample being frozen or dried out. The first study of this thesis covers an attempt to image microtubules under physiologically more relevant conditions, in solution at room temperature. The spatial resolution achieved was lower than those of more established methods, but shows the potential of single particle imaging in liquid solution at room temperature. This thesis also presents two investigations into the question if electromagnetic fields with frequencies corresponding to those of cellular phones of today affects microtubule structure and function. These studies found no influence on either property outside of those that are associated with thermal and spatial alignment effects.

Sammanfattning

Frontlinjen för strukturbiologisk forskning ligger idag i att avbilda proteiner i rörelse. För att förstå hur proteiner fungerar rent strukturellt krävs avbildningsmetoder med en tid- och rums-upplösning anpassad för den specifika biologiska funktionen. Tidigare forskning rörande ljuskänsliga proteinkomplexs reaktion på ljus har genomförts med hög tidsmässig upplösning, men det saknas en generell metod för att initiera och koordinera proteinrörelser. Tidigare forskning har också indikerat att protein i starka elektromagnetiska fält kan induceras att uppvisa relevanta strukturella rörelser.

Mikrotubuli är essentiella komponenter i cellskelettet i allt eukaryot liv. De är i huvudsak uppbyggda av de två proteiner α- och β-tubulin. Tillsammans bildar de en heterodimer som kan organisera sig i en tubformade mikrotubuli. Denna avhandling inkluderar tre undersökningar av mikroubulis struktur och funktion.

Den mest högupplösta avbildningen av mikrotubuli, och proteiner generellt, baseras idag på metoder som kräver att proteinkomplexet fryses ned eller torkas ut. Avhandlingens första studie utgör ett försök att avbilda mikrotubuli under fysiologiskt mer relevanta omständigheter, i en rumstempererad lösning. Den rumsliga upplösning med vilken mikrotubuli avbildades är lägre än vad som uppnåtts med beprövade metoder, men samtidigt visar studien på potentialen att avbilda enskilda partiklar i flytande lösning och vid rumstemperatur. I denna avhandling presenteras även två studier som avsåg att undersöka om alternerande elektromagnetiska fält, med frekvenser motsvarande dagens mobiltelefoni och Wifi, påverkar mikrotubulis struktur och funktion. Studierna fann ingen sådan påverkan utöver de som kan associeras med värmeutveckling eller rumslig orientering.

Acknowledgements

With full knowledge that this is the part of the thesis that will actually be read by my colleagues, I will try keep it short and to the point.

We are all transients here. During my tenure as a PhD candidate a great deal of people have passed through the lab. The only constant at the Lundberg laboratory is the lunchroom conversations. How wonderful that such a place exist where everyday musings so quickly turns in to esoteric science-discussions. Sometimes it is more the going to get that cup of coffee that matters, not the actual drinking of it.

First of all, I want to thank my supervisor **Richard** for giving me the chance to work on a project this wild. I could not have wished for a better guide as I've taken these first steps into the world of research. I did not know what I signed up for, but it has been the experience of a life time. Although having many PhD students under his wing, he always finds time for a chat. I have enjoyed our discussions over the years, often of worldly topics such as faculty politics and Trumpian shenanigans.

I need to say how much I appreciate my partner in crime **Per**. - It has been a delightfully strenuous journey as we have tried to get a grip on how to build experimental setups and figure out how to make sense of it all.

Rob, sharing an office for years a fondness for dark humor was nurtured, perhaps as a sort of self defense. **Daniel**, you are so much more than that *able bodied young man* I once summoned to help out on a beamtime. **Giorgia**, your enthusiasm and determination is inspiring.

Beamtimes are special times. Bonds are forged when one is at the same time at ones best and at ones worst. **Rajiv**, we have done so many beamtimes together I can hardly count them, thanks for making them so enjoyable. Thanks also to **Adams, Aleksandr, Analia, Arpitha, Cecilia, David, Elin, Emil, Giorgia, Guo, Leona, Lucija, Owens, Rebecka, Peter, Peter, Petra, Rob, Rob, Swagatha & Tinna** for making memories in concrete bunkers around the world.

Thank you **Doris, Jessica, Jonathan, Rasmus & Viktor** for the brief glory of the Lundberg running club.

Thanks to all the inhabitants of the Lundberg lab cohort, new and old, for making this place such an amazing place to spend the arguably hardest years of your

life: **Amke, Andrea, Andreas, Ann, Atsarina, Bozidar, Dimitra, Damasus, Doris, Emelie, Emil, Filippo, Gabrielle, Hannah, Florian, Jens, Katharina, Laras, Lidija, Linnea, Maja, Majo, Mathias, Taru, Oskar, Torbjörn, Vaj, Weixiao, Ylber & Yosh**.

To the PIs of the Biochemistry and Structural biology labs, **Björn, Gergely, Gisela, Johanna, Julia, Kristina & Sebastian**, try to ensure the working environment is as great in the new building as it has been at the Lundberg lab. The lab environment would not function properly without **Bruno, Lars, & Valida**. Thank you for making our time here as easy as it can be.

It is truly a great gift to have been given the opportunity to have ones curiosity as a guide for these last few years.

Publications

This thesis consists of the following research papers:

PAPER I: Brändén, G., **Hammarin, G.**, Harimoorthy, R., Johansson, A., Arnlund, D., Malmerberg, E., Barty, A., Tångefjord, S., Berntsen, P., DePonte, D. P., Seuring, C., White, T. A., Stellato, F., Bean, R., Beyerlein, K. R., Chavas, L. M. G., Fleckenstein, H., Gati, C., Ghoshdastider, U., Gumprecht, L., Oberthur, D, Popp, D., Seibert, M., Tilp, T., Messerschmidt, M., Williams, G., Loh, N., Chapman, H., Zwart, P., Liang, M., Boutet, S., Robinson, R., Neutze, R., **Coherent diffractive imaging of microtubules using an X-ray laser**, *Nature Communications, 10, 2589 (2019)*

PAPER II: **Hammarin, G.**, Börjesson, P., Harimoorthy, R., Chen G., Bertnsen P., Widlund P. O., Stoij C., Rodilla H., Swenson J., Brändén G., Neutze R., **No observable non-thermal effect of microwave radiation on the growth of microtubules**, *Manuscript*

PAPER III: **Hammarin, G.**, Börjesson, B., Harimoorthy, R., Nasedkin, A., Stoij, C., Sarabi, D., Ortolani, G., Diaz, A., Lutz-Bueno, V., Appio, R., Swenson, J., Menzel, A., Brändén, G., Neutze, R., **Microwave induced orientation perturbations of microtubules**, *Manuscript*

Related papers that I have co-authored but that are not included in this thesis:

PAPER VI: Sharma, A., Berntsen, P., Harimoorthy, R., Appio, R., Sjöhamn, J., Järvå, M., Björling, A., **Hammarin, G.** , Westenhoff, S., Brändén, G., Neutze, R. **A simple adaptation to a protein crystallography station to facilitate difference X-ray scattering studies.** *Journal of Applied Crystallography, 52(2) (2019)*

PAPER VII: Seuring, C., Ayyer, K., Filippaki, E., Barthelmess, M., Longchamp, J.-N., Ringler, P., Pardini, T., Wojtas, D. H., Coleman, M. A., Dörner, K., Fuglerud, S., **Hammarin, G.** , Habenstein, B., Langkilde, A. E., Loquet, A., Meents, A., Riek, R., Stahlberg, H., Boutet, S., ... Chapman, H. N., **Femtosecond X-ray coherent diffraction of aligned amyloid fibrils on low background graphene.** *Nature Communications 9, 1836 (2018)*

PAPER VIII: Dods, R., Båth, P., Morozov, D., Gagnér, V. A., Arnlund, D., Luk, H. L., Kübel, J., Maj, M., Vallejos, A., Wickstrand, C., Bosman, R., Beyerlein, K. R., Nelson, G., Liang, M., Milathianaki, D., Robinson, J., Harimoorthy, R., Berntsen, P., Malmerberg, E., Johansson, L., Andersson, R., Carbajo, S., Claesson, E., Conrad, C. E., Dahl, P., **Hammarin, G.**, ... Neutze, R. **Ultrafast structural changes within a photosynthetic reaction centre.** *Nature, 589(7841), 310–314 (2021)*

PAPER IX: Dods, R., Båth, P., Arnlund, D., Beyerlein, K. R., Nelson, G., Liang, M., Harimoorthy, R., Berntsen, P., Malmerberg, E., Johansson, L., Andersson, R., Bosman, R., Carbajo, S., Claesson, E., Conrad, C. E., Dahl, P., **Hammarin, G.** , Hunter, M. S., Li, C., ... Neutze, R. **From Macrocrystals to Microcrystals: A Strategy for Membrane Protein Serial Crystallography.** *Structure, 25(9), 1461-1468.e2 (2017)*

PAPER X: Bath, P., Banacore, A., Börjesson, P., Bosman, R., Wickstrand, C., Safari, C., Dods, R., Ghosh, S., Dahl, P., Ortolani, G., Björg Ulfarsdottir, T., **Hammarin, G** ., Bonete, M. G., Vallejos, A., Ostojic, L., Edlund, P., Linse, J. B., Andersson, R., Nango, E., ... Neutze, R. **Lipidic cubic phase serial femtosecond crystallography structure of a photosynthetic reaction centre.** *Acta Crystallographica Section D: Structural Biology, 78(6), 698–708 (2022)*

Contribution report

PAPER I: I designed and implemented the phase retrieval algorithm, drew the majority of the figures and helped write the methods and results parts of the paper.

PAPER II: I purified the protein and devised the experimental setups in collaboration with my co-authors. I did the data collection, analysed the data, drew the majority of the figures and took part in the writing process..

PAPER III: I purified the protein and conducted the experiments in collaboration with my co-authors. I analysed the data, drew a majority of the figures and took part in the writing process.

"*Science depends on faith. Faith that the rules haven't changed, faith that the other guys got the measurements right. All science ever did was measure a teensy sliver of the universe and assume that everything else behaved the same way. If two experiments yield different results... Happens all the time, my friend. And when it does, every good scientist discounts those results because they failed to replicate. One of the experiments must have been flawed. Or they both were. Or there's some unknown variable that'll make everything balance out just as soon as we discover what it is.*"

Peter Watts, *Echopraxia*

"*Hammarinian solution: a highly impractical but not impossible solution to a given problem. Hammarinian solutions should strive to be on the very border between extremely impractical and impossible. When proposing a Hammarinian solution it is important to maintain a calm demeanour and act as if it would be entirely reasonable.*"

Robert Bosman, PhD

Acronyms

Here follows a list and explanation of the different acronyms used as abbreviations in this thesis.

ATP	**A**denosine **T**ri **P**hosphate
COM	**C**enter **O**f **M**ass
CSPAD	**C**ornell **S**LAC **P**ixel **A**rray **D**etector
DNA	**D**eoxyribo **N**ucleic **A**cid
ESRF	**E**uropean **S**ynchrotron **R**aditation **F**acility
FWHM	**F**ull **W**idth **H**alf **M**aximum
FFT	**F**ast **F**ourier **T**ransform
GDP	**G**uanosine **D**i **P**hosphate
GTP	**G**uanosine **T**ri **P**hosphate
GDVN	**G**as **D**ynamic **V**irtual **N**ozzle
IR	**I**nfra **R**ed
LCLS	**L**inac **C**oherent **L**ight **S**ource
MAP	**M**icotubule **A**ssociated **P**rotein
MAX IV	**M**icrotron **A**ccelerator for **X**-rays **IV**
MD	**M**olecular **D**ynamics
ML	**M**achine **L**earning
MTOC	**M**icro**T**ubule **O**rganizing **C**enter
OD	**O**ptical **D**ensity
PDB	**P**rotein **D**ata **B**ank
PTM	**P**ost **T**ranslational **M**odification
SAR	**S**pecific **A**bsorption **R**ate
SAXS	**S**mall **A**ngle **S**cattering
SLS	**S**wiss **L**ight **S**ource
SVD	**S**ingular **V**alue **D**ecomposition
TR-XSS	**T**ime **R**esolved - **X**-ray **S**olution **S**cattering
TTF	**T**umor **T**reating **F**ields
UV	**U**ltra **V**iolet
VNA	**V**ector **N**etwork **A**nalyser
WAXS	**W**ide **A**ngle **S**cattering
XFEL	**X**-ray **F**ree **E**lectron **L**aser

Contents

List of Figures

List of Tables

Till Signe och Vera

Chapter 1

Introduction

1.1 Natural science

Natural science has many branches (physics, chemistry, biology etc.), but is in essence a tool for discovery, a method for trying to understand how the world works. There is no general approach, but rather a range of specific tools used to pry information about the inner workings of the world. New tools are developed continually, and with these new kinds of information becomes available. The current model of *how it works* is only as good as the information you've used to construct the model. The work is never done, it's a continuing process. Science is in this sense an ongoing effort of model building based on information gleaned by using imperfect tools.

We are intrigued by the world by experiencing it in its natural and wild state, but often the process of trying to understand the world involves designing experiments with imposed constraints on the complexity.

There are many representations of an object that can offer insight into it's role. The process of trying to understand something is of course multifaceted. One way is to try to create a model which has some of the same features as the thing one is trying to understand. Maybe the model looks right from a certain angle, maybe it has the same function in some respect. The model is in all ways a reduced version of that which it is supposed to represent. A common approach in natural science is to come at the problem with separate lines of inquiry and make a working model that fits all the different modes of information. This thesis has been done at the intersection of biology, chemistry and biophysics, with an emphasis on methods within the field of Structural biology in which the aim is to understand the function via an understanding of the structure.

1.1.1 Structural biology

Structural biology is an area of natural science that sits just at the intersection between biology, chemistry and physics. Structural biology seeks to understand how the function of biological molecules is attained by it's structure at the atomic level. The dichotomy between structure and function is in a sense a technical one, since they are measured by different methods. Method developments have enabled simultaneous measurements of structure and function in the form of conformational dynamics. Molecular function is in essence the result of a combination of molecular rearrangements and chemical alterations. And since this function is dynamic the field of structural biology must aim to capture the molecular movements involved in the action.

1.1.2 Models and methods

Depending on the research question at hand different models and methods for investigation are suitable.

In order to understand how something works we must watch it in action. And watching here means finding some aspect of the object to measure with a tool at hand. The measuring of something in action often necessitates designing a means to poke it with a stick to make it tick.

In Structural biology there are many available techniques for both prodding and probing proteins. The ones used in this thesis will be introduced in chapter 2. Both the probes we use and the method of perturbing a system have their inherent limitations. It is not possible to know if the perturbation acted upon the system will incite a natural response or something unique to the disturbance acted upon it. For this end, control mechanisms need to be put in place. The scientific publication process have some of these built in, with the review process by peers in the scientific community which could ideally point out flaws in reason or methodology. But most important is to continually question ideas and interpretations in search for potential biases and blinders. This means having to be your own worst critic, having a healthy distrust of the results and to use this drive to design better experiments. Namely, to fail better next time [1]. At the same time, in order for science to progress, one must sometimes be bold and dare to interpret incomplete data. Knowing the limitations of a method does not mean it is not useful. For example, while being the most successful methods for determining protein structure, X-ray crystallography and electron crystallography/microscopy, both rely on methods for sample preparation that takes the protein very far from its natural state [2, 3]. Proteins prepared for electron microscopy and crystallography are generally frozen in order to lie still on

the examination table. Flash freezing might stop proteins in mid stride if the dynamical process investigated is slow enough [4]. X-ray solution scattering keeps proteins in a more natural state, but it is an inherently low resolution technique. Whilst proteins trapped in crystals retain a degree of freedom and can actually still perform their function to some extent, it is uncertain how natural the range of allowed motions is. Another example of method limitations is the difficulty to find methods for the initiation of protein function when trying to image structural movements. For naturally light-sensitive proteins this has been done with great success, but there is no generally applicable method available [5, 6].

Investigations of dynamical processes sets certain demands of the probes and perturbations used with regards to both time and spatial resolution. Protein conformational movements happen on time scales spanning several orders of magnitude [7]. Understanding of how local conformational shifts on the pico- and nano-second time-scale are linked to the much slower global conformational shifts is an important question for structural biology [8]. The development of methods to probe the structure of proteins on the same timescale as the fastest reactions has made this possible. In order to really understand dynamical processes it is important to measure individual proteins in action. Any method measuring assemblies will inexorably lose information about potential distributions in behaviour as a consequence of averaging.

Different kinds of probes and perturbations are available for studying proteins *in vivo* and *in vitro*. Although some developments of methods for structural determination *in vivo* have been made [9, 10], structural biologists tends to focus on in vitro measurements. There are both benefits and drawbacks to this. Different levels of understanding can be achieved depending on how simplified the experimental situation is compared to it's *in vivo* counterpart. An example of this is the previously mentioned sample preparation methods for structural determination. The methods that can achieve the highest resolution are also those which probes samples the farthest from it's natural state. Sometimes this reduction of complexity is necessary to perform the measurements at all. I believe it is important to complement high detail structures made with crystallized and/or frozen samples with measurements in conditions that more closely resembles the natural environment of the proteins.

1.2 Proteins

1.2.1 Life as we know it

There is no record of the beginning of life on earth and it's emergence from the primordial soup [11]. Current models suggest an *RNA world* as the origin of life

on Earth [12]. RNA can both store information, replicate and perform chemical work. Somewhere on the road to more complex life DNA took over the role as genetic storage, probably due to it's superior chemical resistance [13]. And the folded amino acid chains we call proteins took over the jobs as chemical catalysts and general workers. Life as we know it on earth is built upon the multiplication of cells, compartmentalized structures with the ability to generate copies of itself. Cell walls are predominantly made by phospholipids that act as a divider of inside and outside, allowing for the formation inner structures.There are ideas of how temperature gradients could drive cell divsion [14], but today this process is expedited by the cytoskeleton, see chapter 3 for an introduction.

There is considerable debate on where viruses fit in the Tree of Life [15, 16] among or beside the three domains [17]. Phylogenetic analysis is difficult due to the varying rates of evolution [18], but there have been attempts of instead using structural similarities to differentiate between lineages [19].

DNA is the code of life, a sequential list of recipes of how to make proteins. The human genome contains genes for approximately twenty thousand proteins [20,21], but the proteome is considerably larger, considering splicing, post-translational modifications and other ways of letting a single gene give rise to a multitude of proteins [22].

1.2.2 Molecular machines

Proteins are molecular machines that perform work, chemical and physical, inside and outside the cell [23]. Molecular machines transport species across cell boundaries and along cellular transport pathways. Molecular machines enable thermodynamically unfavourable or improbable chemical reactions. Proteins, the workhorses of biology, is what makes us tick. Living is having a collection of proteins that perform their assigned tasks in conjunction with others. Most medicines are interacting with proteins, affecting their behaviour in some way [24]. Understanding the protein machinery is key to be able to effectively perform structure-based drug design [25].

1.3 Societal concerns

This thesis revolves around the usage of electric fields as a general approach to stimulate protein motion, for the use in time-resolved structural studies. At the same time, modern technology envelops us with electromagnetic fields of varying kinds. Cellular phones and WiFi-routers are prevalent examples of electronic devices that emit radiation in the microwave range. It is therefore of societal

importance to study the biological effects due to this non-ionizing radiation. Indeed, the fear of possible adverse effects have drawn much public attention in the recent years, especially in connection with the ongoing roll-out of 5G-cellular networks [26]. Although many studies about possible effects of electromagnetic radiation have been published, often with a focus on toxicological endpoints such as cancer or alterations in genetic transcription of heat-shock proteins, there is no scientific consensus at this moment [27]. The exposure protocols vary, quality of controls vary and reproducibility is low. For microtubules specifically, there have been decades of speculation with regards to specific electromagnetic properties and modes of interaction.

1.4 Aims of this thesis

The aim of the research presented in this thesis has been to try to develop new insight into the structure and function of microtubules by means of exploring methods for single particle and coherent diffractive imaging.

Another aim has been to investigate potential interactions between microtubules and electromagnetic fields, and in connection to this address societal concerns regarding microwave exposure. Working with microtubules, protein structures long suspected to be susceptible to electromagnetic fields, it can be argued that we have an ethical obligation to use methods where we are proficient to try to help answer questions relating to public health [28].

The aim of this thesis is to provide a background to the research questions asked as well as give a brief presentation of the main results of the scientific papers on which this thesis is built.

1.5 Organization of this thesis

Chapter 2 introduces the foundations of the methods used in my investigations. It all revolves around different uses of light and light's different interactions with matter and itself. This chapter also covers electromagnetic fields with wavelengths longer than what is commonly thought of as light, such as those we surround ourselves with, with our cellular phones and WiFi routers, including concerns that such fields might perturb biological systems. Chapter 3 explains the role of tubulin in the cytoskeleton, its properties and behaviour. This chapter also covers the speculations of both tubulins remarkable electrical properties and suggested interactions with electromagnetic fields.

Chapters 4, 5 and 6 presents the results of the original research papers on which this thesis is based. A summary and outlook is provided at the end in chapter 7. Whenever one question is answered, another one inevitably arise. For this reason, this chapter also introduces ongoing experimental investigations that digs deeper where **PAPER I-III** left off. These experiments constitutes the road map ahead for the aim of this thesis.

Chapter 2

Probes and perturbations

Different techniques for imaging an object bring different ways to understand the structure. The tool used to image the object is at the same time enabling and limiting the understanding. The structure of a thing is important, but to connect a function to the structure one needs to image it while it performs its function. One approach to understand how a system works is by perturbing it in some way and looking at how it changes. At times the perturbation is targeted and at times more broadly aimed. A common terminology for this approach is *pump-probe*, although its name derives a specific experimental methodology where light is used to *pump* electrons to a higher state which is then probed by another light source [29]. This chapter will introduce the different methods for probing and perturbing a system used in this thesis.

On a few occasions, this chapter exemplifies a method using microtubules. Microtubules are large macromolecular complexes consisting of tubulin proteins bound together and arranged in a tubular structure. Microtubules perform a diverse range of functions in the cell. The structure and function of microtubules are introduced in chapter 3.

2.1 Light

Depending on the circumstances light is best described as a particle, a photon, or as an electromagnetic wave. The understanding of this complementary duality came hand in hand with the development of quantum-mechanics [30]. Electromagnetic waves can be separated in terms of perpendicular electric and magnetic field vectors (fig. 2.1). An electric and a magnetic sinusoidal wave propagating in phase but at perpendicular angles at the speed of light.

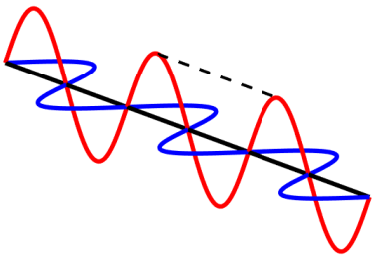

Figure 2.1: Illustration of an electromagentic wave, with electric and magnetic field vectors perpendicular, but in phase. Wavelength marked with dotted lines.

The relationship between wavelength λ [m] and frequency f [s^{-1}] of an electromagnetic field is the same as for any other wave (ocean waves, sound etc.), just that the wave velocity is always the speed of light c [ms^{-1}].

$$\lambda = \frac{c}{f} \tag{2.1}$$

The corresponding photon energy E [eV] is directly proportional to the frequency modulated by Planck's constant h [eV s].

$$E = h \cdot f \tag{2.2}$$

Light can interact with matter i several ways. Light can be absorbed and sometimes re-emitted as well as scattered, all depending on the wavelength of the light and the matter at hand.

Light can also interact with light itself, with the superposition of waves. Interference of waves with the same frequency and phase results in a wave with double the amplitude, whilst two waves of same frequency and opposite phase will cancel each other out. Figure 2.2 illustrates this phenomenon.

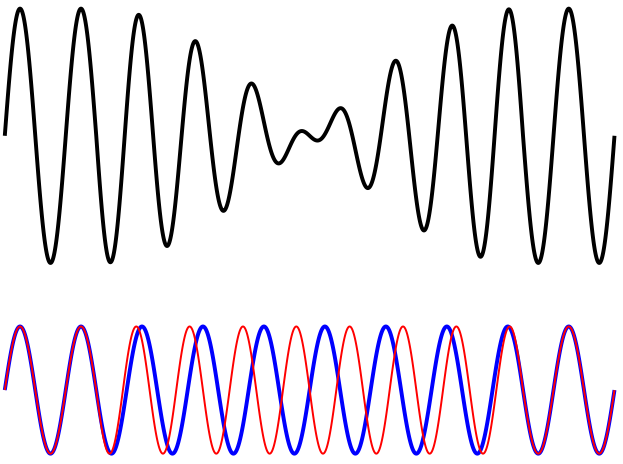

Figure 2.2: Model of interference, sinusoidal curves in red and blue starting out in phase with constructive interference, and with destructive interference when the phases are opposite. Interference shown in black

Light can act both as a probe and a means to perturb a system. The different light interactions used in this thesis work include scattering and absorption as well as emittance, specifically black body radiation.

An overview of the electromagnetic spectrum is shown in figure 2.3. The dichotomy of electromagnetic radiation into different classes (radio, microwave, light, infrared (IR) , ultraviolet (UV), X-ray, gamma) makes it relatable but the fundamental properties and interactions are the same. However, there exists a functional divide between non-ionizing and ionizing radiation. Electromagnetic light with a shorter wavelength than $\approx$ 100 nm have a large enough energy to detach electrons from an atom and thereby creating an ion. This limit is comparable to the delimiter wavelength between UV and X-rays. The energy necessary for ionizing is different for different atomic species and depends on how bound the outer layer electrons are.

2.1.1 Visible light

There is an inherent biological preference to using visible light when first approaching the problem of describing something. Although many species perceive light in a broader spectrum than humans, visible light is classified as light with a wavelength within a narrow band ranging from red (λ: 700 nm, f: 430 THz) to violet (λ: 400 nm, f: 750 THz). Since visible light is considerably larger than the structures studied in this thesis it has not been used as a probe. I have however

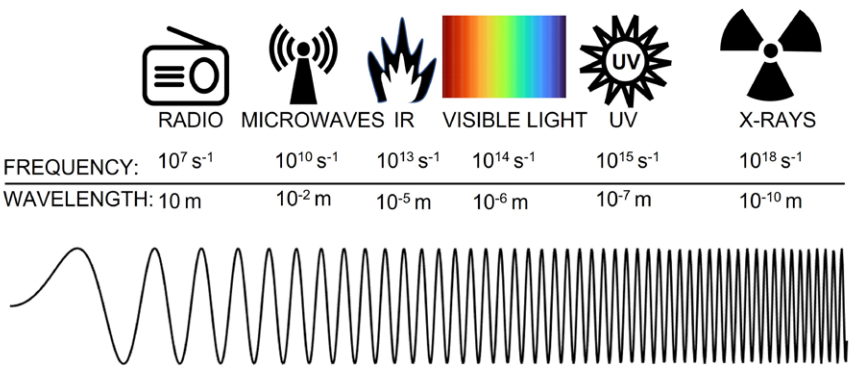

Figure 2.3: Overview of electromagnetic spectrum. Representative wavelengths and frequencies given. Not to scale.

been part of experiments where visible light has been used to trigger reactions in photosensitive proteins [31]. Although not included in my thesis, this paper showed how a crystallography beamline could be easily adapted for difference X-ray scattering studies. In that work we used red light in the visible range to stimulate the conformational photoswitching of phytochromes.

2.1.2 Infrared light

The wavelength distribution and intensity of thermal electromagnetic radiation emitted from an object, known as black-body radiation, is related to its temperature and is described by Planck's radiation law. While heated iron or a burning candle emits radiation into the visible range, objects with a temperature of approximate room temperature emit light only in the infrared range. In our experiments we have utilized this effect in order to measure the temperature of a sample by using an infrared camera (fig. 2.4).

The camera was equipped with microbolometer, a matrix of thermistors, to detect the irradiation in the Long Wave IR range, with detection of wavelengths between 7 and 18 μm. It is straightforward to convert the detected irradiance to temperature by mapping the peak positions and values when compared to an internal control. Figure 2.5 illustrates this with a set of theoretical curves calculated using Planck's law.

The detection range of the camera was ideal since we did not want the measurements to be influenced by the direct beam of an IR laser we sometimes used

Figure 2.4: Example of an image from a thermal camera. The object being imaged is a custom designed flow-cell for the application of electric fields over a sample housed in a capillary. The sample is heated by the applied microwaves.

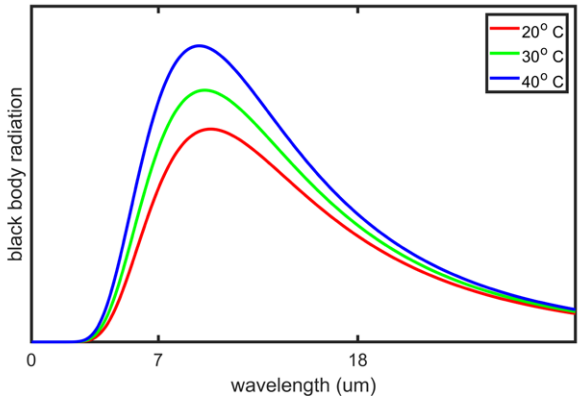

Figure 2.5: Black body radiation as calculated for select temperatures using Planck's law for the relevant detection range of our IR camera.

to heat our samples. This specific IR laser had a wavelength of 1.47 μm which would not be directly detected by our IR camera.

I have also been part of experiments where near infrared light has been used to trigger specific reactions in photosensitive proteins [32]. Although not included in my thesis this paper showcase the initiation and coordination of protein motions with a temporal resolution of pico-seconds. IR can also be used in pump-probe experiments to rapidly heat a protein environment, possibly allowing it to sample a broader conformational space [33].

2.1.3 Ultraviolet light

Protein concentration measurements using near UV

Spectrometry can be used to determine the protein concentration in a solution due to the amino acids Tyrosine and Tryptophan having a specific absorption of light with a wavelength of $\approx$ 280 nm. Although all amino acids with aromatic rings absorb in the near ultraviolet range and there are contributions from disulphide bonds as well as interactions between charged side-chains [34], Tyrosine and Tryptophan completely dominate the absorption spectra at this wavelength. The protein concentration in a sample can thus be determined by the absorption when the specific amino acid sequence is known. Nucleic acids have a strong absorption at slightly shorter wavelengths which means that the molar extinction coefficient for a protein that binds nucleic acids such as GTP needs to incorporate this into the calculations. For tubulin heterodimers with bound GTP/GDP the extinction coefficient is calculated to be 115,000 M^{-1} cm^{-1} [35].

Measuring microtubules kinetics using Optical Density

Microtubules polymerizing in a solution will change both the viscosity and the opacity of the solution. The change in optical density of a solution containing microtubules directly corresponds to the mass of microtubules longer than the wavelength of the probing light. The relationship between microtubule mass concentration and optical density is shown to be linear for all practical purposes [36, 37]. It is though, important to understand the specifics of the relationship because there are circumstances where the linear relationship breaks down. The equations assume that the solution is both monodisperse and the microtubules randomly oriented. The random orientation requirement requires that the solution is stationary, since microtubules, and other high aspect ratio objects readily flow align in small tubes such as capillaries. Also, when the concentration of microtubules is high enough to make multiple scattering events probable the linear relationship breaks down [38]. It has been reported that this

limit is as low as 1.5 mg/ml [39] for a setup with a path length of 0.5 cm, a considerably longer path length than that of the capillaries we have used. The absolute values of the optical density change depends on the specific setup and the relation to actual concentration needs to be empirically established. The wavelength used to probe the sample, in our case 365 nm, determined the cut-off for length sensitivity of the fibres. A shorter wavelength would improve the sensitivity for shorter microtubules, but this is not suitable due to the protein and nucleotide absorption for shorter wavelengths.

2.1.4 Long wavelength electromagnetic fields fields

The long range of electromagnetic fields from Teraherz to radio are non-ionizing. However, there is a justified interest in the possible perturbations by these fields on biological systems. We are surrounded by man-made electrical fields and there is a societal interest in the possible adverse effects of man made electrical sources of fields.

There is also the hope of finding a generalized approach to initiate protein conformational movements. While electromagnetic fields in the UV, IR, visible range has been used to instigate specific reactions in proteins there is an idea that electromagnetic fields can provide the energy for a protein to sample a broader range of the conformational space. If the binding of a protein with a known ligand, or activating a chromophore with a suitable color of light is a precision screwdriver, the idea of using an electric field would be akin to banging it with a hammer. There are examples where a strong pulse of an electric field could induce relevant structural changes in proteins [40]. The development of this method, coined electric field–stimulated X-ray crystallography (EF-X), as a general purpose method for protein dynamic studies has not caught on.

Microtubules, being exceptionally polar protein superstructures, have been of interest for the possibilities of interactions with a range of electromagetic fields. These speculations will be covered in more depth in section 3.3.

Microwaves

The societal interest in potential adverse effects of electromagnetic radiation has recently been centered on microwaves emitted by cellular phones, especially with the roll out of the fifth generation technology standard for cellular networks (5G). 5G being rolled out as this thesis is written. The term *cellular* comes from the organization of telecommunication into geographical areas with local antennas, basestations, cells. The 5G standard was preceded by LTE (4G), UMTS (3G) and GSM (2G). All the underlaying technologies of these standards work within

what is called the ultra high frequency radio band, which is a term applying to frequencies between 300 MHz and 3 GHz. 5G includes these frequencies but also venture towards the super high frequency band which covers frequencies between 3 GHz and 30 GHz. Both these radio frequency bands are encompassed by the broader term microwaves. The higher frequencies of 5G enables an increased bandwidth but comes with a cost. The attenuation in air increases with frequency and the cells have to be smaller than for the previous generation networks, assuming the signal strengths to stay the same.

The most common association with the term microwaves is the microwave oven. Microwaves ovens utilize electromagnetic radiation of specific wavelengths to make water molecules dance. The absorption spectra of water is broad and the frequency chosen for household microwave ovens is not the optimal one for heating water since it would otherwise boil the outer parts of the foodstuffs [41]. The absorption of electromagnetic radiation by water has been investigated for a long time and the theory is not yet finished. The optimal absorption frequency varies with both water temperature and salt content [42, 43].

The current guidelines regarding microwave exposure published by the International Commission on Non-Ionizing Radiation Protection (ICNIRP) is based on microwaves heating tissues containing water [44]. For frequencies below 6 GHz the exposure limit for the general public is a Specific Absorption Rate (SAR) of 2 W/kg. For frequencies above 6 GHz a weight based limit is not suitable since most of the radiation would be absorbed in the skin. For these higher frequencies the limit is instead set at 20 W/m^2.

Studies have found that microwave radiation disrupts the membranes of both bacteria and eukaryotes using microwaves with an high exposure level exceeding the ICNIRP guidelines [45,46]. Even for studies using considerably lower exposure levels, the induced heating of the sample makes it difficult to design a proper control experiment [47]. A couple of studies on human epithelical cells exposed to 40 GHz and 60 GHz electromagnetic fields found no changes in heatshock reporter gene expression or genotoxicity and attributed this result a low power exposure scheme which had no thermal effect [48,49], especially when comparing the experimental design to other studies which used a higher power and had found an effect. A couple of review papers call the studies that find biological effects into question since they are neither replicated nor standardized [27, 50].

Teraherz radiation

There has been decades of speculations regarding the possibility of long range coherences, Frölich condensations, in proteins [51, 52]. However, the experimental observations of this is scarce and inconclusive [53, 54]. Studies of how Teraherz

radiation affects biological systems have been claimed to suffer from similar problems of experimental design as some of the microwave research [55].

2.2 X-rays

What in English is called X-rays was discovered by Wilhelm Röntgen in 1895 [56]. In Swedish the name is *Röntgenstrålning*. The newly discovered rays were identified as being electromagnetic radiation by their diffraction by a crystal [57]. Today, electromagnetic radiation with a broad range of wavelengths between tens of picometers and a few nanometers are labeled X-rays, whilst the most common wavelengths for scientific applications hover around 1 Ångström.

While diffraction using light had been known for hundreds of years the study of the arrangement of atoms required electromagnetic radiation with a wavelength similar to the size of and the spacing between them. The size of an atom depends on the number of electrons around the nucleus. Inter atomic distances in a material is determined on the bonds lengths which are different for different element combinations and depends on the number of electrons involved. Both the atomic sizes and bonded distances are approximately 1 Ångström and thus corresponds nicely to the wavelength range of X-rays.

X-ray crystallography has been around for over a hundred years. Max von Laue was awarded the Nobel prize in physics in 1914 for the discovery that X-rays could be used to determine the structure of a crystal. William Henry Bragg and William Lawrence Bragg was awarded the Nobel prize the following year for further elucidating the physics of X-ray crystal diffraction and solving the first structures.

2.2.1 X-ray scattering and diffraction

Diffraction is the result of an interaction between an electromagnetic wave and matter. Incident X-ray photons can be scattered by an atom when, primarily, it's electric field interacts with it's electron cloud. Light can be scattered both in-elastically, when the scattered light's wavelength is changed by the interaction and elastically, when the scattered light has the same wavelengths as the incident light. This thesis will deal only with elastic scattering, also called *Thomson* scattering. Very few of the incident X-rays actually interact with the object and the majority of the ones that do are either absorbed (photoelectrically) or scattered in-elastically. Far less than 1% of the incident photons will scatter in a for us useful way, elastically and coherently [58]. The wavelength of the X-rays determine the limit of attainable resolution.

When the incident photon interacts elastically with the electrons of an atom the electric field causes the electrons to accelerate and emit electromagnetic waves spherically with the same wavelength as the incident light. Atoms with a higher atomic number and more electrons scatter more than less electron dense atoms. The amplitude of the scattering from an atom is called the atomic form factor f and is related to the electron density ρ around the atom.

When an electromagnetic wave is elastically scattered by several electrons the resulting waves will interact, with fully constructive and destructive interference as the edge cases. The interference at the measurement point is determined by the difference in distance travelled by the two waves. This distance is angle dependent. Figure 2.6 illustrates this phenomenon. For elastic scattering the incident and scattered waves remain in coherence, which enables an interpretation of the interference pattern. If the difference in distance is an integer multiple of the wavelength the scattered waves will remain in phase and the interference will be constructive. If the scattered waves are out of phase the interference will be destructive. It is important that the incident wave is both coherent and monochromatic [59].

For an actual experiment the sample is small compared to the distance to the detector which satisfies the Fraunhofer condition which means that scattered waves from different parts of the samples can be assumed to be parallel [59].

Bragg's law, suitable for crystallographic studies where the sample is ordered in a lattice, states that constructive interference resulting in bright so called Bragg peaks, occur at the angle θ when then difference in path length of the scattered waves from different scattering planes is an integer multiple n of the wavelength λ, where d is the distance between the crystal planes [60].

$$n\lambda = 2dsin(\theta) \tag{2.3}$$

The incident wave, assumed to be a plane wave, has a wave vector k_i defined as $k = 2\pi/\lambda$. The elastically scattered wave has a wave vector of k_s and since the scattering is elastic these wave vectors have the same magnitude, $|k_i| = |k_s|$. The angular change in direction of the scattered wave is explained by the momentum transfer q and defined as $q = k_s - k_i$ (fig. 2.7).

The magnitude of q is defined in equation 2.4, where 2θ is the angular difference between the incident and scattered wave vector.

$$q = \frac{4\pi sin(\theta)}{\lambda} \tag{2.4}$$

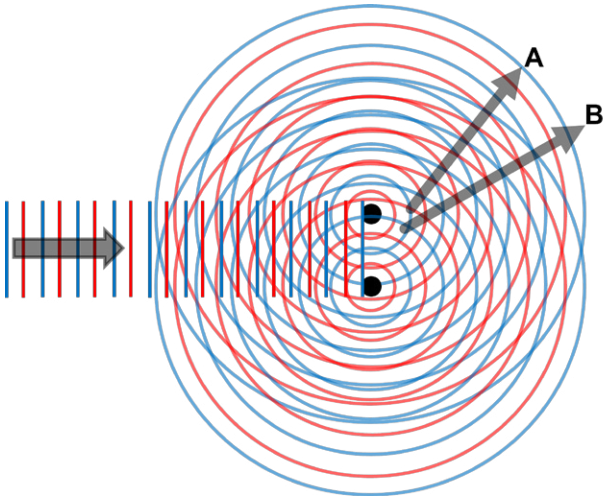

Figure 2.6: Elastic scattering by pair of electrons with red and blue signifying peaks and valleys of the incident and scattered waves. **A**) Destructive interference at an angle where the scattered waves are out of phase. **B**) Constructive interference at an angle where the scattered waves are in phase. This figure is not at scale and is not satisfying the Fraunhofer condition.

For a set of *N* scattering objects, such as in a molecule, the scattered wave's phase difference at the detector depends on all the distances r_N between them. The summed scattered wave is called the form factor $F(q)$ and includes the atomic form factor *f(q)*.

$$F(\mathbf{q}) = \sum_{N=1}^{N} f_n(\mathbf{q}) e^{i\mathbf{q}\cdot\mathbf{r}_N} \tag{2.5}$$

This can be rewritten using the relationship between form factors and a continuous electron density ρ as a Fourier transform of the systems electron density.

$$F(\mathbf{q}) = \int \rho(\mathbf{r}) e^{i\mathbf{q}\cdot\mathbf{r}} d^3r \tag{2.6}$$

The intensity *I(q)* measured at the detector is the product of the amplitude of the wave with it's complex conjugate, $I(\mathbf{q}) = F(\mathbf{q})F(\mathbf{q})^* = |F(\mathbf{q})|^2$. The phase is thus lost and the electron density cannot be directly recovered. What can be recovered is instead the autocorrelation of electron density.

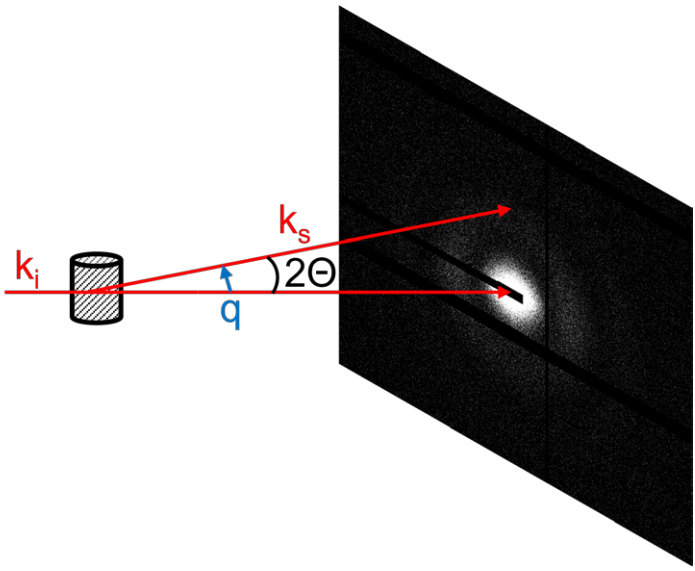

Figure 2.7: Illustration of scattering event. Incident and scattered wave vectors denoted with subscript i and s respectively. Example of isotropic solution scattering diffraction pattern on detector. Direct beam caught by beamstop.

For solution scattered certain assumptions can be made; that the sample is isotropic and it's constituents have random orientations. This further reduces the information content of the measured signal. The complex phase factor $e^{i\mathbf{q}\,\mathbf{r}}$ becomes $sin(qr)/qr$ when spherically averaged. This orientational averaging of the amplitudes is described by the Debye equation where r_{ij} is the distance between scatterers with respective form factors $f_i(q)$ and $f_j(q)$ [61].

$$\langle I(q)\rangle = \sum_{i=1}^{N}\sum_{j=1}^{N} f_i(q) f_j(q) \frac{sin(qr_{ij})}{qr_{ij}} \tag{2.7}$$

The sample being isotropic means that the measured signal is also isotropic, Figure 2.7 contains an example of an isotropic diffraction pattern. This makes it impossible to know how the different distances are related to each other.

By combining equation 2.3 and 2.4 an equation relating the real-space distance d to q can be written.

$$d = \frac{2\pi}{q} \tag{2.8}$$

Another way to relate real-space distances to what is actually measured in a solution scattering experiment is to relate them to their respective terms in the Debye equation 2.7. The intensity I for a select number of distances between unitary electron densities, with arbitrary units is shown in figure 2.8. By looking at the intensity contributions from different distances it is clear that smaller distances relate to a higher intensity at higher q, while larger distances have most of their intensity and information content at lower q. Translating this into scattering angles through equation 2.4 one can say that larger features predominantly scatter at low angles and smaller features scatter at higher angles. This is the basis for the functional distinction between Small Angle X-ray Scattering (SAXS) and Wide Angle X-ray Scattering (WAXS). The two different methods are geared towards investigations of features with different length scales. Relating this to protein scales, at low q, small scattering angles, the general size and shape (tertiary and quaternary structure in case of protein complexes) of the protein can be determined, while inter-atomic distances and amino acids sequence (primary structure) scatter at wider angles. In between these two extremes, motifs such as alpha helixes and beta sheets and how the polypeptide chains are folded together (secondary structure) are found.

Since a molecule is mostly empty space, the probability that an incoming X-ray hit an electron (using particle terminology) or interacts with an electron cloud

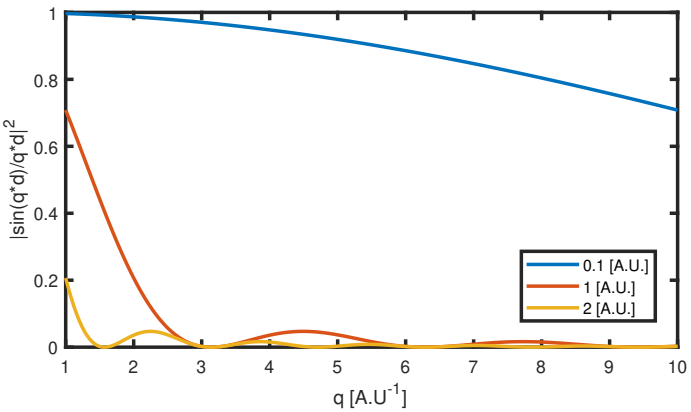

Figure 2.8: Theoretically calculated Intensities for a selection of arbitrary atomic separations on a reciprocal unit scale. Calculated from equation 2.7. Larger distances have their most information content at low q while smaller distances extend to higher q.

(wave terminology) is very low. This requires either the photon intensity to be very high or the sample to be very large. In practice, solution scattering using X-rays required more brilliant sources than the initial experiments with protein crystallography to be useful [62]. Synchrotrons rather than the tabletop sources of old. The absorbance cross section depends on electron cloud size, and for the atoms normally occurring in biological molecules these are rather small, which is why a brilliant X-ray source is needed. The development of Synchrotrons and XFELS enabled experiments with biological molecules in solution.

2.2.2 X-ray protein crystallography

Max Perutz [63] and John Kendrew [64] solved the first protein structures, for haemoglobin and myoglobin respectively and were awarded the Nobel prize in Chemistry in 1962. The phase problem was solved by isomorphous replacement, where electron rich heavy atom are introduced into the crystal unit cells. The very same year Francis Crick, James Watson and Maurice Wilkins was awarded the Nobel price in Medicine for solving the structure of DNA, a related biomolecule.

The three-dimensional structure one can obtain using X-rays is an electron density map. X-ray crystallography remains the main technique for solving protein structures and to date more than 150 000 structures have been deposited to the PDB. X-ray crystallography, as the name implies, requires well ordered crystals.

Unfortunately not all proteins crystallize easily or at all, requiring other means of determining their structure.

X-ray crystallography gives the average structure of multitudes of presumed identical proteins in a hopefully well ordered crystal lattice. Even proteins stuck in a crystal lattice have degrees of freedom in movement and some parts are more flexible than others. The most static parts of the protein are the ones that are best resolved by the resulting crystallographic structure [65]. In crystal diffraction only the well ordered parts scatter brightly. The "shadow" of the disorder in the crystals can still be seen as diffuse scattering overlaid on the bright Bragg peaks, and are described by the Debye-Waller factor [66].

Crystals are generally probed from a set of different angles by rotating it in front of the X-ray beam using a goniometer. In order to reduce X-ray induced damage to the molecules due to inelastic scattering, Compton scattering, and photoelectric absorption, they are often cooled [67].

An argument towards protein structures inside crystals are comparable to the *real* structure is that they retain their function inside crystals, which has been known for a long time [68]. The function and accompanying structural movements are to different degrees affected by the crystallization conditions and the lattice restraints [2, 69].

2.2.3 X-ray solution scattering

X-ray solution scattering, albeit a low resolution technique compared to crystallography, is especially useful when investigating dynamic processes, both for proteins and chemical reactions [70–72]. Even at low resolution SAXS can provide high accuracy size determination of larger objects features such as the microtubule diameter [73, 74].

Since it is impossible to directly calculate the pair distance distribution of a sample from the detected signal, solution scattering data is of best use when the structure is at least partly known.

For solution scattering the measured intensities is a combination of all the constituents of the sample, for example protein, buffer, hydration layer of differently structured water around the protein surface [75] and sample holder. In order to extract the signal from the protein of interest the other components need to be measured separately and subtracted from the combined signal. In this thesis however, only difference scattering is used, which makes the separation of the signal into it's constituent parts unnecessary. Difference scattering is the difference in scattering of the sample in two different states, $\Delta I(q) = I_{perturbed}(q) - I_{baseline}(q)$ [31].

Another important consideration is to try to limit the amount of stray scattering from upstream the beampath. This is usually done by a combination of slits and a collimator tube positioned just before the beam hits the sample (fig. 2.9b). The x-ray tube is pumped to a vacuum to avoid air-scattering along the way. If the experimental geometry prevents positioning the sample close to the collimator it is advisable to find another way of reducing air scattering (fig. 2.10). It is likewise important to reduce the amount of air between the sample and the detector since this would also scatter. The density of air is low, but the volume is far greater than the sample volume. For this end the sample or at least the space between the sample and the detector can be kept in vacuum, or within a housing filled with a low scattering species such as Helium (fig 2.9a).

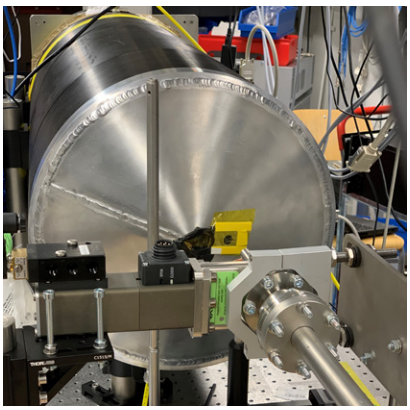

(a) Steel Helium cone at FemtoMAX beamline, MAX IV

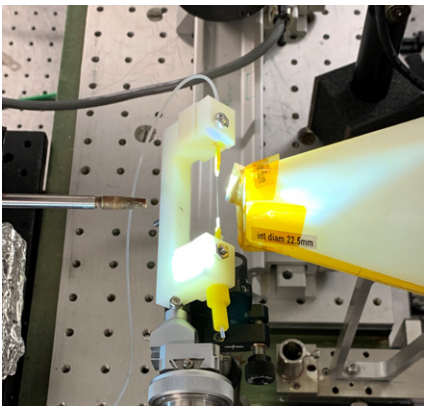

(b) Collimator and plastic helium cone at ID09 beamline, ESRF.

Figure 2.9: Beamline essentials

The beam cannot be allowed to hit the detector directly since it would damage it. This is accomplished by either having a hole in the middle of the detector with a beamstop positioned behind, or by placing a beamstop in front of the detector to block the path of the beam (fig. 2.7 & 6.7). A beamstop in front of the detector allows for positional freedom of the detector with respect to the X-ray beam. Sometimes the beamstop is equipped with a diode so that the beam intensity can be measured. This measurement can also facilitate aligning of sample in the beampath. An example of such diode readings are shown in figure 6.3a.

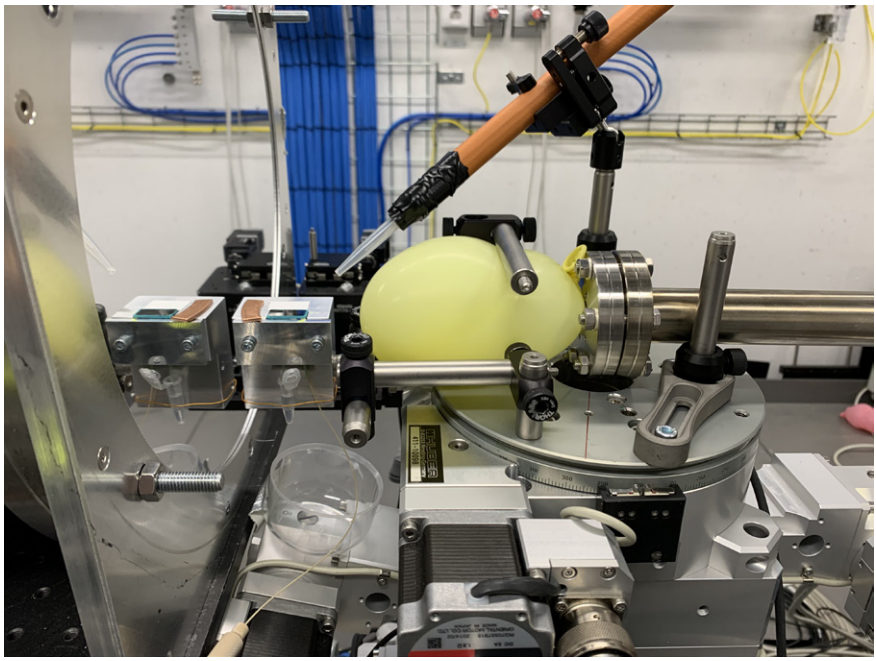

Figure 2.10: Helium filled balloon placed between sample and X-ray tube to minimize air scattering.

SAXS and WAXS

Small Angle X-ray Scattering and Wide Angle X-ray Scattering are not different techniques per se, but signifies different types of experimental setups. The cameras used for measuring the scattered photons are comparably small and trade-offs have to made when determining detector placement. A choice informed by which scattering angles and corresponding q range is of interest, and which angular resolutions is needed. For SAXS measurements the detector is placed far away from the sample. An example of this is the Ultra-SAXS beamline ID02 at ESRF which can place the detector as far off as 30 meters away from the sample [76]. In order to capture the wider scattering angles, corresponding to higher q and an increased spatial resolution, setups for WAXS measurements place the detector closer to the sample position. The detector placement for WAXS and protein crystallography is similar and I've been part of an proof-of-principle adaptation of a crystallographic beamline for solution scattering measurements [31]. Many experimental beamlines can vary the detector distance, to a certain degree, and datasets measured at different scattering angles can be merged and analysed jointly. The dichotomy between SAXS and WAXS is fluid and based on design considerations when building experimental stations.

Solution scattering measurements, images recorded on a detector, are often dimensionally reduced by azimuthal integration into a curve where intensity is plotted against q [77]. Several such curves are found in this thesis, for example figure 4.1a.

2.2.4 Synchrotrons and XFELS

Whilst the original X-ray sources utilized the photons sent out by breaking electrons in desktop sized apparatuses, *Bremsstrahlung*, Synchrotrons and Linear Accelerators are large scale structures that utilize the electromagnetic radiation emitted by electrons accelerated perpendicular to their path. Electrons are first accelerated to close to the speed of light, then kept in a storage ring by bending magnets (fig. 2.11b). The electron bunches are subjected to periodic arrays of magnets in arrangements called wigglers and undulators [78] in order to generate the X-rays. The arrangement of magnets gives an magnetic wave which due to the relativistic speeds of the electrons is *percieved* as having a wavelength corresponding to the desired wavelength of X-rays. The magnetic forces accelerate the electrons transversely to their travelling direction which causes them to emit electromagnetic radiation in the forward direction. In the end the electron beam is diverted and dumped (fig. 2.11a). An illustration of the storage ring and

the X-ray generation for use at experimental stations, beamlines, is provided in figure 2.12.

(a) Beamdump **(b)** Bending magnets

Figure 2.11: Synchrotron essentials, examples from MAX IV

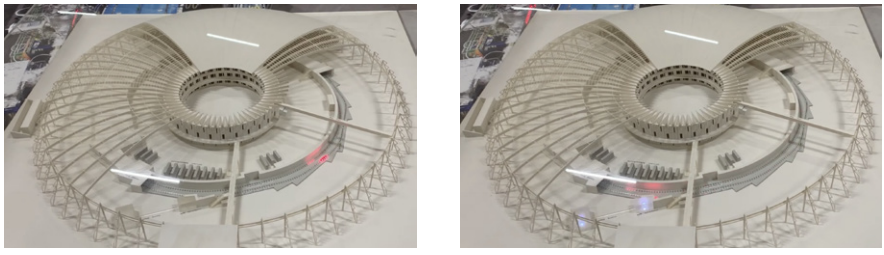

(a) Electron bunch circling in storage ring, marked with red LEDs **(b)** X-rays generated at a beamline, marked with white LEDs

Figure 2.12: Physical model of a synchrotron, Swiss Light Source. Model uses red and white light to represent electrons and X-rays respectively.

X-ray Free Electron Lasers (XFELs) are built on the same principle, but design considerations favour a linear accelerator rather than a circular storage ring. When the wiggler is long enough the emitted electromagnetic radiation will interact with the electron bunch and favour even more emission. Conceptionally, free electron lasers differ from conventional lasers in that the electrons are free and not bound to an atom. As a compensation for the absence of mirrors that work for X-ray wavelengths, XFELS need to be powerful enough that a single pass through the wiggler is enough for lasing to occur. XFELs utilize kilometers long linear accelerators that to achieve this. The number of photons in each X-ray pulse of an XFEL means that the sample will disintegrate upon illumination. Fortunately, the length of time of the pulses, in the tens of femtoseconds range,

is short enough to be able to diffract the sample before it's destruction [79]. The destruction of the sample upon X-ray illumination requires the sample to be continuously replenished. Examples of such sample delivery systems are liquid jets [80], electrosprey [81] and fixed target [82]. Examples of the fixed targets used in **PAPER VII** can be seen in figures 2.13a and 2.13b. The choice of sample delivery method depend on the sample and research question at hand [83].

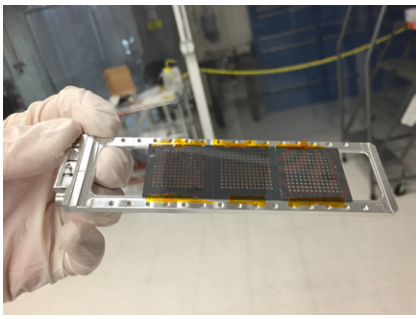

(a) Array of fixed target matrixes

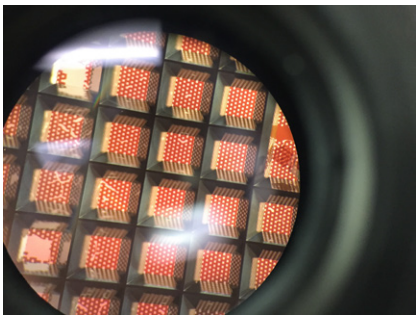

(b) Closeup of support for graphene layers

Figure 2.13: Fixed target for XFEL sample delivery

Important metrics for X-ray sources are photon flux, it's angular spread and how broad the wavelength range of emitted X-rays are. These qualities are often summed up in a measurand called *spectral brightness* or *Brilliance* [84]. This combined measure says something about how the intensity of the X-ray beam is related to its temporal and spatial coherence lengths .

Depending on the temporal resolution needed, sometimes purpose built experimental stations are needed for time-resolved experiments, such as ID09 at ESRF [85] or BioCARS at APS [86]. For slower conformational shifts a more conventional experimental synchrotron endstation can be used [87]. Sometimes a combination of beamline capabilities can be utilized to cover a broader timescale. [88]. The lower limit of time-resolution of synchrotrons is limited to the bunch-size of the electrons in the storage ring, which for current generation facilities is in the range of 100 picoseconds [89]. For the study of faster reactions than this the use of XFELs are needed, for example the study of picosecond structural movements in a photosynthetic reaction center [90].

2.2.5 Fourier analysis

The Fourier transform is a mathematical tool initially developed by Joseph Fourier for analysing heat conduction [91]. Today, Fourier analysis is useful in

a range of scientific methodologies [92–94] as well as image compression [95]. The Fourier transform is also a good representation of what happens with the information about the structure of an objects electron density distribution when an electromagnetic wave is scattered by it. The equations for X-ray scattering involves the use of Fourier transforms.

The Fourier transform is a way to use combinations of sine and cosine-waves to represent any structure. A spatial frequency distribution can be compared to the pairwise distance distribution of electron densities sampled by X-rays in the previous section. Repeat distances in real space corresponds to repeated distances (frequencies) in reciprocal space.

As an example of how important the phases are for being able to reconstruct the image, I've prepared pictures of a brick wall and some foliage showing the differences between phase and intensity and what happens if you lose the phase (fig. 2.14 & 2.15. Figure 2.16 shows an effective example of phasing with the wrong phase. These figures are prepared using the Fast Fourier Transform (FFT) which is much more computationally effective version of the Fourier transform [96].

The phase problem

In practical measurement situations the phases are not measured which presents a challenge for the interpretation. Without the phases there is no unique structure that will fit the measurement data. The phase gives information about the position of the scattering objects. There are a range of methods to tackle the phase problem, including the previously mentioned heavy atom replacement. One approach is phasing using anomalous diffraction [97]. An practical approach is to phase the data using a a low resolution image captured by other means. Another method is to combine a rudimentary knowledge of the structure at hand and a phase retrieval algorithm. Although the methodology of how to construct phase retrieval algorithms have been out there for a long time [98], the implementation of this is plagued with practical issues [99, 100]. The use of phase retrieval algorithms have become paramount in the field of coherent diffractive imaging of non-crystalline samples [101]. A detailed description of the phase retrieval algorithm developed to interpret the data collected for **PAPER I** is provided in section 4.4.

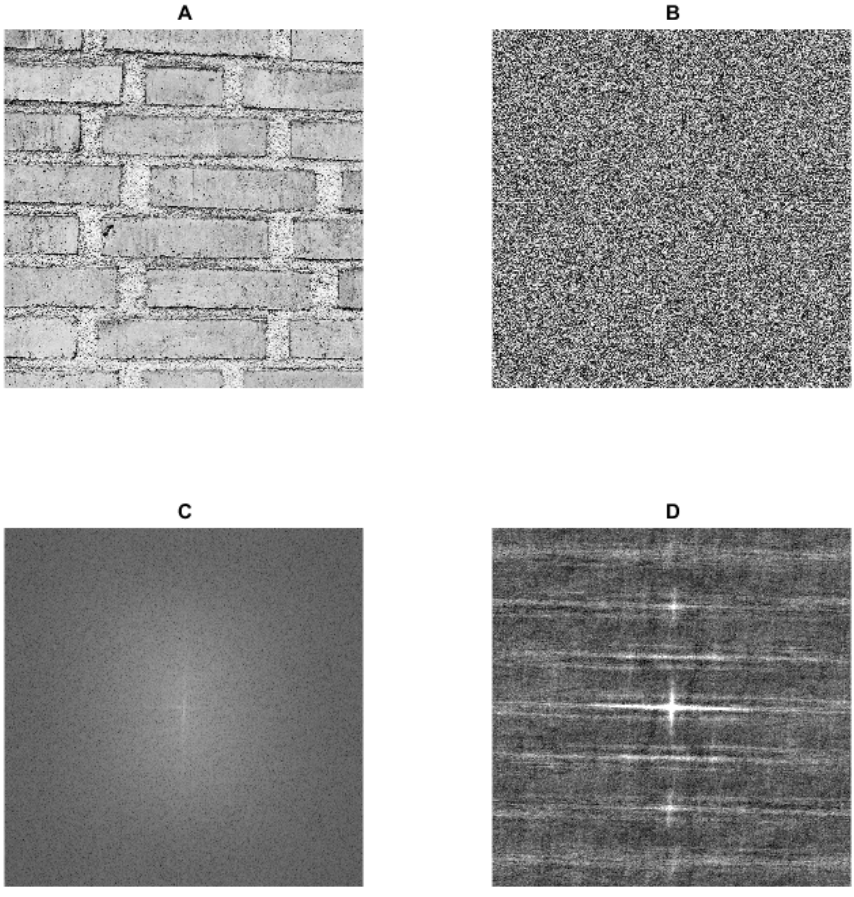

Figure 2.14: Fourier transform of brickwork **A**) Picture of brickwork, **B**) Fourier transform phases, **C**) Fourier transfer amplitudes, **D**) Real space image with phases lost

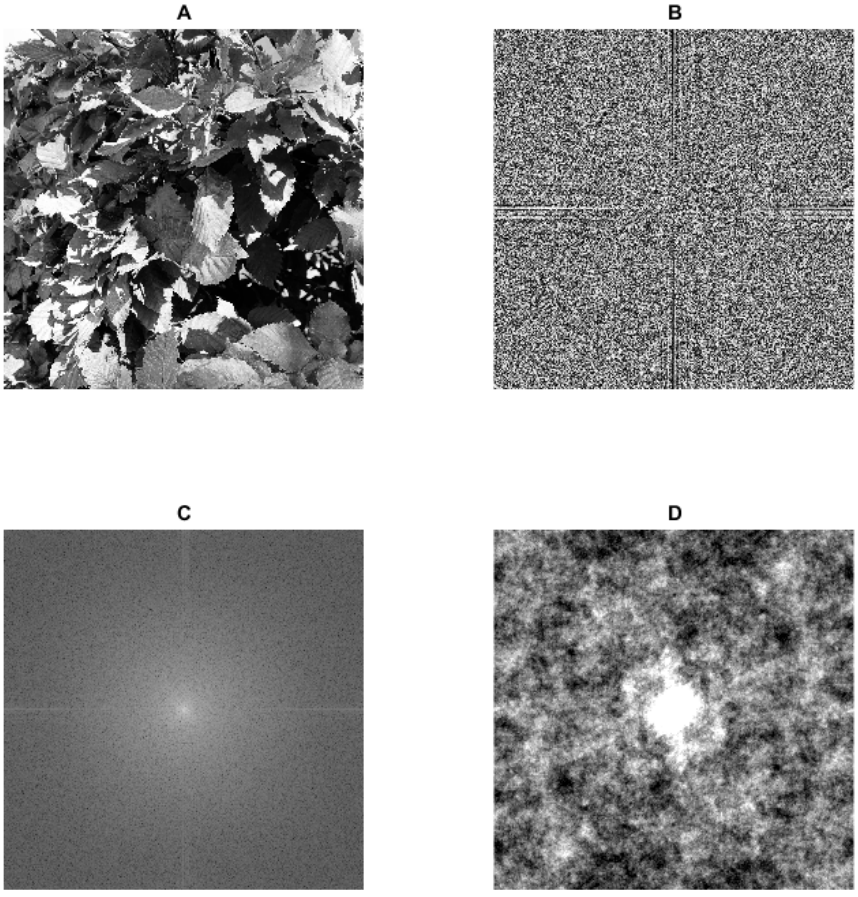

Figure 2.15: Fourier transform of leaves **A**) Picture of leaves, **B**) Fourier transform phases, **C**) Fourier transfer amplitudes, **D**) Real space image with phases lost

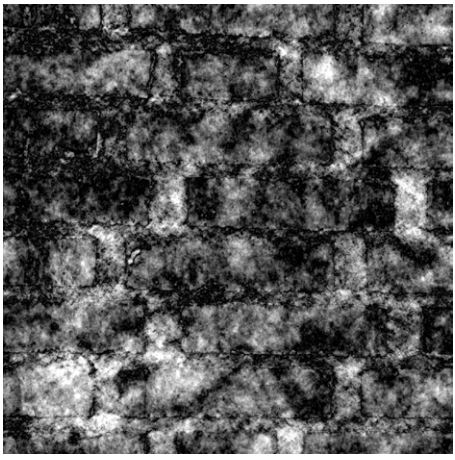

(a) Amplitude of leaves combined with phases from bricks, inverted into real-space

(b) Amplitude of bricks combined with phases from leaves, inverted into real-space

Figure 2.16: A mix-up of phases and amplitudes showcase their relative importance. The general intensity and dynamic range is retained by the amplitudes but the structural information provided by the phases as contrasts enables us to see the brick-pattern among the foliage and the bland brick-colored leaves.

Chapter 3

Cytoskeleton

Investigations and speculations into of how organisms are internally organized have a long history, guided by the tools of discovery available at the time. For a long time a combination of vital fluids where thought to be the essence of life with muscles, bone, organs and ligaments working as structures and vessels for these. But with the the invention of the microscope more detailed and scientific investigations became possible. After van Leeuwenhoek saw fibers composed of smaller filaments in excised cow-muscle a more mechanistic body of theory was developed, where the organism was governed by a succession of ever smaller fibers [102]. In the early twentieth century the need for a cell-skeleton in order to allow cells into have any other shape than spherical was suggested [103]. The wide range of cellular shapes identified would otherwise be in conflict with basic biophysical considerations. The term cytoskeleton was coined by an embryologist who identified the need for an organizing structure within the cells [104, 105]. This was in opposition to the then prevalent idea of organelles freely floating around inside the cells. The existence of such a structure was inferred from eggs ability to reorganize themselves after being squeezed and squished. Polarized light and birefringence measurements on squid nerve fibres showed the existence of cylindrical rodlets with a width smaller than the wavelength of the light and oriented in parallel with the axon [106]. With the advent of electron microscopy it was finally possible to visualize tubular structures in nerve tissue from a range of organisms. These structures were given the name neurotubules [107].The name microtubules was posed since these tubular structures were later found in a range of cell types [108]. This dynamic rearrangement of microtubules during mitotic spindle formation was also identified [109]. Advances in staining procedures for electron microscopy would later allow for the discovery of the ubiquitous nature of microtubules [110].

Today the components of the cytoskeleton in all three domains of life are well described, although many questions of how it is regulated remains. The cytoskeleton in eukaryotes is better understood than it's counterparts in prokaryotes and archea. Indeed, it was long believed that the cytoskeleton was a unique feature for eukaryotes [111]. But since protein homologues for tubulin and actin were found in bacteria [112–114] the view of evolution of cytoskeletal components has expanded. Although primary sequence parity between tubulin an its bacterial homologue FtsZ is fairly low, the structures show a remarkable similarity which indicates an evolutionary link [115].

The cytoskeleton in eukaryotes has three main components, microtubules, actin filaments and intermediate filaments, which works together to enable cell shape and internal organization, motility, cell division and intracellular transport. Microtubule and actin dynamics are energetically driven by nucleoside triphosphate hydrolysis, while intermediate filaments use other proteins [116].

Actin is the most abundant protein in eukaryotic cells [117]. Monomers of actin can polymerize into helical polymers with two linear strands that wind around each other with a filament diameter of 7 nm. Actin microfilaments are involved in establishing/controlling the shape of the cell boundary. Myosin molecular motors can climb on actin filaments and generate the contractile forces of muscle fibres. Although actin is the dominant component of myofibrils, microtubules are also involved both in the growth [118] and organization of these [119]. Actin filament polymerization growth showcase treadmilling, the addition of subunits on one end of the filament while they are lost on the other end.

Intermediate filaments are thus named since their width lies in between that of actin filaments and microtubules. While the proteins forming both microtubules and actin filaments have conserved primary sequences, the family of intermediate filament proteins differ in both primary sequence and size with the functional organization of an intertwined dimer, coiled coils, being the common structural motif. Intermediate filaments are good at withstanding both tensile and bending stress and form networks and meshes with both microtubules and actin filaments, as well as connecting cells with each other [120].

Microtubules, being the focus of my investigations and that of many researchers over several decades [110], will be described in some detail below.

3.1 Microtubules in vivo

Microtubules are hollow cylindrical filaments with an outer diameter of approximately 25 nm. Microtubules polymerized from sub-units consisting of an heterodimer of the globular proteins α and β tubulin. These two tubulin proteins have a similar amino acid make up ($\approx$ 50% sequence identity) [121]. The cylindrical shape is formed by a helical arrangement of stacked heterodimers, so called protofilaments, bound together laterally with non-covalent bonds. In most cases the number of protofilaments that make up the microtubule is 13, at least in mammals [122]. However, microtubules polymerized in vitro tend to polymerize with a range of protofilament numbers, with 14 being the dominant population [123]. A model of a 14 protofilament microtubule with a 3 start shift is shown in figure 3.1 and 3.2. The designation 3 start shift means that after one full turn a row of subunits connects with the lattice 3 subunits further away from its starting position. Not all microtubules configurations follow a strict helical arrangement of the dimers, it depends on both the shift and the number of protofilaments [124]. Actually, microtubules with protofilament differing by an order of magnitude have been found [125]. Microtubules can grow to lengths of several micrometers. An electron micrograph of a microtubule is shown in figure 3.3.

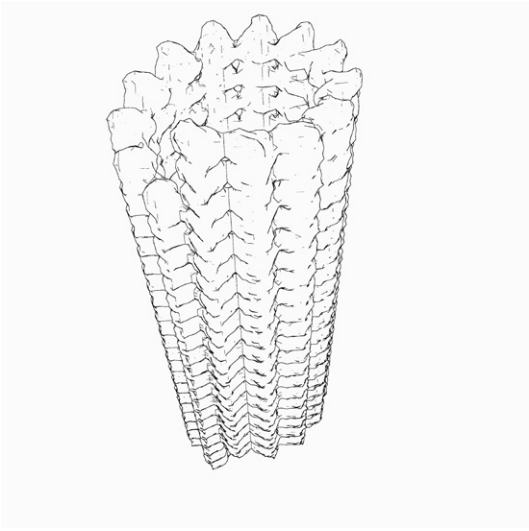

Figure 3.1: Microtubule surface contour, 14 protofilaments, 3 step start, transverse view

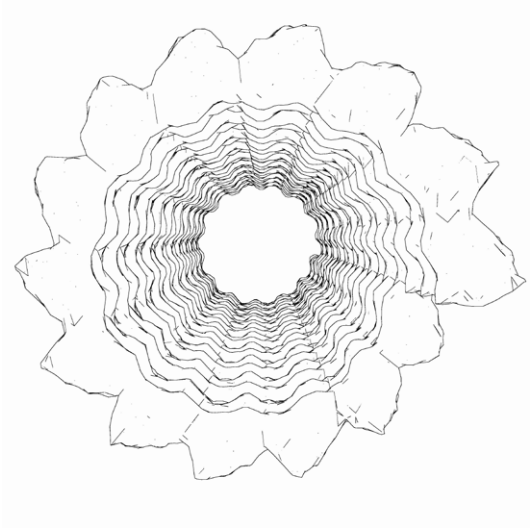

Figure 3.2: Microtubule, 14 protofilaments, 3 step start, longitudinal view

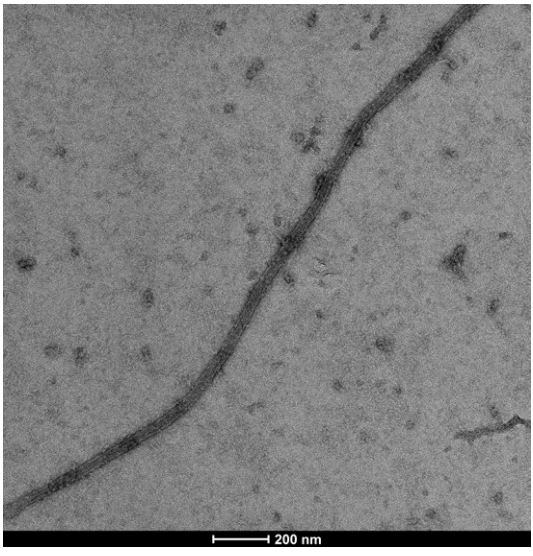

Figure 3.3: Microtubule electron micrograph.

The tubulin heterodimer is approximately 8 nm in it's longitudinal direction and 4 nm wide. The number of dimers in a 1 μm long microtubule is then 14 protofilaments $*$ (1000 nm/8 nm)=1750 dimers.

The polymerization process is dynamic and different compared to the other cytoskeletal filaments. Microtubules predominantly grow from one of their ends, called the *plus end* [126] while being attached to a scaffolding at it's *minus end*. The heterodimer is oriented in the protofilaments such that the α subunit is closest to minus end and the β subunit is closest to the growing end. The assymetric electrostatic distributions of the α and β tubulins gives the heterodimer and the microtubule as a whole polarity. Sometimes the growth is replaced by rapid depolymerization. This behaviour is called dynamic instability, which will be described in more detail below. In the cell this process is regulated and tuned by other molecules, so called Microtubule Associated Proteins (MAPs), as well as a host of Post Translational Modifications (PTMs). Hydrolyzation of GTP is utilized to fuel this dynamic process.

Microtubules serve a variety of functions in the eukaryotic organism, with a wide range of cellular process relying on proper microtubule function. A range of disorders are connected to malfunctioning microtubule processes. Several neurological disorders have been shown to be connected to mutations in genes coding for different tubulin isotypes [127] or MAPs/PTMs [128]. In many cases it is different microtubule isotypes that perform the different functional roles, although a host of PTMs and interactions with MAPs are also involved. This is a prime example on how structure and function of proteins are intertwined.

Microtubules are the stiffest components of the cytoskeleton, with a Young's modulus and persistence length comparable to carbon nanotubes. Although the available techniques have evolved over the decades [129–131], the reported values differ by an order of magnitude and is dependent on both measurement method and specific sample preparations [132]. Regardless of the uncertainty in numbers it is important to note that microtubules are stiff enough to span the width of a cell. Since the different cytoskeletal species often work together in the cell it is important to try to study the mechanical interplay between them, rather than their mechanical properties in isolation [133].

In the cell, nucleation is orchestrated by biological scaffolding structures, Microtubule Organizing Centers (MTOC), such as at the centrosome [134]. Specific isotypes of tubulin are also involved in this initial nucleation step, for example γ-tubulin. Knockout variants without this specific isotype are still able to nucleate though, mediated by MAPs [135].

3.1.1 Functions

Microtubules are functionally heterogenous and are involved in a wide range of cellular processes. A brief overview of microtubule biological functions follows.

Cell division

Microtubules are important in cell division, forming the mitotic and meiotic spindles pulling the chromosomes apart (fig. 3.4).

One of the most common treatment drugs for cancer is paclitaxel, a compound that binds to the tubulin heterodimer subunit and prevents microtubule depolymerization and thus the organization of the mitotic spindles [136]. The effect is related to the search and capture model for the organization of the microtubule connections between centrosomes and kinetochores. The dynamic instability in microtubule polymerization kinetics required for this behaviour is hindered. Paclitaxel has also been used extensively when studying microtubules in vitro, since it stabilizes microtubules at room temperature for days [137]. Originally paclitaxel was derived from the bark of the pacific yew tree and there were environmental concerns about about over harvesting [138]. There are several anti-mitotic chemotherapy drugs that work by binding to microtubules and disrupting cell division [139].

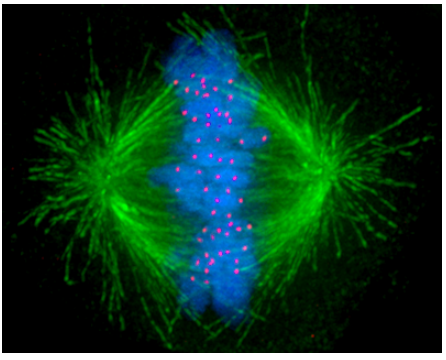

Figure 3.4: Human cell division, mitotic spindle: Microtubules, DNA, Kinetochores. Attribution: commons.wikimedia.org

Cilia and flagella

Microtubules form the structural basis for cellular motility. The axoneme, a structure shared by cilia and flagella, is comprised of a set of doublet microtubules. A doublet microtubule is a merger of two microtubules that share one side of the

cylinder. These doublet can split into two singlet microtubules farther out from the axoneme [140]. Molecular motors such as Dynein can force the microtubule doublets to move with respect to each other, ultimately producing the necessary movement of cilia and flagella [141].

Intracellular transport

Microtubules form cell-spanning networks on which molecular motors transport vesicles. Motor proteins have a preferred direction of travel along microtubules. Generally, kinesins walk towards the plus end of a microtubule, while dyneins move towards the minus end. Both these motor families are ATPases [141,142]. Modelling suggests that microtubules structurally responds to being stepped on, and ease the path forward [143]. Kinesins also transport their cargo along microtubular bundles in axons. Since the molecular motors have a preferred walking direction the polarity of the axonal bundles is important. Polarity here is meant both in terms of elemental charge distribution, electrostics, as well as orientation of how the heterodimers are stacked in the protofilaments of the microtubule since this influences which end of the microtubule is actively growing [144]. The axonal microtubules are stabilized with the protein Tau, which forms a crosslink of sorts between microtubule dimers.

Structural support

Microtubules can form cell-spanning networks which is used upholds the assymetric distribution of protein complexes and organelles. This cell polarity inform for example where growth cones occur [145]. Together with actin filaments microtubules give platelets their unactivated flattened disk shape and enable their rapid shapeshifting into spherical activated state [146]. Another example of the structural use of microtubules is the manchette-structure in shape the sperm heads which help to shape it's hydro-dynamically efficient form [147].

3.1.2 Multi-tubulin hypothesis

How can a single set of proteins be involved in such a wide range of cellular processes? There are several isotypes of tubulins expressed but severe constraints put on the evolution of these by the many structural interactions with MAPs and the range of PTMs have kept them structurally very similar. It was proposed that different isoforms of tubulin were involved in the different cellular processes [148]. However, it seems that many isoforms and PTMs can be interchangable and/or deleted without severe functional consequences [149]. Today, the view is that the isoform populations and modifications are responsible for fine-tuning of microtubule function in different circumstances.

The term *tubulin code* has been used to describe the way tubulin isoforms and PTMs change how the microtubule structure is "read" by the MAPs in the cell. This changes the interactions to serve different functions in the cell [150]. The complexity of this regulation is still not well understood.

Microtubule associated proteins

Microtubule associated proteins is a common name for all proteins that bind to microtubules. A large number of MAPs have been identified and their influence on microtubule function established. This includes the molecular motors such as kinesins and dyneins. Molecular motors either use microtubules as paths when they transport cargo or something to hold onto when exerting force. Another MAP, Tao, binds to neuronal microtubules and stabilizes them by holding on to several dimers [151]. There are also end binding proteins that help the cell identify microtubule orientation. This is important since motor proteins tend to have a preferred walking direction.

Post transcriptional modifications

There is an extensive list of PTMs of microtubules known, including acetylation, detyrosination, deglutamylation, glutamylation, glycation, methylation, palmitoylation, phosphorylation, polyamination, polyglutamylation, polyglycation, tyrosination and ubiquitylation [150]. Some of the enzymes target microtubules and other free-floating tubulin heterodimers. Together these modifications change the interaction landscape of microtubules inside the cell.

Isotypes

The α and β tubulins involved in microtubule polymerization are highly conserved between species, which is less true for specific isotypes performing species-specific functions. Several isotypes have been identified in the human genome and they are expressed to different degrees in different cell-types in different organs [152]. Even the first sequencing of tubulin found evidence of isotypes [153].

An example of this is that the purified tubulin we extracted from bovine brains contained a mixture of a number of different α and β tubulins, see table 3.1. These were identified using mass spectrometry, see section 3.2.3.

An example of a tubulin isotype which uniquely serves a specific function is is β1-tubulin. This isotype of β-tubulin helps form the marginal band, ensuring blood platelet shape and shapeshifting during activation [154]. This isotype is highly divergent from other β-tubulins and seemingly optimized for the severe bending required.

Tubulin isotypes						
α	1b	1c	1d	4a	8	
β	2b	3	4a	4b	5	6

Table 3.1: Tubulin isotypes.

There are approximately 450 amino acids in the tubulin sequences. Most isotypes differ by the c-terminal end. This part of the protein is also where most PTMs happen and and where most MAPs bind. The c-terminal differences are not close the the lateral contact points between dimers. However, different isotypes preferently form microtubules with a different number of protofilaments and have different polymerization rates [155,156]. An example of this is that the subsets of the tubulin isotypes in our purification $\alpha 1B$ and $\beta 2B$ forms microtubules with 14 protofilaments while $\alpha 1B$ and $\beta 3$ isotypes form 13 protofilament microtubules. The tubulin isotype is generally assumed to drive the microtubule structure, but there is evidence that PTMs can effect this as well [157].

3.1.3 Structure

The propensity of tubulins to polymerize into microtubules made them a difficult target for structural studies. While X-ray crystallography on crystals of neatly arranged proteins could produce three-dimensional maps of proteins the search for an ultra-structural model for microtubules was a bit more complicated.

The search for the structure of tubulins and their arrangement within microtubules has produced models with increasing detail over several decades. Improved negative staining techniques gave the first fine structure images of microtubules in 1966 [158]. Tubulin protofilaments induced to form sheets rather than tubules by the addition of zinc turned out to be a good target for electron microscopy. The improved images could be used to phase X-ray scattering data and recreate a better model in 1979 [159]. By using an iterative phase-retrieval algorithm an even better model could be constructed in 1987 [160]. The model building has often been done using various combinations of data collected by X-ray scattering and electron microscopy and crystallography. The addition of zinc to polymerizing tubulins produced a two-dimensional crystal of sorts which was suitable for electron crystallography which gave the first high resolution structure of the tubulin $\alpha\beta$-heterodimer in 1998 [161] (fig. 3.5).

The use of Cryo-EM on tubular microtubules would add even more validity to the full structure, avoiding the need to dock higher resolution images from tubulin dimers into the microtubule structure. The details emerging from these

Figure 3.5: First high resolution Tubulin structure, pdb: 1TUB. α subunit in green, β subunit in red.

structures enabled an understanding of the structural differences between tubulin bound to GTP and GDP [162], as well as interaction sites for MAPs [151].

Microtubules are generally assumed to be hollow cylinders, but in some cases there are intra-lumenar proteins of yet unknown type [163].

The dynamics of microtubule polymerization has been investigated using time-resolved SAXS [164, 165], but there is a lack of high resolution structures stemming from microtubules in solution at physiological temperatures. This is something **PAPER I** tried to address.

3.1.4 GTP

Both subunits of the tubulin heterodimer bind GTP, however it is only the GTP bound to β-tubulin that hydrolyzes shortly after polymerization. ATP can also bind to tubulin and affect the nucleation process, although it binds at a different site [166]. ATP and GTP have similar concentrations in the cell [167]. When GTP is hydrolyzed to GDP it introduces a kink in the heterodimer, a structural change which is energetically involved in driving the depolymerization reaction [168]. It is this structural strain caused by GTP hydrolyzation that enables the structure to disassemble rapidly. The energy expenditure of constantly feeding a network of microtubules primed for instability has to have a purpose. It has been argued that the function of this is for the cell to have the flexibility to rapidly redeploy it's microtubule network. A search and capture model was

developed of how microtubules nucleated at centrosomes find, attach to and are stabilized by kinetochores during mitosis [169]. Microtubules that do not find their target depolymerize and deposits their constituent dimers to the tubulin pool. There are also microtubules originating from the kinetochores and the research into this complexity is ongoing [170]. The current understanding is that growing microtubules retains a *GTP-cap* of not yet hydrolyzed GTP which prevents it's disassembly which makes the whole process reliant on the stochastic nature of hydrolyzation, although models of this shows that the process is quite complicated. MAPs can also influence both the frequency of *catastrophe* and growth rate [171].

3.1.5 Electrostatic properties

Tubulin, and hence microtubules, are charged and polar structures. The long c-terminal tail of tubulin has a chain of predominantly negatively charged amino acids (Glutamate, Aspartate). Microtubules are very large structures with over a million atoms. This made the first calculations of the electrostatic properties require considerable computational efforts [172]. These first estimates of the electrostatic potential excluded the c-terminal end since the structure of these had not been determined at the time. Later calculations indicated that a large part of the charge is indeed localized at the c-terminal end [173]. The isoelectric point of tubulin incorporated in microtubules differs from that of the dimer [174].

There is an interest of using molecular motors and microtubules in building lab on a chip devices for a range of applications [175, 176]. From efforts to improve these kinds of devices actual measurements of microtubule electrophoretic mobility in static fields and rotational alignment in field gradients. Although the numbers reported both deviate from each other and estimated values, this approach have a higher validity [177–181]. Different assumptions with regards to the retarding effects of the viscous environment are made. Some estimates are based purely on the molecules in the microtubule structure and does not take counterions surrounding the microtubule in a physiological environment into account. Counterions would effectively screen the charges. An example of an experimentally derived value of the effective charge per dimer is -23e, which is about half the value calculated from the amino acid sequence alone [177]. Regardless of the uncertainties in numbers it is obvious that microtubules are quite charged and has a large induced dipole moment in field gradients, especially compared to other proteins [182]. There are plenty of experimental validation of electrophoresis and dielectrophoresis.

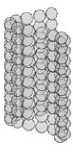

3.2 Microtubules in vitro

As for most proteins microtubule kinetics has been predominantly studied and described in vitro, with the level of understanding evolving with the available methods.

Tubulin was first isolated by utilization of its binding properties to colchicine, a known anti-mitotic agent affecting microtubules [183]. When it was found that Calcium inhibits the polymerization reaction the conditions for polymerizing microtubules in vitro using buffers with a chelating agent such as EGTA (Ethylene glycol tetraacetic acid) could be established [184].

In order to cope with the dynamic nature of microtubules in solution, many experiments use paclitaxel to stabilize the microtubule population. This keeps the microtubules stable even in room temperature. There is also evidence that the addition of paclitaxel to a sample reduces the average number of protofilaments in the microtubules, working both on nucleating and preformed microtubules [185].

3.2.1 Microtubule kinetics

The first studies of microtubule formation were done using electron microscopy or sedimentation assays [186] but these methods have limitations when it comes to following a reaction as it evolves over time. The development of a method where bulk polymerization of microtubules could be monitored using light [36,37] opened up the field and many groups worked to uncover the kinetics of the polymerization reaction. This turbidimetric assay is based on the property that the opacity of a solution changes linearly with polymerized mass as long as the microtubules are longer than the wavelength of the incident light, see section 2.1.3.

Experimentally, tubulin dimers can be held from polymerizing by keeping the temperature low. A heat-jump will then enable the polymerization process. After a brief lag time the mass of polymerized tubulin rises quickly until it reaches a plateau equilibrium value. An example of such a polymerization curve is shown in figure 3.6.

These kinds of diagrams were used to try to build ever more detailed models for the polymerization reaction of microtubules [39, 187–189]. The buffer conditions, required tubulin concentrations and temperatures for nucleation as well as polymerization are well understood [190].

Models of the polymerization mechanism were based on a range of measurands, but a measure of nucleation (e.g. a tenth of the time it takes to reach full

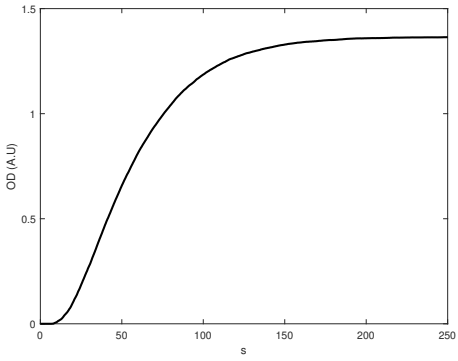

Figure 3.6: Example of a microtubule polymerization time-course measured by UV light scattering, Optical Density (OD) vs. time (s). Density increases only after microtubule length exceeds that of the probing light, in this case 365 nm.

polymerization) and the rate constant of elongation under different conditions were common. These were modifications of the classic condensation mechanism for linear and helical aggregation of macromolecules [191]. Elongation is energetically more favourable and dominates after onset. The lag phase can be interpreted as a measure of the time it takes to form nuclei from which the microtubules can grow. Nucleation is a thermodynamically unfavourable step and stochastic in it's nature. Calculated for the specific experimental setup we used, more than 600 dimers needs to be incorporated in the a microtubule before it scatters appreciably which means that the nucleation can only be measured by proxy.

Several different models for microtubule polymerization was offered before electron microscopy images of fixed samples of microtubules polymerized to a presumed steady-state were found to have a wide length distribution. A new model called *Dynamic instability* was proposed [192, 193]. Dynamic instability means that although the polymerized mass of bulk microtubules remains constant, the individual microtubules constantly depolymerize only to resume polymerization. Video microscopy of individual microtubules showed that this dynamic instability meant that shrinking and growing microtubules co-existed in the same sample [194]. This insight into the polymerization dynamics was only possible after observing single microtubules in action. The polymerization dynamics previously seen with optical density measurements would not have been able to show this feature. The apparent steady state of bulk microtubule polymerization is very dynamic. The rapid depolymerization is called *catastrophe* and when the

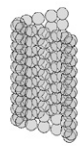

depolymerization halts before completion and growth resumes it is called *rescue*.

The polymerization reaction involves the hydrolyzation of GTP to GDP [195]. The energy gained from this drives the dynamics of the polymerization process. GTP hydrolysis is not necessary for the polymerization reaction but rather involved in the dynamic instability [196]. This was shown using a non-hydrolyzable analogue to GTP, GMPCPP, which polymerized fine.

The polymerization rate is not diffusion limited [197] but is constrained by physiological factors such as MAPs and PTMs [171]. Reported values for polymerization rate in vivo, though varying for species, cell type as well as cell cycle phase, often far exceeds those achieved in vitro. By imaging single microtubules at high resolution it has even been shown that the growth rate varies quite a bit as a single microtubule grows [198].

Glycerol is often used as a crowding agent [199] when polymerizing microtubules in vitro [200]. It substantially lowers the critical concentration for spontaneous nucleation [201]. By a combination of crowding agents and select MAPs the growth rate has been pushed close to the theoretical limit [202].

The search for a good model of microtubule polymerization kinetics continuous using modern methods such as TIRF microscopy and optical tweezers [198,203] as well as sophisticated analytical models including the influence of MAPs [168, 171]. The exact nature of microtubule nucleation and growth in vitro is not known.

A simple analytical model of bulk polymerization kinetics

There has been a range of kinetic models developed for the polymerization of microtubules, each assuming a different number of stages of both nucleation and growth and interaction partners. However, we found that a simplified model of microtubule kinetics was sufficient when analysing our data of bulk polymerization kinetics. Whilst this model was in the end not necessary for the interpretation of our results, it managed to completely match our measurement data (fig. 3.1). The model includes a couple of assumptions; microtubules will only be opaque at a certain size set as a tenth of the final length, nucleation is slower than elongation, polymerization continues until all dimers are incorporated into a microtubule. This kinetic model of microtubule polymerization was implemented in MATLAB [204] as a two step process of nucleation and elongation with their respective forward,f, and backward,b kinetic parameters. The forward reaction depends on both microtubule concentration [MT] and dimer concentration [D]. Forward and backward reaction rates where set separately for nucleation and elongation with a step-function over the size (i) range. Reaction

rates were further multiplied by a temperature analog mimicking the actual temperature equilibration during an experimental run. Microtubule concentrations at specific sizes where transformed into opacity by multiplying their respective concentrations with a step function to account for the property that the opacity of microtubules sharply increases when their length surpass the wavelength of the probing light.

$$\begin{aligned}[\mathrm{MT}]_{\mathrm{i,t+1}} = [MT]_{\mathrm{i,t}} + f_{\mathrm{i\text{-}1}} * [MT]_{\mathrm{i\text{-}1,t}} * [D]_{\mathrm{i\text{-}1,t}} \\ - f_{\mathrm{i}} * [MT]_{\mathrm{i,t}} * [D]_{\mathrm{i,t}} + b_{\mathrm{i+1}} * [MT]_{\mathrm{i+1,t}} - b_{\mathrm{i}} * [MT]_{\mathrm{i,t}}\end{aligned} \tag{3.1}$$

In order to illustrate how relative changes in the kinetic parameters change the shape of the polymerization reaction curve we implemented a range of simulations where the proportions between parameters where changed. It was possible to match experimental data using different sets of kinetic parameters, however it works equally well to implement a realistic temperature change during the time-course of the experiment. This worked for all the different experimental conditions we measured with the exception of a set of measurements done at low temperature. We believe this is due to the low temperature being outside the domain of normal polymerization kinetics.

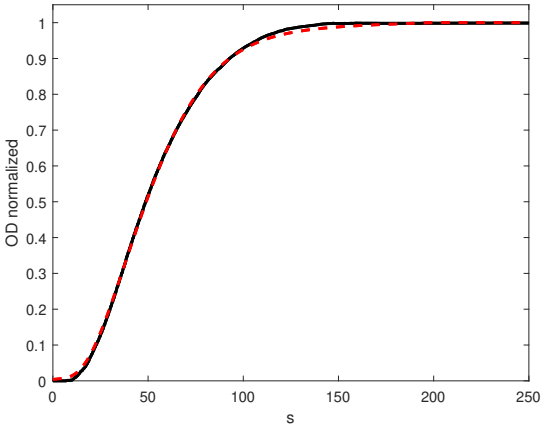

Figure 3.7: Microtubule polymerization time-course, matching model curve in red

3.2.2 Purification

The process of extracting microtubules from mammalian neural sources has been established for a very long time [186]. The purification requirements differ somewhat between species but all utilizes the innate propensity of tubulin to polymerize under the right circumstances. Sometimes the optimal pH of the solutions is different for different species [205]. Most purification methods hinges on an initial concentration of tubulin high enough to be able to initiate polymerization, which restricts the methods to neuronal sources.

It is very important that the brains are very fresh. Reported halftimes of yield is below 20 min [205].

> "For this ghastly experimenting it was necessary to have a constant supply of very fresh human bodies; very fresh because even the least decay hopelessly damaged the brain structure..." *H.P. Lovecraft, Herbert West - Reanimator*

We have used a modification of a purification protocol devised to produce tubulin without associated MAPs [206]. This protocol utilizes a set of high molarity buffers and is based on consecutive cycles of ultracentrifugation. The protocol also incorporates a substantial concentration of ATP which is used to drive ATPases such as the molecular motor Dynein "off the cliff". In addition to the original protocol we have determined that the addition of a protease inhibitor (Protease Inhibitor cocktail, 5 ml, Sigma Aldrich) to the mixture before the first centrifugation step produced a higher yield.

The protein is purified by controlling tubulins innate propensity to polymerize or depolymerize in specific conditions. In order to get tubulin to polymerize one has to supply the appropriate buffer conditions, warmth and enough GTP to sustain the polymerization process. For the depolymerization of microtubules the most effective means are to lower the temperature and to add calcium to the buffer solution. Centrifugation enables us to separate the sample into fractions based on density. This, together with the option to shift tubulins state from depolymerized to polymerized means that one can selective remove everything unwanted while keeping the protein of interest. Two cycles of polymerization-depolymerization is enough to purify tubulin from native sources such as calf or pig brains. An overview of the purification protocol is provided in figure 3.8.

The protocol uses two different buffers to control the tubulins propensity to polymerize, a Depolymerization Buffer (DB) and a High Molarity Pipes Buffer (HMPB), see 3.2. Stock solutions of ATP and GTP was also prepared. All reagents were supplied by Sigma Aldrich.

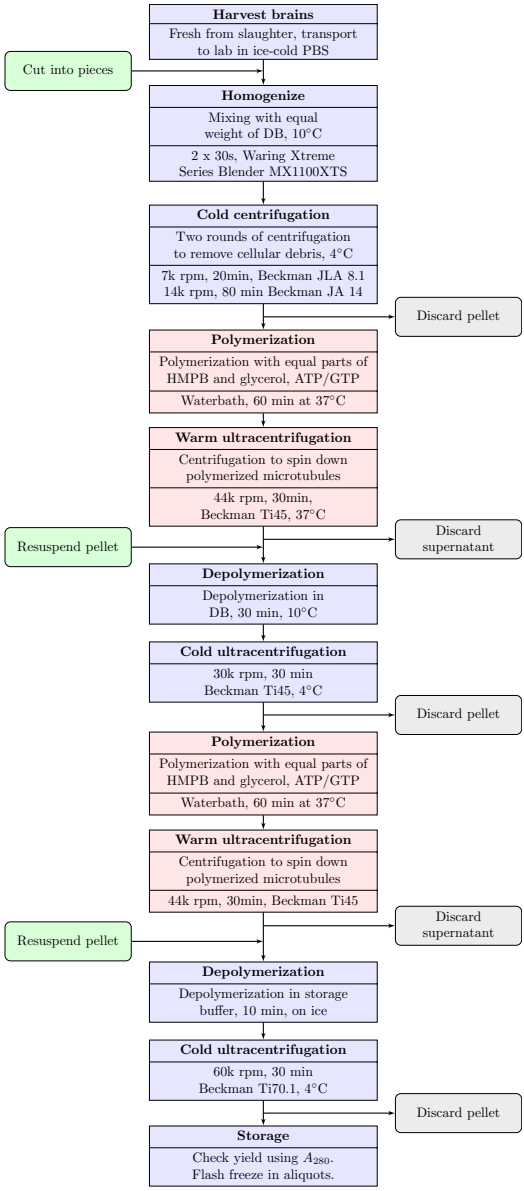

Figure 3.8: Microtubule purification flowchart. Depolymerization Buffer (DB). High Molarity Pipes Buffer (HMPB).

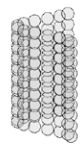

Depolymerization Buffer	
MES	50 mM
$CaCl_2$	1 mM
pH	6.6
High Molarity Pipes Buffer	
PIPES	1 M
$EGTA_2$	20 mM
$MgCl_2$	10 mM
pH	6.9
GTP and ATP stock solutions	
ATP	100 mM
GTP	200 mM
pH	7.5

Table 3.2: Purification buffers

In short, tubulin was extracted and purified from bovine or porcine brains provided fresh after slaughter (approximately 40 minutes) by Dalsjöfors Meat AB. The brains were transported from the slaughterhouse to the laboratory in ice-cold PBS (Phosphate Buffered Saline) to slow down protein degradation.

The brains were cleaned from blood clots, cut into chunks and weighed (fig. 3.9).

Brains, DB and protease inhibitor cocktail were put in a blender in equal weight to be homogenized (fig. 3.10a). Both these first steps were done in a cold room.

The homogenate was then centrifuged in two steps to remove cellular debris. First in a Beckman JLA 8.1 rotor (7000rpm, 20 min) after which the supernatant was transferred to a Beckman JA 14 rotor (14 000 rpm, 80 min). Both centrifugations set to 4°C. The second supernatant (fig. 3.10b), was then mixed with equal parts of pre-warmed HMPB and glycerol, as well as ATP and GTP to a final concentration of 1.5 mM and 0.5 mM respectively. The polymerization solution was then incubated at 37°C for 1 hour in a water bath.

The polymerized microtubules were then pelleted using a Beckman Ti45 (44 000 rpm, 30 min, 37°C). The pellet was resuspended in the DB using a pestle. The resuspension was done with the tubes held in ice after which the solution was kept in the cold room at 10°C for half an hour. After this a second centrifugation step was done where the supernatant was kept. A second run of polymerization

Figure 3.9: Porcine brains to be cut into pieces.

with equal parts HMPB and glycerol supplemented with ATP and GTP was incubated in a water bath for 1 hour. The polymerized microtubules were then again pelleted using a Beckman Ti45 (44 000 rpm, 30 min, 37°C). The pellets were again resuspended but this time in General Tubulin Buffer (Cytoskeleton) and kept on ice for 10 min. The final ultracentrifugation step was done in a Beckman Ti70 (60 000 rpm, 30 min, 4°C). Finally, the purified protein solution was divided into aliquotes, flash frozen using liquid NO_2, and placed in a $-80°C$ freezer for long term storage. The protein concentration was determined with a Nanodrop using the A_{280} assay, see section 2.1.3. Since the protein concentration we achieved was usually quite high, in the range of 30-50mg/ml, the concentration measurements were done with a dilution series.

A note about centrifugation

Centrifuges are heavy and hard working but essentially brittle machines requiring constant maintenance and frequent service. This requires an understanding of the fundamental mechanisms of what one tries to achieve with the centrifugation since it is often necessary to switch rotors and as a consequence the rotation speed. There are simple ways to calculate the *clearing factor* or *k-factor* of a specific ultracentrifugation setup. The sedimentation time is dependent on the angular velocity of the sample which is determined by the inner and outer

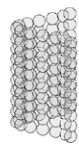

(a) Homogenization of brains.

(b) Cellular debris pelleted.

Figure 3.10: Tubulin purification steps

radius of the angled centrifugation bottle. We also had to adapt the original protocol [206] to the centrifuges and rotors available in our lab environment.

3.2.3 Methods for control

This purification protocol claims to produce tubulin free of MAPs and other proteins which we have confirmed using SDS-PAGE gels and Mass Spectrometry. We have also confirmed the tubulins ability to form nice microtubules with Transmission electron microscopy. I tried using Atomic Force Microscopy once, but since the solution contained glycerol which did not dry properly this attempt failed. The use of an AFM with the option to profile the sample in liquid or a different storage buffer would most probably work better [207, 208].

Electron microscopy

While Cryo Electron Microscopy has evolved technically and is now rivalling x-ray crystallography as the method of choice for obtaining electron density maps for proteins, conventional Transmission Electron microscopy of negatively stained samples is a useful tool for checking that the microtubules have indeed polymerized correctly. The staining procedure adds grains of heavy metals to the surfaces which reduces the resolution to the grain-size. Figure 3.11 shows an example of polymerized microtubules on an EM-grid.

Figure 3.11: Microtubule electron micrograph

SDS-PAGE

The protein purification process can be monitored by saving aliquots and running SDS-PAGE gels (fig. 3.12). The gel-electrophoresis works by separating proteins based on charge, which became proportional to mass by the addition of SDS.

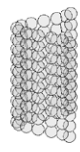

A readymade ladder mixture is run i parallel with the sample for calibration purposes.

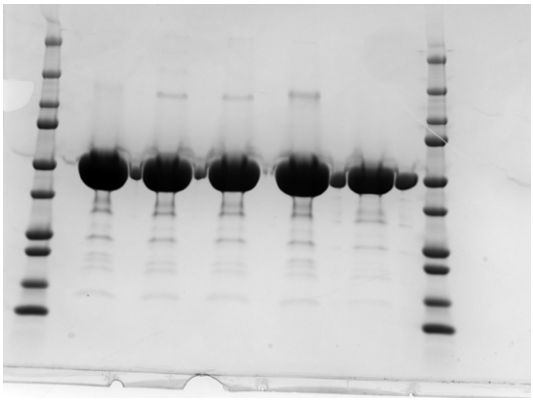

Figure 3.12: Example of an overloaded SDS-PAGE gel with tubulin as the major band. Ladders on the sides.

Mass spectrometry

Further identification of proteins can be done using mass spectrometry. This method works by measuring the mass to charge ratio of the protein cut into shorter peptide fragments. This ratio is then checked against a database. We used this method to check how purified our tubulin was. The purified solution we extracted from bovine brains contained the mixture of tubulin isotypes given in table 3.1, but no known MAPs.

3.2.4 Bovine, porcine and human tubulins

The spread of the mad cow disease and the possibility of it's transmission to humans in the form of Creutzfeldt-Jakob disease made it difficult to work with primary proteins derived from bovine brains. The established tubulin purification protocols, while developed for a range of species, had centered in on using bovine brains as the raw material. These had to be adapted for another source of tubulin. However, purifying tubulin from pig showed could be done easily using the same protocol and gave tubulin with comparable activity [209].

The density ratio of white and grey matter in the pig brain is similar to the human brain [210] and pig brain organisation is similar enough to the human brain for it to be a good model for studying neurodegenerative diseases [211]. Early

structural studies of tubulin actually used the sequence for bovine tubulins, for lack of alternative, while the data was collected on tubulin derived from porcine [161]. Both bovine and porcine core temperature is slightly higher than human core temperature, eg. 38-39 °C. However, tubulins functions over a wide range of temperatures [190] and it is safe to assume that the relevant temperature intervals for tubulin polymerization should be comparable to humans.

3.3 Microtubules and electric fields

Although there is no agreed upon measurements of the intrinsic charge and dipole moment of microtubules, there are is a diverse body of research about potential effects these electric properties might have. Suggestions that proteins in general, and microtubules in particular, interact with and emits electric fields [212]. Most of this interest stems from speculations regarding unique roles microtubules can play in yet unknown cellular functional modes. Microtubules are indeed unusually charged and polar structures and there is a range of theoretical models that investigate the intracellular consequences of having cell-spanning networks of potentially oscillating electrical charges. Simulations of microtubules oscillating (normal mode) shows that they would emit a high frequency electrical field, although too small to measure [213].

Measurements have shown that the conductance in a solution is dependent on the microtubule concentration [214]. A very speculative study claimed for enabling microtubule polymerization in the absence of GTP through the application of alternating electric fields of specific resonance frequencies [215]. Another speculative study using low frequency (217Hz) electromagnetic fields found an influence on the microtubule polymerization reaction [216].

PAPER II and **PAPER III** addresses the possibility of perturbing microtubules function or structure using microwaves.

3.3.1 Microtubules in electric fields

There is an idea that oscillations of microtubules might be sustained by the application of external energy, such as an pulsed [217, 218] or alternating electromagnetic field [219, 220]. These studies are based on molecular dynamics simulations.

3.3.2 Dampening of oscillations

Microtubules are, as previously mentioned, astonishingly stiff fibers able to perform mechanical work as well as function as structural support for other protein

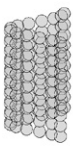

complexes in the cell. There is also, as previously mentioned, an interest in using microtubules for microfluidic applications. Both of these functions requires an understanding of the mechanical properties of microtubules. This view, that microtubules can be seen as mechanical structures like any other, only on a different scale, prompts attempts to understand their properties through modelling. It appears that there is considerable dampening of mechanical oscillations inside a viscous environment such as the cell [221, 222].

A review of possibility of measuring and sustaining these proposed oscillations includes the following quote [223].

> "The large amount of literature assuming that microtubule vibrations are a physical reality, however, is in contrast with doubts about the mere existence of such vibrations in vivo and their possible relevance in biology of cell. We have to ask whether two decades of simulation efforts have brought conceptually new insights or dramatical improvement pertaining to model accuracy."

3.3.3 Tumor Treating Fields

Alternating electric fields of low intensity and intermediate frequency, $\approx$ 100kHz, have been found to disrupt cell division [224]. This has been used to develop anti-mitotic cancer treatment modalities under the name Tumor Treating Fields (TTF) [225]. The mechanism of action is currently unknown, but interactions with microtubules have been suggested as being the origin of an effect [226, 227].

3.3.4 Microtubules and consciousness

Ever since the publication of Nobel laureate Roger Penrose's books *The Emperor's new mind* [228] and especially *The Shadows of the mind* [229] a connection has been made between quantum-mechanical effects in microtubular networks and the *easy problems* of consciousness [230]. Together with an anesthesiologist Penrose developed a theory of how quantum effects might translate into the arise of consciousness called Orchestrated Objective Reduction, *Orch OR*, [231]. However, it has though been argued that the decoherence time-scale would make any quantum effects irrelevant for biological processes [232].

The mode of action of consciousness altering drugs such as anesthetics is not known. Normal mode simulations show that although no specific binding sites for the most common anesthetic drugs are found on tubulin, their binding to tubulin would change their oscillating frequency scaled to the potency of the drugs [233].

Oscillations and coherent motions of protein complexes has been seen as a way to extend the decoherence time enough to enable quantum mechanical influences on protein function. It ought to be possible to measure these oscillations and coherent motions if they indeed exist.

A note about quantum biology

Quantum biology is a label put on biological functions where quantum mechanical effects are instrumental for the function. Several claims on how especially light-harvesting protein complexes rely on quantum mechanical effects have been published [234, 235]. In a foundational way all chemical interactions is based on quantum mechanical effects, but the question is if these effects make a difference on the scale of biology. It has been posed that specific structural arrangements of pigments enable coherence on relevant temporal and spatial scales. However, this interpretation of spectroscopic data and estimated decoherence timescales have also been questioned [236]. And if these effects indeed are physiologically relevant, the question remains if they are evolutionary selected for or just a bi-product of packing several chromophores next to each other, a spandrel of sorts [237].

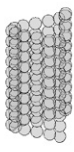

Chapter 4

Coherent diffractive imaging of microtubules using an X-ray laser

PAPER I constituted a stepping stone towards single molecule structure determination of proteins in a more physiologically relevant environment. The goal of being able to resolve the structure from imaging of single particles is to date only realized for very large complexes at low resolution. The reasoning behind this goal is twofold. One would be to be able to capture individual differences in the sample that otherwise would be lost in the averaging and to be able to study dynamics of systems not easily synchronized, both very important aspects that we currently know very little of [238]. Yet another goal would be to see if the structure captured at physiological conditions differ from those rendered by other means.

4.1 Single particle imaging

While X-ray crystal diffraction methods have produced atomistic models of more than a hundred thousand proteins, different tools are needed when protein crystals are unavailable or hard to produce in suitable sizes [239]. The use of slurries of microcrystals is a way around the problem of growing large enough crystals for conventional crystallography [240, 241]. But this approach requires a combination of a multitude of crystals imaged and intense X-rays in order to get enough scattering from each microcrystal. These measurements are conducted at X-ray Free Electron Lasers (XFELs), see section 2.2.4, and the method is called

Serial Femtosecond X-ray Crystallography (SFX). Whereas conventional crystallography includes the illumination of a crystal from different angles sequentially the serial scattering approach relies on the random motions of microcrystals to able to sample the structure completely. But for protein structures that cannot form crystals this approach is untenable. Electron imaging techniques have been successful for solving protein structures generally and are especially useful for proteins that does not crystallize. This approach, however, requires the sample to undergo freezing which raises questions regarding how fully the sampled the protein conformational space can be [242, 243].

Single particle imaging involves the imaging of many proteins separately and the use of a collated dataset to reverse engineer the protein structure, since the information gleaned from a single single particle is not enough. Single particle imaging should really be called serial single particle imaging. Single particle imaging with X-rays is basically solution scattering but with a lot fewer particles imaged at a time. Even though the final structural model is based on an average of single particles, the conformational space can still be assessed [244].

The X-rays available at XFELs are indeed intense enough for recording X-ray diffraction from large biological molecules, typically delivering 10^{12} photons/pulse. The amount of energy deposited into the sample is however enough for it to rapidly disintegrate. A landmark calculation showed the potential of outrunning this destructive force by using short enough pulse-lengths [79], with the term *diffraction before destruction* describing the methodology [245, 246]. A decade later this estimation that diffraction could be attained before sample destruction was first proved [247] and later, with the inauguration of LCLS [248], used for biological samples for the first times [249, 250].

The obvious biological targets for single particle imaging has been large structures such as viruses [251, 252], mitochondria [253] and biological fibres [254]. Determining how diffraction images from particles imaged from different orientations fit together is an arduous task [255].

Fibers with helical symmetries constitute an intermediate approach. The helical assembly means that what is actually imaged is a two-dimensional sheet rolled up into a biological one-dimensional crystal of sorts. The theoretical interpretation of diffraction patterns of axially aligned helical fibres viewed from a perpendicular angle [256] was what enabled James Watson and Francis Crick to discover the structure of DNA [257]. The X-ray diffraction of oriented DNA images were collected by Rosalind Franklin [258, 259]. The diffraction pattern from helical fibers differs both from the Bragg peaks of crystal diffraction and the isotropic patterns of solution scattering. Instead the diffraction is organized in so called layer lines. A related approach which has achieved a considerable increase in

resolution is the imaging of fibers aligned next to each other on a fixed target [82]. High aspect ratio particles such as biological fibers tend to align with the flow due to the shear forces in the liquid jet [254]. The flow alignment is more pronounced in smaller volumes where the ratio between inertial and viscous forces is low, also called the low Reynolds number regime [260].

The benefits of single particle imaging is that the measurement can be done with the sample in solution and at room temperature, the drawback is that the currently achieved resolution is considerably lower than the alternatives.

4.2 Coherent diffractive imaging of microtubules

Tubulins are essential proteins in the cell. These globular proteins polymerize into long hollow tubular structures, several micrometers long, called microtubules. Microtubules constitute an integral part of the cytoskeleton and are instrumental in a wide range of cellular functions, described in detail in 3.1.1. The current structural understanding of microtubules comes from a combination of high resolution models of tubulin heterodimers combined with lower resolution microtubule structures, both approaches using predominantly electron crystallography or imaging, see section 3.1.3. There is a lack of a high resolution structure of microtubules in solution at physiological temperatures.

For this experiment tubulin was purified as described previously, see section 3.2.2, although with the difference that the source of the protein was bovine instead of porcine. The pre-formed polymerized microtubules had to be stabilized using paclitaxel since the measurements were performed at room temperature [137]. Characterization and validation of the integrity of the purification and assembly protocols were made both with SAXS and electron microscopy (fig. 4.1a & 4.1b). The collection of X-ray coherent diffraction images of microtubules were done at the CXI experimental station at the Linac Coherent Light Source (LCLS) at the XFEL in Stanford [261] (fig. 4.2). The sample delivery was done by squirting a liquid jet with pre-polymerized microtubules in front of the X-ray pulses (fig. 4.3). The liquid jet was achieved by using a Gas Dynamic Virtual Nozzle (GDVN) which uses an exterior shell of gas to tune and compress the liquid size [80].

Using the concentration of the sample, the size of the liquid jet and the X-ray beam focus, on average an estimated 20 microtubules were in the imaged volume of $0.16\mu\text{m}^3$. This is not exactly single particle imaging, but far less than the multitudes of protein molecules in microcrystals. Every microtubule also contains thousands of tubulin heterodimers. This is why we call it an intermediate approach. The viscosity of the sample as well as the lengths of the fibres made it difficult to use a smaller jet diameter. A smaller jet is also less stable and harder

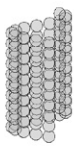

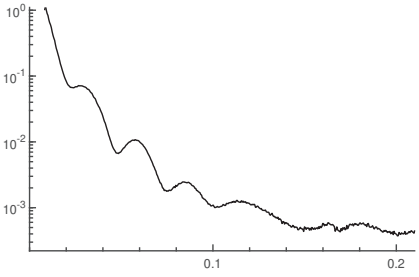

(a) SAXS pattern of microtubules.

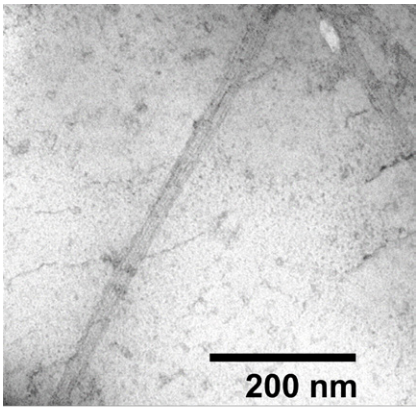

(b) Electron micrograph of microtubule

Figure 4.1: Characterization of microtubule integrity.

Figure 4.2: On the road to LCLS, Stanford.

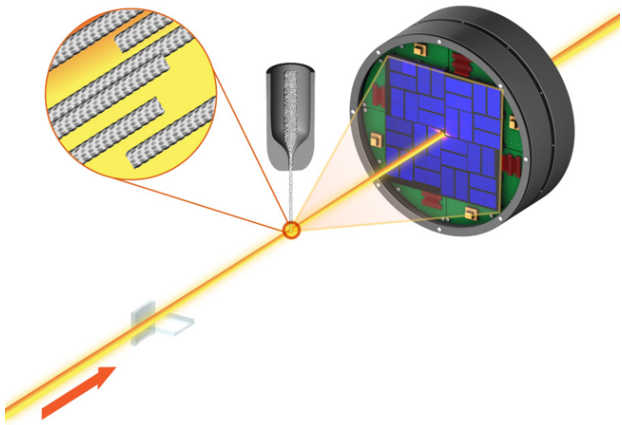

Figure 4.3: Schematic of experimental setup. X-ray pulses hitting a liquid jet sample slurry and diffraction collected at the CSPAD detector.

to hit. Even in the data collected from single X-ray pulses the characteristic equatorial diffraction of helical microtubules can be seen, see panel **a** in figure 4.5.

4.3 Data processing

Approximately one million images were collected in total. An overview of the data reduction and processing is shown in figure 4.4. Out of these million images more than 90 % were not considered for further analysis: either since they did not contain any microtubules or since if the pulse had hit the edge of the jet which gives a dominating edge scattering diffraction pattern. Initial data sorting was done with the high throughput analysis software Cheetah [262]. Further sorting and classification of images were done with a software suite initially developed for electron microscopy, XMIPP [263, 264]. Images were sorted both on basis of the alignment of the microtubules, represented by the angle of the equatorial diffraction, as well as the signal to noise ratio. The resulting image classes were averaged and a subset of these with the highest signal to noise ratio were rotated and again averaged into a final composite image. The result of this averaging of the best 1% of the collected data was that diffraction at the 4 and 2 nm layer lines became visible. Finally, in order to remove the effect of the gaps between the detector panels, Gaussian functions were fitted to the diffraction spots. Figure 4.5 shows how the data quality improves with every step on the way.

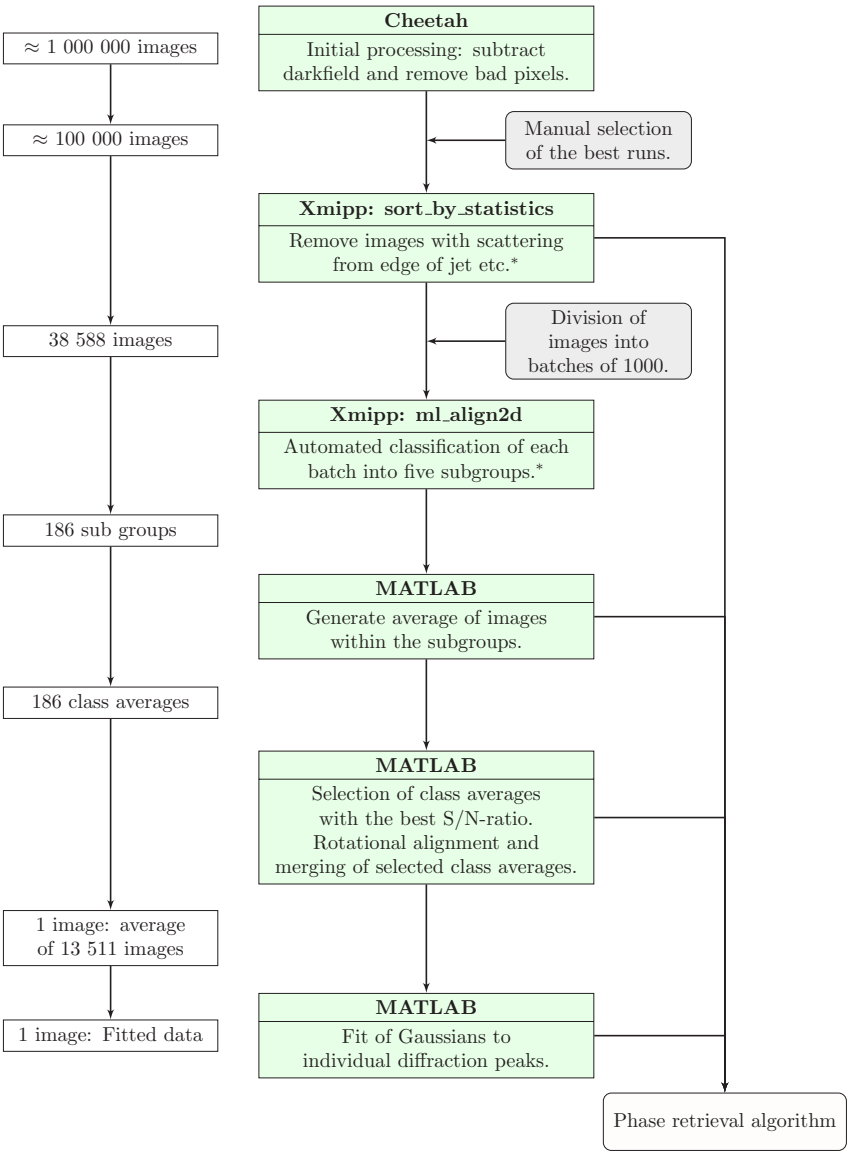

Figure 4.4: Overview of data processing steps. Inital sorting using *Cheetah*, followed by classification by *Xmipp* and merging using *MATLAB*.

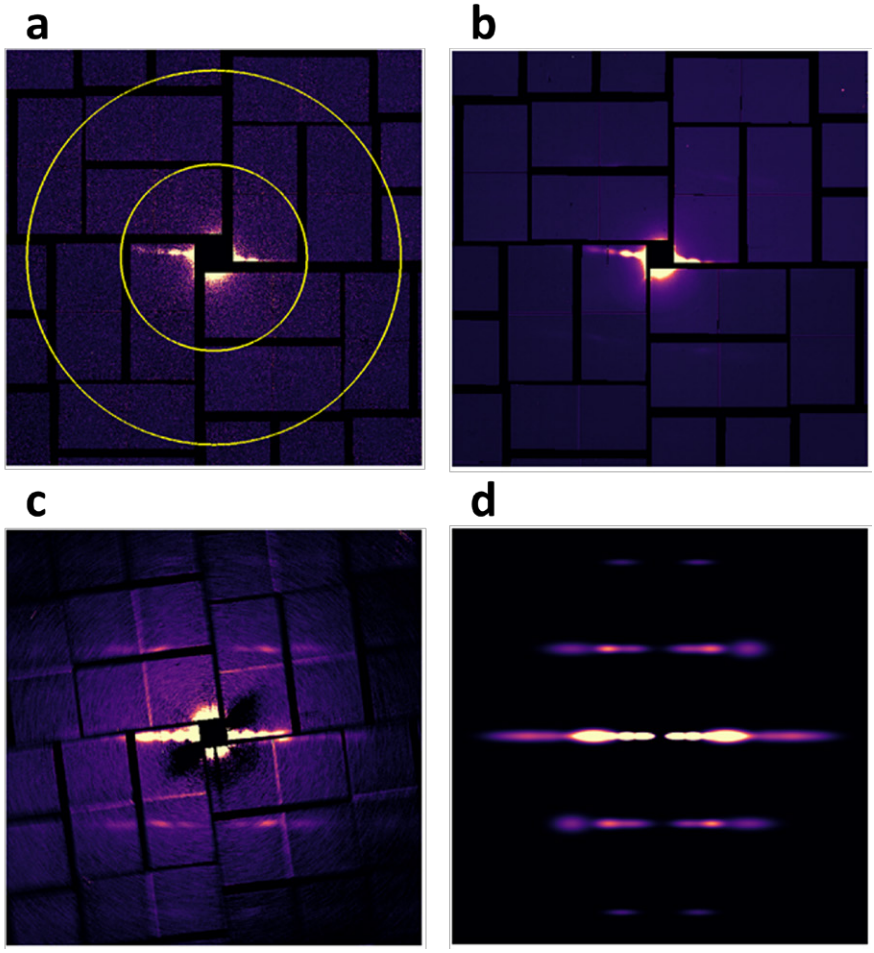

Figure 4.5: Data from different steps of the data reduction: **a**) single frame with circles denoting a resolution of 4 and 2nm, **b**) single class average, **c**) average of all groups, **d**) optimized image with Gaussian profiles fitted to diffraction data.

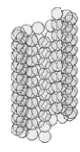

4.4 Image reconstruction

In order to reconstruct the real-space image of the imaged microtubules a simple phase reconstruction algorithm was developed and implemented in MATLAB [265]. Figure 4.6 provides a flowchart of the algorithm. Phase retrieval algorithms have been around for a very long time [98] but are still tricky to implement [99]. The algorithm also requires a basic knowledge of the structure one seeks so that some starting assumptions can be made.

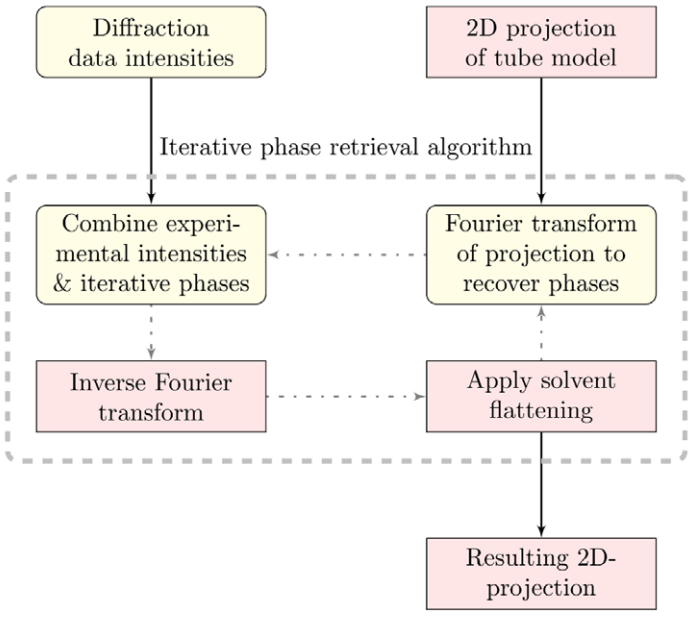

Figure 4.6: Phase retrieval algorithm overview. Pink boxes signifies real space and cream colored boxes reciprocal space.

One such assumption is that the electron density is zero outside the structure. This solvent flattening was achieved by creating a transverse top-hat support function falling of as half Gaussians that forced the real-space projection to zero a bit outside the width of the microtubules we were looking for. Another Gaussian shaped support that mimicked the intensity of the X-ray pulse was imposed in the longitudinal direction. Once the algorithm had converged, this second support structure could be used to invert the final projection and recreate the tubular structure. Another input into the phase retrieval algorithm was the initial phases. For this end a 2D density-projection of a featureless tube was used

(fig. 4.7). Since the measurement did not record the forward scattering we had to supplement our data with a central peak. We borrowed this from simulated scattering from the featureless tube, scaled to the subsequent peaks along the equatorial diffraction line in our data. In order to improve convergence of the

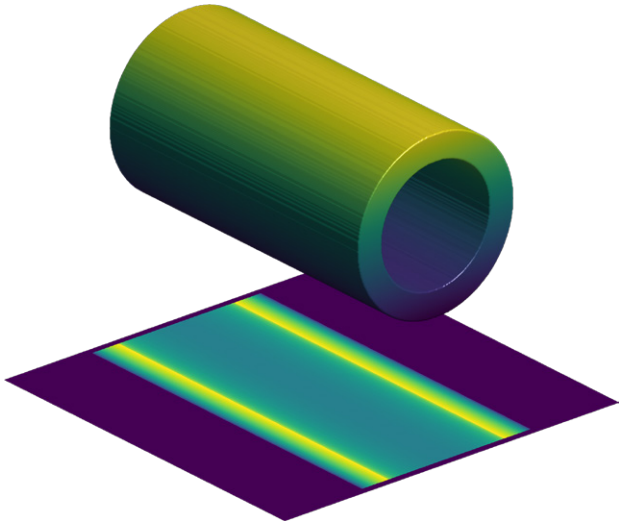

Figure 4.7: Featureless tube and it's 2D density projection

algorithm an inversion of the real-space projection was implemented every 10 rounds of the cycle.

We used this algorithm on the sequential steps of data optimizations of our dataset (fig. 4.5) and the resulting 2D real-space projections showed similar improvements (fig. 4.8).

4.5 Results

It is clear that a reconstructed projection of a tubular structure is possible from even a single shot image, see panel **a** in figure 4.8. However, it is also clear that the features we can reconstruct from the merged and optimized image are more defined. Both the width of the tube and the distances between dimers are physiologically relevant. Although the resolution we achieved here is not high compared to the atomistic models of microtubules achieved using other methods, this is a significant improvement compared to other attempts at single particle imaging in physiological conditions.

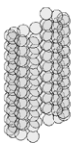

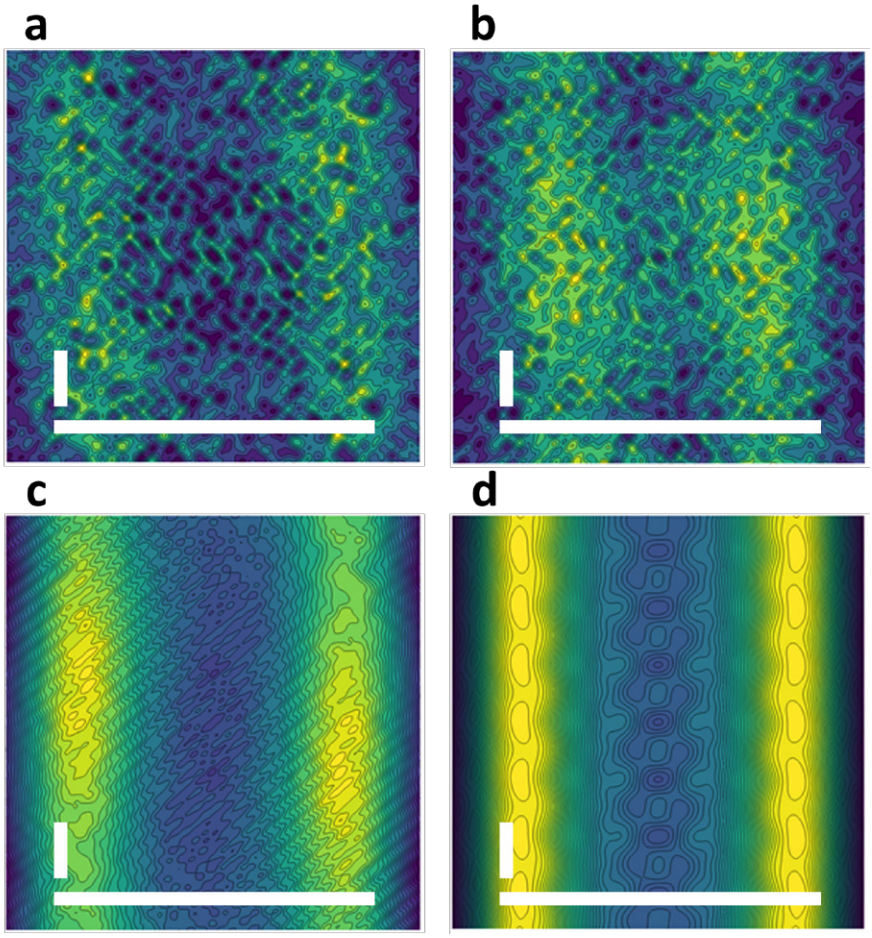

Figure 4.8: Final real-space projections from: **a**) single frame, **b**) single group average, **c**) merged group averages, **d**) optimized image. Scalebars represent 25 nm and 4 nm respectively.

In order to understand the effects of imaging a few rather than single microtubules, and then averaging the images into a optimized composite, we created simulated diffraction patterns of a simplified microtubule model (fig. 4.9 & 4.10). When we used the simulated diffraction patterns in our phase retrieval algorithm we could recreate an even more detailed projection, see panel **a** and **b** in figure 4.10.

A composite of the microtubule sphere model over a range of axial rotations, panel **c** in figure 4.10 would produce a reconstructed projection very similar to our final result, panel **d** in figure 4.8.

4.6 Robustness

It is important that the inputs into the phase retrieval algorithm is close enough to the correct structure, but one should also be careful not to supply too much information since that could steer the result. In order to handle this and explore the algorithms sensitivity to the input and constraints we subjected the algorithm to a range of robustness tests. The algorithm benefited from but was not sensitive to the parameters of the two different support functions for solvent flattering. The rate at which inversion symmetry was imposed was likewise varied and the resulting projections were the same although the number of cycles necessary varied. The parameters of the featureless tube that supplied the initial phases, inner and outer diameter, was also varied. For a range of center of mass (COM) radius the projection converged to a COM distance of $\approx$ 20 nm (fig. 4.11a). COM is a better measurand than outer diameter when comparing 2D density projections.

We also calculated the Pearson correlation of a Fourier transform of projections using a range of starting radii for the initial phases against the equatorial diffraction line in our merged average, panel **c** of figure 4.8 (fig. 4.11b). The figure shows a broad distribution which centers on 11 nm. A comparisons can be made with a Cryo-EM image of a 13-3 pf microtubule (pdb entry 5SYF [266]) which yields a COM radius of 11.2 nm.

By azimuthally integrating the merged dataset (panel **c** in figure 4.8) a comparison can be made against SAXS data for a range of microtubule conformations [74]. The position of the first maxima in the equatorial layer line here points to a protofilament number of 14. It is reasonable to assume that out sample consisted of a mixture of microtubules with different protofilament numbers [123].

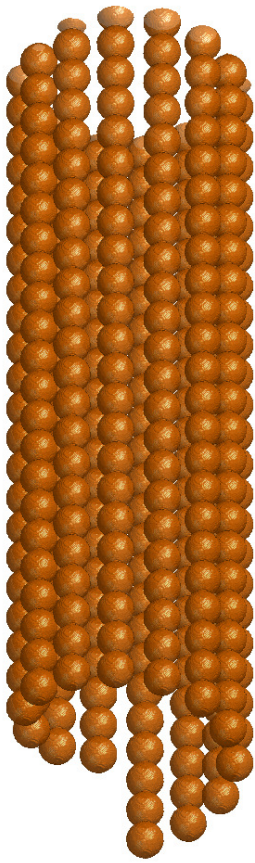

Figure 4.9: Simplified model of helical fiber with monomers as isotropic spheres.

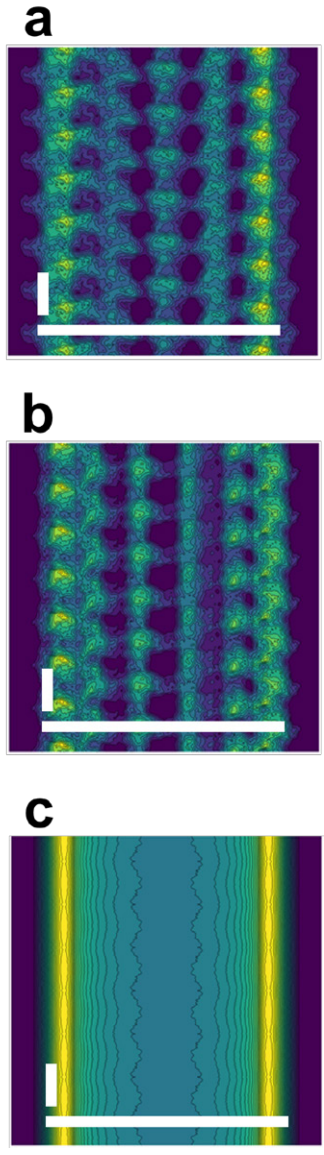

Figure 4.10: Theoretical phase retrieval projections from simulated data. **a**) and **b**) Projections of model viewed from two different angles. **c**) Recovered projection from an average of rotated model.

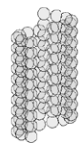

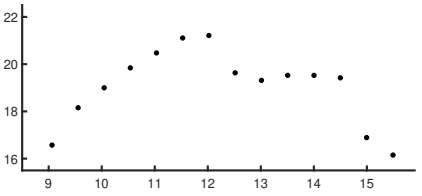

(a) Robustness test for phase retrieval algorithm. The resulting projections center of mass (COM) peak distances plotted against the starting models COM radius.

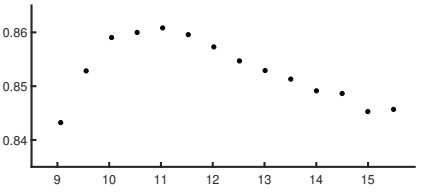

(b) Pearson correlations between data and transforms of projections based on phases with a range of radii (nm).

Figure 4.11: Robustness testing of phase retrieval algorithm.

4.7 Summary and Outlook

In summary, **PAPER I** describes how coherent diffraction data on microtubules was collected, sorted and merged to a point where the 4 and 2 nm layer lines emerged. In order to interpret this dataset a an iterative phase retrieval algorithm was developed. The reconstructed 2D projections showed relevant biological lengthscales. Analysis of our data suggest that our sample consisted of a mixture of microtubules with different protofilament numbers. Microtubules with a different number of protofilaments, and also different helical parameters, will scatter differently [267]. This must also be taken into account if one would be interested in recreating a higher resolution structure.

The dataset and reconstruction show either a low or high resolution depending on what it is compared to. In either case, the structure projections recreated were from microtubules at room temperature and in solution, a step towards physiological conditions.

Simulated data shows the potential of getting higher resolution images if single fibres were imaged. Our experimental data were collected on flow-aligned microtubules. This facilitated the data sorting and merging process, but also meant that in the end we ended up with a dataset consisting of microtubules averaged around the longitudinal axis seen from a perpendicular angle only. This precluded the reconstruction of a 3D structure. However, in order to collect the data required for such an endeavor, an order of magnitude more data needs to be collected. Development in both X-ray intensity, repetition rate and sample delivery systems should enable this. Ideally, such a study might even give structural information about the growth mechanism of microtubules.

Versions of some of the figures in **PAPER I** and this thesis were originally published in the PhD thesis of Rajiv Harimoorthy [268].

Chapter 5

No observable non-thermal effect of microwave radiation on the growth of microtubules

Microtubules are ubiquitous tubular structures formed by the helical arrangement of tubulin heterodimers. Microtubules can form cell spanning networks and serve a variety of functions within the cell, many of which are described elsewhere in this thesis, see section 3. **PAPER II** investigates the effect of microwaves on microtubule polymerization kinetics. Our investigations show that microtubule polymerization kinetics is indeed influenced by the application of an electromagnetic field when compared to a control experiment with the same steady state temperature. This apparent enhancement of the growth rate is however completely recovered when compared to a set of control measurements that better recreates the thermal history of the sample. The frequencies of the electromagnetic fields used in this study corresponds to those of the 5G cellular networks currently being rolled out around the world.

5.1 Microwaves and biology

Much of modern technology, including everyday examples such cellular phones and WiFi, emit microwaves. Microwaves is a term to describe electromagnetic radiation in a broad frequency range between 300 MHz and 300GHz. Electromagnetic radiation within these frequencies is non-ionizing, see section 2.1. The

societal concern that microwaves may cause adverse effects on biological systems is to be taken seriously [26]. So far however, research into the possible interactions between these electromagnetic fields and biology has not provided a scientific consensus, although it seems that most studies that have found an effect are neither replicated nor standardized [27, 50]. A review of the literature concerning electromagnetic fields and biology as well as it's proposed interactions with microtubules is provided in section 2.1.4 and 3.3.

Despite decades of speculations regarding electromagnetic fields influence on microtubules [220, 269] the experimental evidence is scarce and questioned on the basis of the damping any induced oscillations would experience inside such a viscous environment as the cell [221]. Regardless of this, due to the presumed substantial electrical charge and inducible dipole moment of tubulin/microtubules they are seen as prime candidates for the interaction with electromagnetic fields.

One well known feature of microwaves is the ability to heat water, see section 2.1.4. This property is what informs current guidelines regarding microwave exposure [44]. The fact that microwaves heat water so well might also obscure a non-thermal effect [270, 271].

5.2 Microtubule kinetics

In this paper the potential influence of an electromagnetic field on the tubulin polymerization kinetics is measured via changes in solution turbidity. Microtubules are polymerized from heterodimers of α and β tubulins. Tubulin dimers are essentially transparent to ultraviolet light with a wavelength above 350 nm. Microtubules however, when their length exceeds that of the probing light, increases the turbidity of the sample solution proportionally to the polymerized mass. The basis for optical density (OD) measurements is described in section 2.1.3. Microtubule kinetics is covered in section 3.2.1.

Three parameters are extracted from the polymerization time-courses, OD, nucleation time and elongation rate. An example of such a polymerization curve can be seen in panel **A** of figure 5.8 where the time to reach 10% of the final OD is marked with t_{10}. The initial elongation phase can be approximated by a power law.

$$O.D.(t) = a \times t^b \tag{5.1}$$

This approximation loses it's validity when the polymerization reaction is near complete and the available dimers in the solution are scarce.

The natural logarithm of both sides of the equation gives the relationship $ln(O.D.(t) = ln(a) + b \times ln(t)$. A log-log plot gives a straight line with slope *b*, an example of which can be seen in panel panel **B** of figure 5.8. The *b* value was determined by fitting a one degree polynomial to the data between 10% and 40% of the equilibrium OD, which is illustrated by the dashed lines.

5.3 Experimental setup

The purification of tubulin has been described in section 3.2.2. Aliquots of purified high concentration tubulin were thawed and diluted with buffer, glycerol and GTP. The composition of the working sample solution was the same for all experiments presented here: 91μM tubulin, vol. 10% glycerol and 2mM GTP.

In order to expose polymerizing tubulin to a parallel plate type field we commissioned a flowcell with a 300 μm thin copper waveguide where a 1 mm quartz capillary could be held between the waveguide and ground (fig. 5.1 & 5.2). The waveguide is terminated with a 50 Ω load at one end. A hole was drilled through the the low dissipation dialectric polymer (Rexolite) so that the capillary could be accessible for imaging.

Figure 5.1: Image of flowcell with waveguide.

Figure 5.2: Schematic of flowcell. a) 50 Ω load, b) hole for imaging. c) connector to coaxial cable.

The flowcell was connected to a commercially available signal generator (Anritsu MG3694C) capable of delivering up to 23 dBm for frequencies up to 40 GHz.

Microtubules undergoing polymerization was followed for a range of ambient temperatures (31.9°C, 34.9°C and 39.1°C), a range of frequencies (3.5GHz, 20GHz and 29GHz) and for the 20GHz frequency a range of power levels (15 dBm, 19dBm and 23dBm).

Since tubulin polymerization requires a temperature above room temperature the waveguide was housed in an insulated and temperature controlled plexi glass box (fig. 5.3a, 5.3b & 5.4). Temperature control was achieved by a constant flow of hot air. Temperature was monitored in two ways. Thermocouples monitored the ambient temperature surrounding the flow cell and an IR camera was used to monitor the temperature at the sample position (fig. 5.5).

The tubulin solution was kept on ice and a liquid plug sucked up to the capillary inside the flowcell via tubing. Based on the tubing's inner diameter and the flow rate it took 7 seconds to reach the measurement spot. Using a faster flow rate or thinner tubing was not possible since both these increased the creation of air bubbles in the capillary.

The volume of the sample is small (5 μl) and the nature of the thermodynamically unfavourable spontaneous nucleation of microtubules means that we see a significant sample to sample variation in the polymerization kinetics. This has also been noticed in previously reported measurements of tubulin polymerization [36, 188]. To handle this sample to sample variation the runs were repeated on average 24 times (N after outlier rejection), see table 5.1. Outlier rejection was primarily done for the runs where bubbles disturbed the measurements.

Since the exposure to microwaves heated the sample by a couple of degrees the box temperature had to be set at a correspondingly lowered temperature in order to reach the target steady state temperature. The power level 23 dBm translates to a power of 200mW and an electric field strength of 8.9 V peak to peak over the capillary which corresponds to $\approx$ 9000V/m. For our small volume of 5 μl this means an exposure of approximately 40kW/kg, which is considerably higher than the ICNIRP guidelines of 2W/kg or 100V/m in this frequency range [44]. The power output of the waveguide is comparable to that of a WiFi router, but acting on a much smaller volume of space.

In order to quantify the amount of emitted and absorbed radiation we measured the transmitted and reflected scattering parameters (S11 and S21) for the RF-device filled with sample as well as empty using a Vector Network Analyser (VNA). The S21 and S11 parameters together show that at 20GHz, when the capillary is filled by sample, 83% of the power is emitted by our parallel-plate

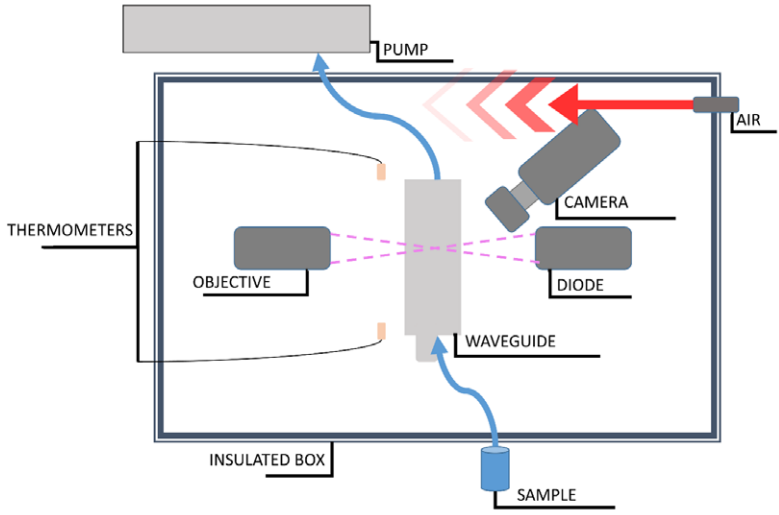

(a) Schematic of the the experimental setup for light scattering measurements of microtubule polymerization kinetics. Objectives focus UV light through the sample capillary. IR camera measures the temperature on the same spot. Thermocouples measure ambient temperature in the insulated box. Hot air flow sets the box ambient temperature. Sample pump is outside of box and sucks up the sample from a container held on ice.

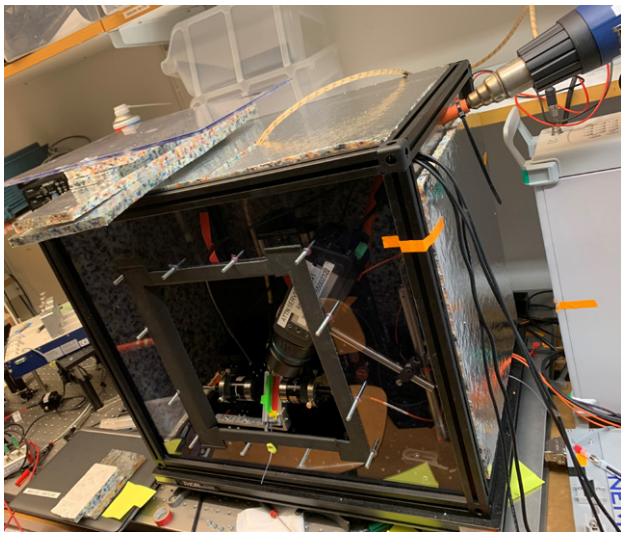

(b) Thermally insulated and temperature controlled box opened up for inspection.

Figure 5.3: Experimental setup. **a)** schematic overview, **b)** picture of insulated box.

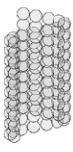

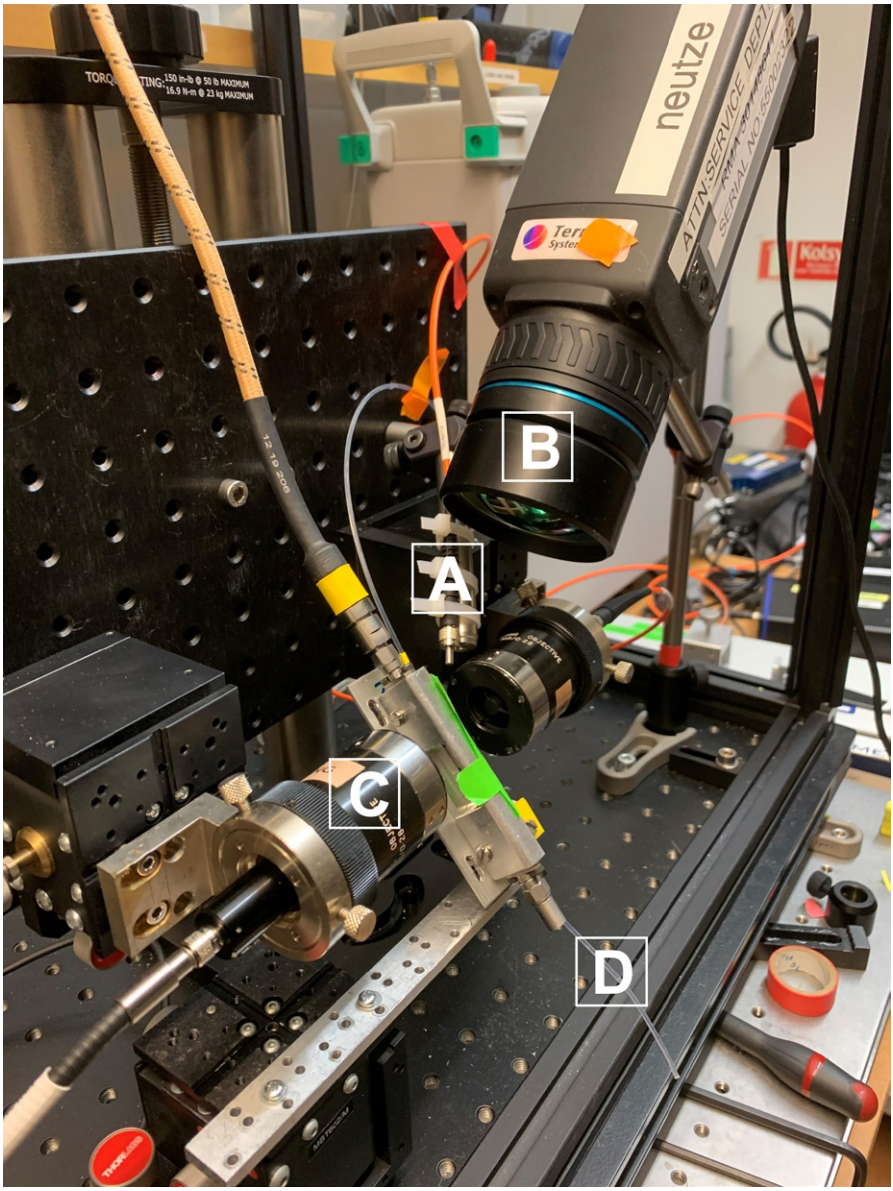

Figure 5.4: Closeup of flowcell inside box. **A**) Fiberoptic for IR laser, **B**) IR Camera, **C**) Optics for UV absorbance measurements, **D**) Flowcell is angled to reduce the length of tubing to outside the box.

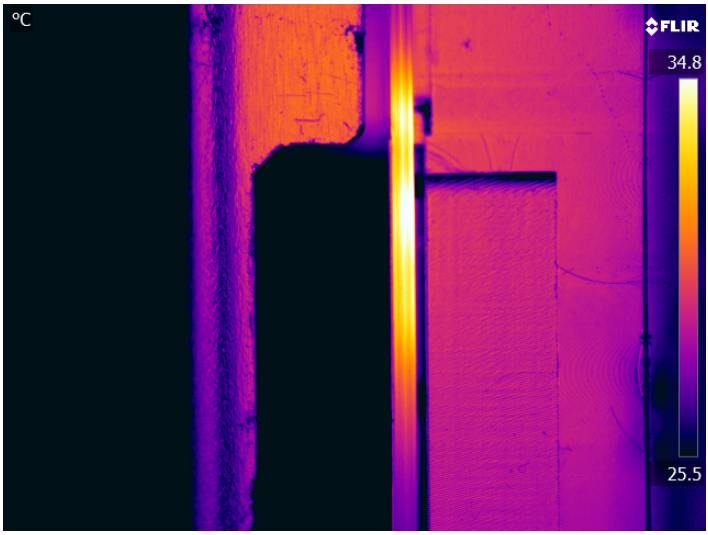

Figure 5.5: Thermal image when using a macro lens

waveguide. On the other hand, when the capillary is empty, this emission decreases to 45% and more of the power goes through to the port capped with a resistor, suggesting a strong power absorption by the sample. S21 and S11 parameters measured for both capillary with sample and empty are shown in figures 5.6a and 5.6b. The measurements with an empty capillary were made for a smaller frequency range.

5.4 Data analysis

The analysis of the polymerization curves included a normalization step where the initial absorption value was set to zero and the final steady state value to unity. The steady state *O.D.*, *b* and t_{10} value was used for statistical analysis using a two component t-test [272] in order to determine if there are any statistically relevant changes in microtubule polymerization kinetics under microwave exposure. The basic parameters of all the measurements are shown in table 5.1. The results of the statistical analysis are shown in table 5.2. Due to the considerable sample to sample variation a stringent delimiter of $p < 10^{-4}$ is used to decide what is to be considered a significant statistical difference.

The kinetic reaction parameters of the polymerization, forward and backward for both nucleation and elongation, can be assumed to co-vary with temperature.

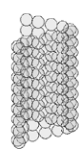

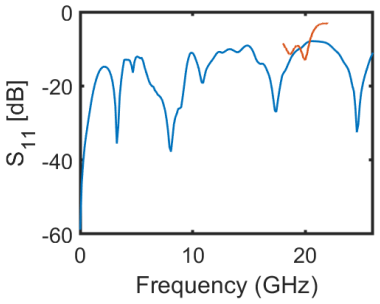

(a) VNA measurement of reflections (S11 parameter) in our waveguide with a capillary filled with buffer for a range of frequencies. Measurements with an empty capillary in red

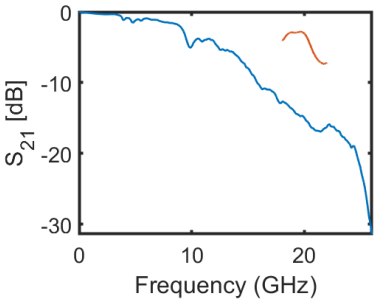

(b) VNA measurement of absorptions (S21 parameter) in our waveguide with a capillary filled with buffer for a range of frequencies. Measurements with an empty capillary in red

Figure 5.6: VNA measurements on microwave waveguide

A linear rescaling of time for a polymerization curve then represents a linear scaling of the kinetic reaction parameters. The basic sigmoidal shape of the curve is assumed to be temperature invariant. We use this temporal stretching to scale curves to see if their shape is different. In practise the stretching was done by re-scaling the time-axis so that the two curves reach the midpoint of 50% of steady state OD, t_{50} at the same time. Examples of such time-stretched curves are shown in panel **C** of figures 5.8, 5.9, 5.12 and 5.13. This procedure changes neither the OD nor the *b* value of the curves, but opens up the t_{10} values for renewed statistical analysis, which are shown under **Stretched* in table 5.2.

	N	OD	$\frac{\sigma_{OD}}{\sqrt{N}}$	t_{10} (s)	$\frac{\sigma_{t_{10}}}{\sqrt{N}}$	b	$\frac{\sigma_b}{\sqrt{N}}$
31.9°C	22	1.04	0.04	63.8	5.8	2.01	0.06
34.9°C	22	1.36	0.04	25.8	1.8	2.21	0.04
39.1°C	19	1.58	0.02	10.6	0.6	2.10	0.06
3.5 GHz 23 dBm	17	1.25	0.04	20.4	1.2	2.20	0.10
20 GHz 15 dBm	20	1.37	0.03	18.1	0.6	2.15	0.05
20 GHz 19 dBm	28	1.42	0.04	20.4	1.3	2.37	0.07
20 GHz 23 dBm	26	1.49	0.03	20.7	0.5	2.99	0.04
29 GHz 23 dBm	29	1.42	0.04	24.0	1.0	3.05	0.07
IR heating	36	1.92	0.01	12.8	0.5	2.95	0.06
Inhom. heating	17	1.69	0.03	17.2	0.9	2.92	0.11

Table 5.1: Average and standard error in measured parameters from experimental data.

Comparison of samples heated (homogeneously) to different temperatures.					
		Measured			***Stretched**
		OD	$\mathbf{t}_{10}$	**b**	$\mathbf{t}_{10}$
31.9°C vs 34.9°C	p-values	$<10^{-4}$	$<10^{-4}$	0.01	0.78
31.9°C vs 39.1°C		$<10^{-4}$	$<10^{-4}$	0.34	0.31
34.9°C vs 39.1°C		$<10^{-4}$	$<10^{-4}$	0.14	0.11
Microwave exposed measurements versus homogeneous heating.					
34.9°C vs 3.5 GHz 23 dBm	p-values	0.05	0.02	0.94	0.35
34.9°C vs 20 GHz 15 dBm		0.82	3×10^{-4}	0.42	0.14
34.9°C vs 20 GHz 19 dBm		0.3	0.02	0.05	0.52
34.9°C vs 20 GHz 23 dBm		0.12	0.01	$<10^{-4}$	0.14
34.9°C vs 29 GHz 23 dBm		0.78	0.38	$<10^{-4}$	0.06
Microwave exposed measurements versus (inhomogeneous) heating from an air stream.					
Air heating vs 3.5 GHz 23 dBm	p-values	$<10^{-4}$	0.04	$<10^{-4}$	0.03
Air heating vs 20 GHz 15 dBm		$<10^{-4}$	0.47	$<10^{-4}$	3×10^{-3}
Air heating vs 20 GHz 19 dBm		$<10^{-4}$	0.06	$<10^{-4}$	0.7
Air heating vs 20 GHz 23 dBm		1×10^{-4}	3×10^{-3}	0.58	0.8
Air heating vs 29 GHz 23 dBm		$<10^{-4}$	$<10^{-4}$	0.32	0.38
Air heating vs 34.9°C		$<10^{-4}$	2×10^{-4}	$<10^{-4}$	0.3
Microwave exposed measurements versus infrared (inhomogeneous) heating.					
IR heating vs 3.5 GHz 23 dBm	p-values	$<10^{-4}$	$<10^{-4}$	$<10^{-4}$	0.02
IR heating vs 20 GHz 15 dBm		$<10^{-4}$	$<10^{-4}$	$<10^{-4}$	3×10^{-4}
IR heating vs 20 GHz 19 dBm		$<10^{-4}$	$<10^{-4}$	$<10^{-4}$	0.69
IR heating vs 20 GHz 23 dBm		$<10^{-4}$	$<10^{-4}$	0.61	0.78
IR heating vs 29 GHz 23 dBm		$<10^{-4}$	$<10^{-4}$	0.26	0.32
IR heating vs 34.9°C		$<10^{-4}$	$<10^{-4}$	$<10^{-4}$	0.25
*Time-parameter scaled so that the mean value was numerically the same as for the control.					

Table 5.2: Two component t-test comparison of growth curve data

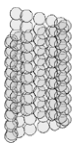

The optical density increases with temperature, as seen in table 5.1. The time-stretch needed to match the t_{50} time points of two curves is related to their differences in OD. A plot of the OD-ratio versus the stretch for a range of experimental conditions is shown in figure 5.7. The Pearson correlation between these two measurands is 0.82.

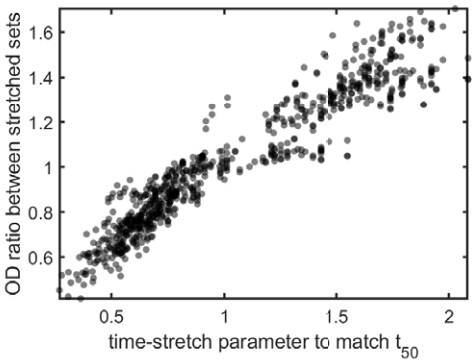

Figure 5.7: Figure shows the linear relationship between the OD ratio of two curves time-stretched to each other together with the stretch calculated to match their t_{50} time points.

5.5 Results

Averaged polymerization curves with an apparent sigmoidal shape for measurements done for two different temperatures, 34.9°C and 39.1°C are shown in panel **a** of figure 5.8. The same dataset as in panel **a**, but with logarithmic axes are shown in panel **b**. The straight line used to calculate the *b* value is marked with a dotted line. As can be seen in both the figure and table 5.1 the t_{10} values are different for measurements done at different temperature, while the *b* values remain similar. The statistical analysis in table 5.2 illustrates this further. The t-test shows statistically significant differences between the different temperature measurements for the OD and t_{10} values while the *b* values are not significantly different. The increase in OD and decrease in t_{to} that we see as the temperature is raised is in agreement with earlier observations [189]. Panel **c** shows the 34.9°C curve linearly time-stretched to agreement with the 39.1° curve. This indicates that the fundamental kinetic parameters are the same, only scaled by temperature. Panel **d** shows the thermal history for the two sample sets.

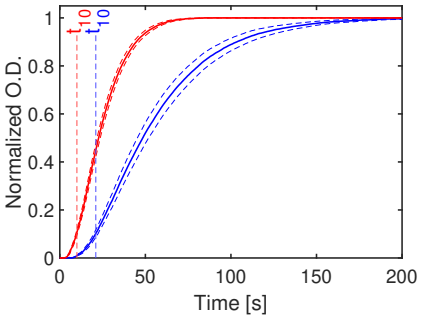

(a) Average normalized polymerization curves, standard error marked with dashed lines and t_{10} indicated

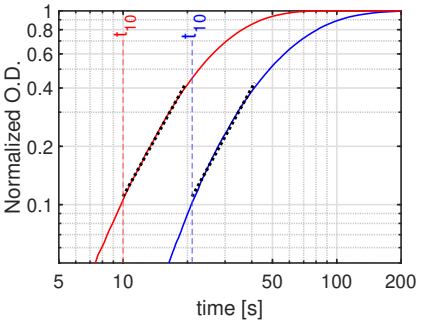

(b) Average normalized polymerization curves log-log plot shows the curves are parallel. Dashed line shows fit to determine *b* value, t_{10} indicated

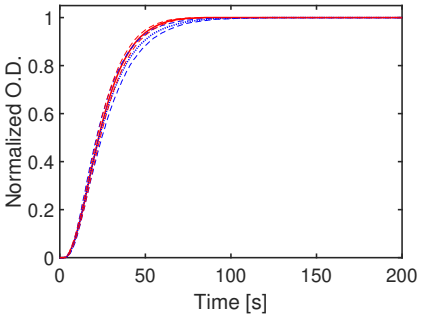

(c) Lower temperature curve linearly time-stretched to match the higher temperature curve.

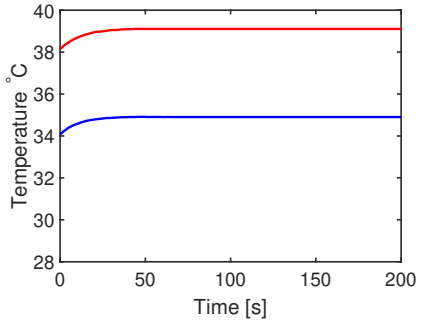

(d) Temperature time-course for the two measurement sets show a different but constant temperature difference.

Figure 5.8: Comparison between two different steady state temperatures, 34.9°C in blue and 39.1°C in red

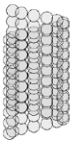

Figures 5.9, 5.12 and 5.13 are organized in the same way as figure 5.8, but compares different sets of the data.

Figure 5.9 shows a comparison between growth curves of the $34.9°C$ set and tubulin exposed to microwave radiation with a frequency of 20GHz and a power level of 23 dBm. The difference between the growth curves is obvious in the log-log plot of panel **b** where they are not parallel and have substantially different *b* values, see table 5.1. This difference is substantiated by the statistical analysis which gives $p < 10^{-4}$ for this comparison and is further illustrated by the mismatch in shape seen in for the time-stretched curves in panel **c**. Panel **d** shows the temperature evolution during the polymerization for the two sets. It is clear that the localized heating by the microwaves give a sharper rise in temperature during the measurement run even if the final steady state temperature is comparable. The parameter values and statistical differences when compared to control, shows very similar results for the 29GHz and 23 dBm measurement set.

For the sets with a frequency of 20GHz but a lower power, 15 dBm and 19 dBm, there are no statistical differences when compared to control according to our criteria. But the there is a trend where our experimental parameters show an increase in the *b* value and a decrease in the t_{10} values when the applied power increases.

This led us to conclude that we indeed found a statistically relevant difference in the growth parameter *b* of microtubules under exposure to microwaves. Especially since this slope of the growth curve in a log-log plot has been previously shown to be unperturbed by a range of experimental parameters [189]. We asked ourselves if this apparent non-thermal effect of microwave radiation could be a consequence of the qualitative differences in the thermal history of the microwave exposed samples as compared to those heated by the ambient temperature in the box. The temperature time-courses in panel **D** of figure 5.8 and 5.9 illustrate the difference between different but ambient temperatures in the experimental box and the local heating effect of microwaves in combination with a slightly lower ambient temperature. The temperature measurements were done at the spot as the OD measurements and it took approximately 7 seconds to transport the sample from ice to this point. It is clear that the sample is pre-heated during this transport phase by the initial temperatures of our temperature traces. This initial temperature history was not available to record.

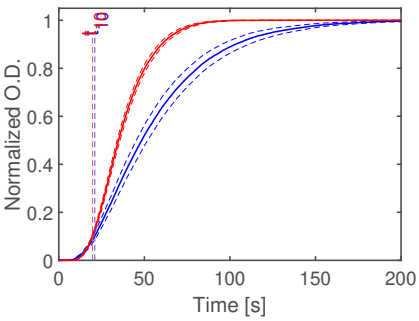

(a) Average normalized polymerization curves, standard error marked with dashed lines and t_{10} indicated

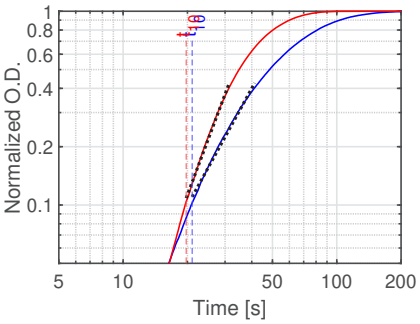

(b) Average normalized polymerization curves log-log plot shows the curves are not parallel. Dashed line shows fit to determine *b* value, t_{10} indicated

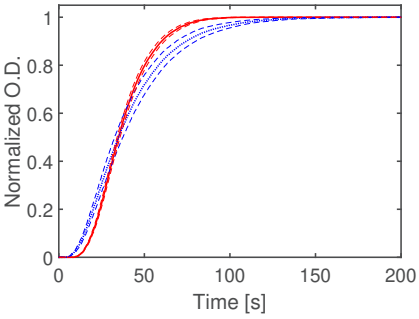

(c) Time-stretched of microwave exposed sample does not match the shape of the 34.9°C sample.

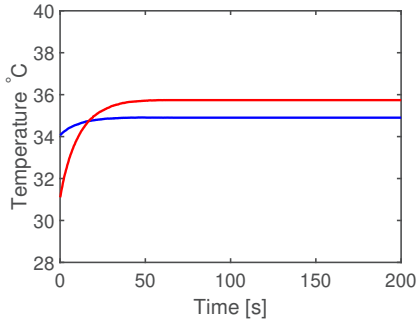

(d) Temperature time-course of the two measurement sets show a qualitative difference in the thermal history shape.

Figure 5.9: Comparison between microwave exposed sample (20Ghz 23 dBm, red) and ambient temperature control (34.9°C, blue).

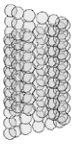

5.5.1 Design of better control experiments

In order to investigate the consequences of the samples thermal history we designed two alternative means of delivering a thermal gradient similarly inhomogeneous to that of microwave heating. One design consisted of simply flowing hot air onto the capillary. This design was realized by building an open air setup where the capillary was held next to a focused air flow (fig. 5.10). The other method was to direct light from an IR laser at an oblique angle at the sample (fig. 5.4). The thermal profiles of the different heating modes were not exactly the same, but all were spatially localized as compared to ambient heating of the box (fig. 5.11). Panel **d** of figures 5.12 and 5.13 show that the thermal history of samples exposed to these heating methods were qualitatively comparable to that of the microwave exposed sample.

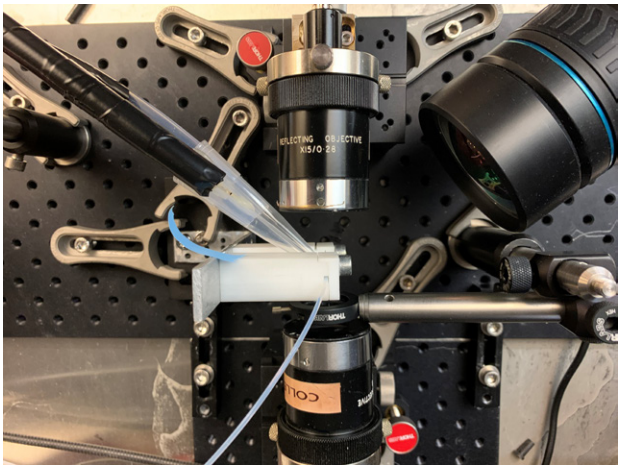

Figure 5.10: Open air setup for heat flow induced inhomogeneous thermal gradient.

The extracted parameter value *b* of these two methods were similar to that of the high power microwave exposed samples, see table 5.1. Statistical analysis against the original control sample of homogeneous heating to 34.9°C show significant differences both for t_{10} and the *b* values. However this difference in t_{10} could be eliminated by time-stretching. Statistical analysis of the new control sets against the microwaved samples does not show a significant difference for the high power microwave samples and the difference in t_{10} is similarly eliminated by time-stretching. Graphical comparisons between the 20GHz 23 dBm set and the two control sets with localized heating are shown in figures 5.12 and 5.13.

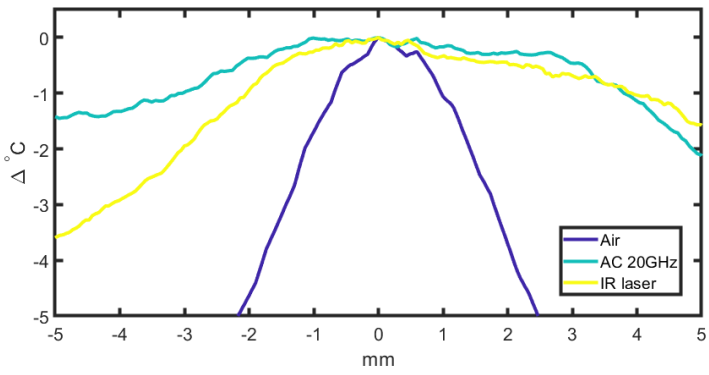

Figure 5.11: Temperature profiles of different methods of heating the sample: Airflow, IR laser and 20GHz 23 dBm electric field.

A comparison between the difference in temperature during the measurements and the theoretical non-linear time-stretch needed to complete overlap two curves is shown in figure 5.14. Panel 5.14a shows the polymerization curves, panel 5.14b the thermal history and panel 5.14c plots a calculated non-linear time stretch that would completely match the two curves along with the temperature history. The two curves have a similar shape and a Pearson correlation score of 0.98. Similarly high Pearson correlation scores are achieved when comparing sets of data with significantly different temperature history.

5.6 Discussion

There are still many outstanding questions with regards to how microtubules nucleate and grow in vitro, without the chaperoning of specialized MAPs and mediated by anchoring MTOC sites and specific tubulin isotypes. Model building of the kinetics is ongoing, see section 3.2.1. The stochastic nature of nucleation however, indicates that small perturbations might have an influence on the kinetics. Microtubules are polar species and align and migrate readily in alternating and static electromagnetic fields, see section 3.1.5.

Microtubule growth assays involve a temperature quench, and it is impossible to avoid a transient temperature change during the initiation of the experiment. The use of microwaves which heat water further complicated the matter, and the initially devised control experiments were found to be insufficient. Fortunately our careful thermal measurements of the sample enabled us to identify

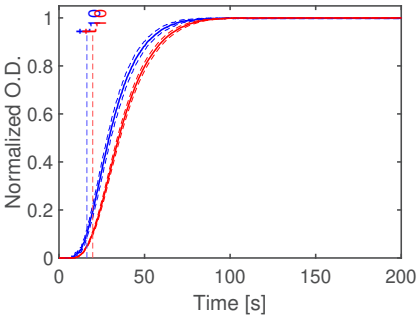

(a) Average normalized polymerization curves, standard error marked with dashed lines and t_{10} indicated

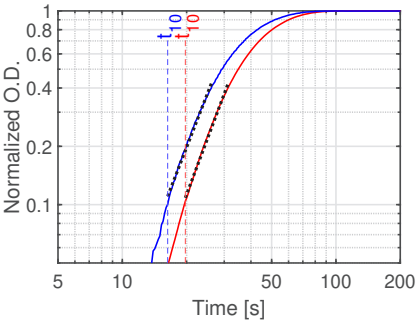

(b) Average normalized polymerization curves log-log plot shows the curves are parallel. Dashed line shows fit to determine *b* value, t_{10} indicated

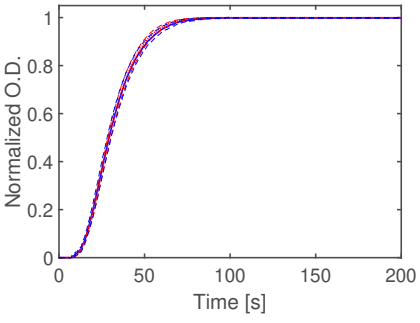

(c) Time-stretched of micro-wave exposed sample match the shape of the air heated sample.

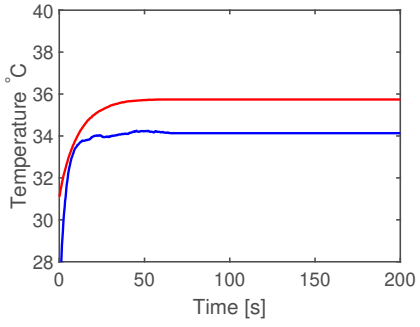

(d) Temperature time-course of the two measurement sets show a qualitative similarity in the thermal history shape.

Figure 5.12: Comparison between ambient 20GHz 23 dBm (red) and inhomogeneous heating by air flow (blue).

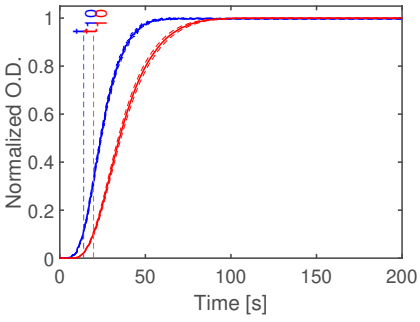

(a) Average normalized polymerization curves, standard error marked with dashed lines and t_{10} indicated

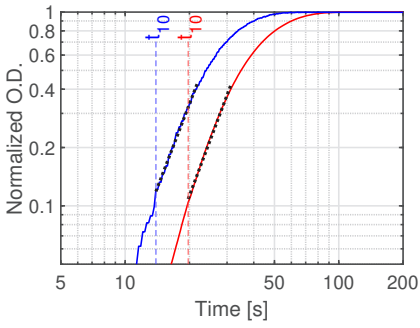

(b) Average normalized polymerization curves log-log plot shows the curves are parallel. Dashed line shows fit to determine *b* value, t_{10} indicated

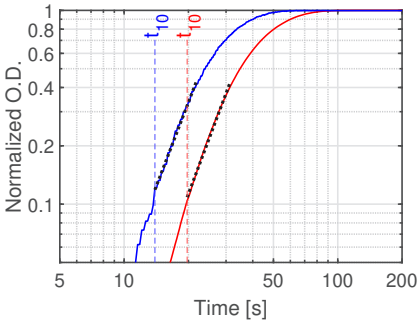

(c) Time-stretched of micro-wave exposed sample match the shape of the IR laser heated sample.

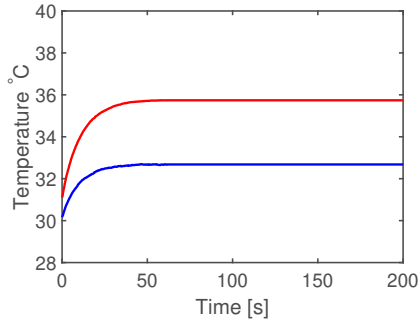

(d) Temperature time-course of the two measurement sets show a qualitative similarity in the thermal history shape.

Figure 5.13: Comparison between ambient 20GHz 23 dBm (red) and inhomogeneous heating by an IR laser (blue). **A**) Average polymerization curves. **B**) log-log plot of the same data show that the dashed lines are parallel. **C**) Time-stretched of micro-wave exposed sample match the shape of the IR laser heated sample. **D**) Temperature time-course of the two measurement sets show a qualitative similarity in the thermal history shape.

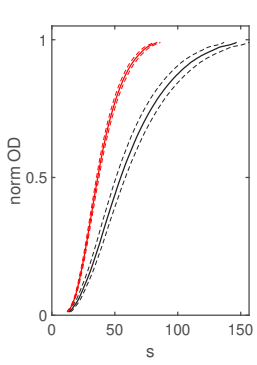

(a) Normalized polymerization curves. Standard error marked with dashed lines.

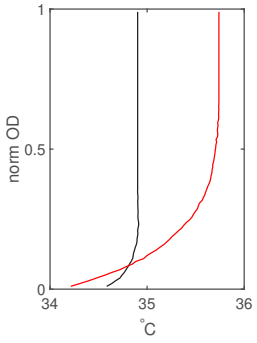

(b) Thermal history of both sample sets.

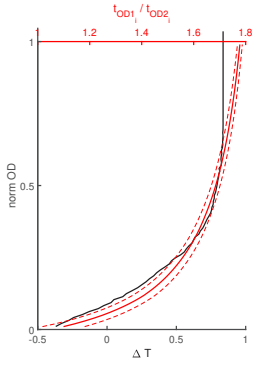

(c) Thermal history difference (black) and calculated time-stretch (red) co-plotted. Standard error marked with dashed lines.

Figure 5.14: Theoretical stretch calculations and comparison to thermal difference. Microwave (20GHz 23 dBm) exposed sample curves in red and 34.9°C ambient heating in black lines

the discrepancies in thermal history and design additional control measurement conditions that more accurately recreated the localized heating of microwaves.

Our results agree with a previous study which found no functional or structural changes in microtubules exposed to 2.5GHz electric fields [273].

The tubulin concentrations used for these measurements are well above the critical concentrations for spontaneous nucleation and slightly above what is usually used. The rationale for using this high a concentration is twofold, but both considerations were practical. One consideration is that when preparing for experiments using X-ray scattering, the highest possible concentration is usually preferred. At these concentrations, the microtubules polymerized well. Another consideration is that this high concentration substantially reduces the time needed for each repeat run.

An alternative explanation for the differences we saw between homogeneous and inhomogeneous heating could be thermophoresis (Ludwig-Soret effect), where larger particles are driven away from a hotter area. It could have been that this effect changed the microtubule concentration at the measurment spot. This effect have been utilized for aligning DNA in microchip analysis setups [274]. We tested this idea by designing a spatially localized inverse thermal gradient where the sample was hotter on each side of the measurement spot. However, this did not produce a noticeable difference in the polymerization kinetics.

Microtubule growth alignment can also be controlled by having a spatial gradient of the concentration of available tubulin dimers for growth. This has been experimentally implemented by letting tubulin nucleate in a thermal gradient. The nucleation step is faster in the warmer areas than the cold. After nucleation the polymerization reaction rapidly depletes the available dimer concentration in the warmer areas while the cold areas retain a higher dimer concentration. This enables preferential growth in the direction of higher dimer concentration [275]. The temperature gradient scale and spatial scale of this experiment is comparable to ours.

In summary, we are able to completely recover an apparent change in microtubule kinetics caused by the application of electromagnetic fields, by designing control measurements that mimicked the localized thermal effect of the microwaves. In the frequency range used in this study, 3.5-29GHz, no indication is found of a perturbation other than those than can be related to temperature alone.

Chapter 6

Microwave induced orientation perturbations of microtubules

PAPER III presents investigations into potential structural changes of microtubules when exposed to microwaves. The tubulin purification protocol, flowcell and signal generator used to generate the microwaves are the same as used in **PAPER II**.

This is a Time Resolved X-ray Solution Scattering (TR-XSS) study of potential structural changes in microtubules in response to a 20 GHz oscillating electric field. X-ray solution scattering is a technique that has been used to study microtubules over several decades [73, 164, 276]. Difference scattering is a powerful method to detect changes in protein structure [277, 278]. This experiment was conducted at the cSAXS beamline at the Swiss Light Source. The cSAXS beamline is an excellent beamline for this type of experiment since it has two complementary detectors, one SAXS and one WAXS which have an overlap in q and are housed in the same vacuum tube.

Preliminary and previous analysis had indicated a small low q difference signal between exposed and unexposed samples [268]. A slight elongation of the microtubules, possibly coming from a longitudinal standing wave, was one of several possible interpretations suggested by simplified modelling. However, the sign of this difference signal could flip depending on the choice of runs and outlier rejection criteria, which was worrisome. The difference signal also aligned well with the absolute microtubule scattering which would indicate an increase or decrease in microtubule mass, rather than a structural perturbation. We decided to investigate the influence of a horizontal or vertical alignment of our flow cell with

respect to the X-rays. These different capillary holder orientations also indicated flipping difference signals. Another problem we identified was that it was also difficult to return to the exact same position in the capillary after switching capillaries, which is occasionally necessary since the sample gets burned in on the capillary walls. This effect is compounded by the fact that all capillaries are somewhat unique with respect to the diameter and degree of tapering. Finally we decided to investigate how different capillary positions would influence the scattering. These measurements were all done using the same capillary and sample preparation and data collection protocols were kept short enough that a full set could be captured before the capillary suffered from precipitations. These investigations form the basis of **PAPER III**.

6.1 Experimental setup and procedure

Tubulin was purified as described in section 3.2.2. Microtubules were polymerized at a very high concentration, 47mg/ml, in order to increase signal to noise. This high concentration also helped to keep the microtubules from de-polymerizing in room temperature [190]. The sample was continuously replenished in order to avoid imaging radiation damaged proteins [279]. The sample was held in a thermostat at 37°C and sucked to the sample position through a thin tubing with a flow rate of 0.2 μl/s. The experimental setup in the beamline hutch is shown in figure 6.1. Figure 6.2 shows a closeup of how the capillary holder was positioned in relation to the X-ray tube and detector housing.

6.1.1 Exposure protocol design

X-ray scattering data were collected using an interleaved exposure strategy. The exposure protocol cycle we designed began with 4 s where the electric field was turned on, followed by 6 s where it was off. For technical reasons the off setting wasn't really off but the power was rather damped almost half a million times. Measuring the output of our signal generator set at 23 dBm we measured 20.1 dBm (0.1 W, 6.4 V_{pp}) really delivered to the waveguide. The "off" setting was measured to be at -35.87 dBm ($2.6{\cdot}10^{-7}$ W, 10 mV_{pp}). The off-time in the cycle was longer to account for the slower cool down period necessary since the microwaves heated the sample.

In the data analysis, these cycles were stacked on top of each other and averaged. Directed outlier rejection was not done, instead trimmed means were used where 20% of the data was excluded from the mean. The four different exposure protocols in total included 165 000 images recorded at 25Hz.

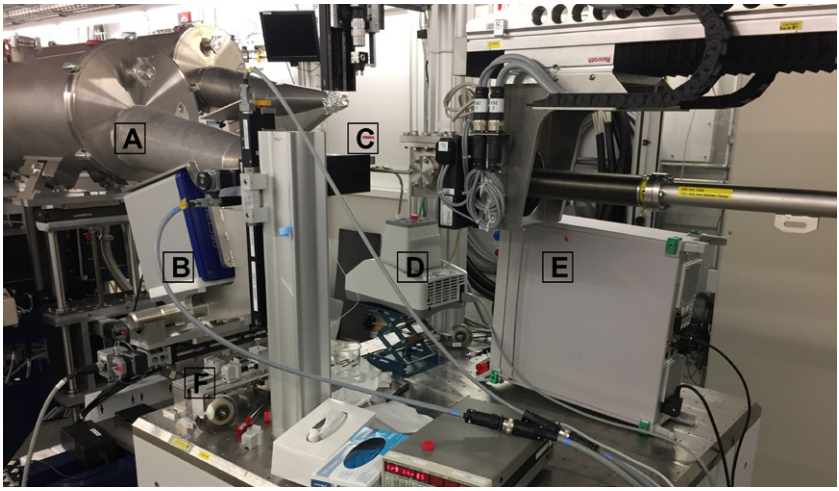

Figure 6.1: Experimental setup at cSAXS beamline, SLS. **A**) SAXS detector **B**) WAXS detector, **C**) Sample position, **D**) Thermostat, **E**) Signal generator, **F**) Sample pump.

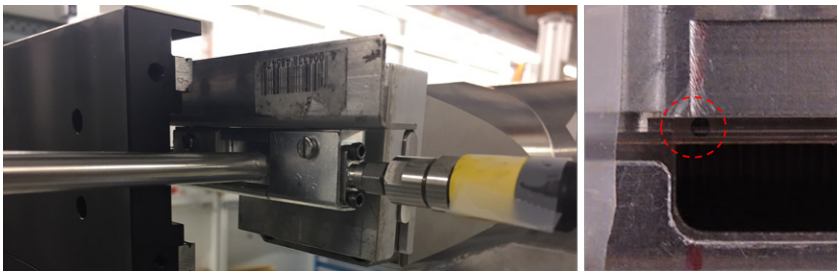

Figure 6.2: Experimental setup, closeup of sample holder. Left side shows sample holder in a horizontal orientation, Right side closeup shows capillary held between waveguide and ground, measurement area marked with red dashed lines.

6.1.2 Capillary positions

We investigated how a change in the beamspot position across the capillary influenced the diffraction pattern. The position closest to the waveguide, A, was set 15 μm before the scattering from the waveguide would interfere. The next position, B, was moved a further 50 μm away from the waveguide. The middle position, C, was a further 150 μm away. The farthest position was positioned another 150 μm away. Figure 6.3a and 6.3b shows the different positions we probed, both as a side-view and a cross-sectional view, as measured by a diode on the beamstop giving us a reading of the transmission through the sample environment. The capillary holder was itself aligned horizontally for these tests, since the beam spotsize was asymmetric with a shorter Full Width Half Maximum (FWHM) in the vertical axis. X-ray beamsize was 300μm in the vertical direction and 400μm in the horizontal direction. The absolute range was restricted since the outer edges had the beam either hit the copper waveguide or the steel ground which would interfere with the microtubule diffraction.

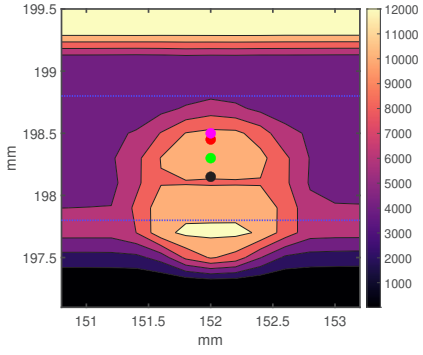

(a) The different positions in the capillary probed labelled as A, B, C and D. Black field shows area with no transmission of X-rays and a lighter shade means higher transmission.

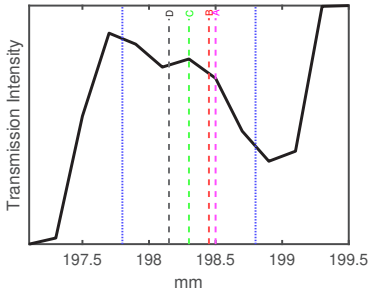

(b) Crossection across the capillary. The other side of the waveguide have an airgap where transmission is high. Capillary does not snug tightly to the ground so a smaller airgap through the hole in the dielectric can also be seen.

Figure 6.3: Capillary positions marked on a measurement of X-ray transmission across the capillary holder. Measurement resolution limited by the size of the beamspot, 0.3 mm vertically and 0.4 mm horizontally.

The absolute scattering of the different capillary positions show a marked difference in the background pedestal (fig. 6.4). Position C and D are the least affected by the background scattering, probably due to their larger distance to a heavy scatterer such as the waveguide. The ratios between the absolute scattering of the different positions does not change when the data is normalized which means that the probed volumes are comparable.

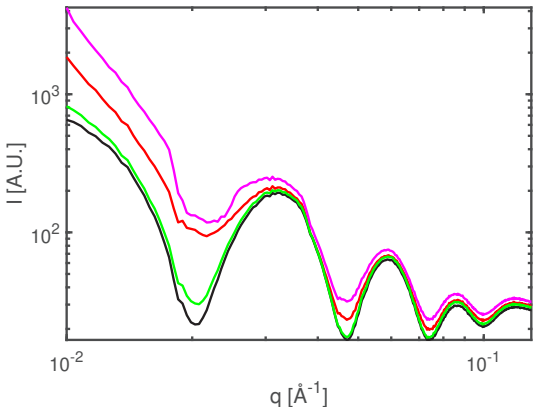

Figure 6.4: SAXS absolute scattering of the different capillary positions, A, B, C and D.

6.1.3 Microwave induced heating

It is a well known feature of microwaves, such as the 20GHz alternating electric fields we used, that they heat water. See section 2.1.4 for an introduction to this phenomenon. Any analysis of the data must take this effect into account. The solvent temperature of the sample can be seen in a broadening of the water peak at high q, since the average spacing between solvent molecules increase with higher temperature. We track this by looking at the data recorded by the complementary WAXS detector. With the last second of our off-period as baseline we can then calculate difference curves for every time-point up until then. SVD analysis can be used to separate different signals in a mixture by order of their relative importance [72, 90]. We extracted the basis spectra components of the WAXS differences and figure 6.5a shows the first basis spectra of the four capillary positions we probed. We can also plot the weight of this first basis spectra as a measure of its contribution to the complete curve for all time-points. The time evolution of the weights of this first basis spectra component is shown in figure 6.5b. The shape of the weight evolution is comparable to what we can track with an IR camera. The temperature difference basis spectra, as well as the weights they are assigned, are similar for all four capillary positions. This means that the thermal time-evolution was comparable and differences between the different capillary positions are not due to thermal inhomogeneities across the capillary.

The wide angle scattering data also allows us to normalize both the SAXS and WAXS together at the water peak isobestic point in a region around q=1.45Å^{-1}.

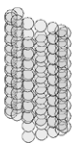

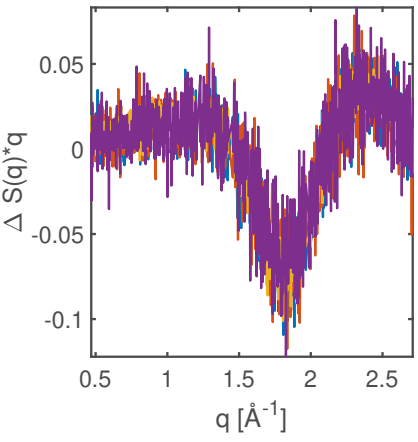

(a) SVD derived first basis spectra of water heating for the capillary positions overlap. This indicates that the temperature change is comparable.

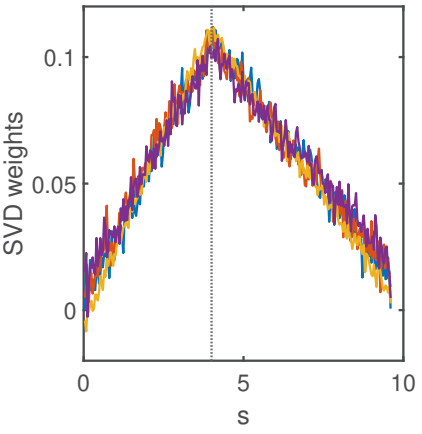

(b) Time evolution of the first basis spectra weights for the capillary positions overlap. Exposure protocol delimiter between ON and OFF marked with dashed line.

Figure 6.5: WAXS basis spectra and weights for the four capillary positions.

The isobestic point is the the scattering angle where the signal does not change with the temperature differences.

6.2 Flow-alignment and anisotropic scattering

The detectors record 2D images which are often azimuthally integrated to give a curve of scattering intensity *I(q)*. The peaks and troughs of the absolute scattering align well to a theoretically calculated scattering curve calculated using the online tool FOXS [280, 281] (fig. 6.6).

However, the 2D images recorded by the SAXS detector show that the diffraction pattern is not isotropically distributed which tells us that the microtubules are not randomly oriented (fig. 6.7). This is the result of flow alignment in the capillary which results in a diffraction pattern with an anisotropic distribution. With the sample holder oriented horizontally and the microtubules aligned approximately parallel to the flow, the scattering on the detector will be aligned vertically. Using terminology from fiber diffraction studies we call the dominant scattering direction for equatorial, and the perpendicular direction meridional. The flow alignment of microtubules was also seen in **PAPER I** where it was much more pronounced, due to the sample delivery via a GDVN microjet with a combination of higher flowrate and smaller diameter.

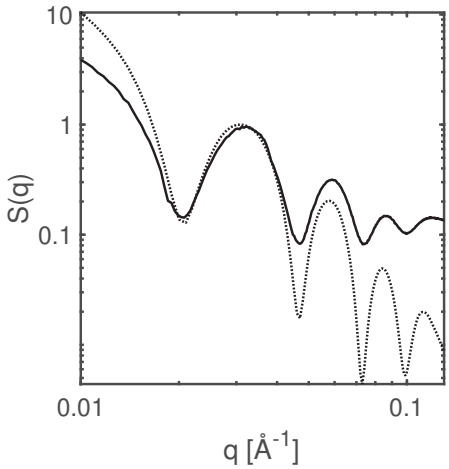

Figure 6.6: Experimental absolute scattering plotted with a solid line and theoretically calculated scattering with a dashed line. Theoretical scattering calculated scattering from a pdb structure using FOXS [280, 281].

Due to the flow aligment we decided to azimuthally integrate the equatorial and meridional scattering separately. Figure 6.7 also marks the partition into the equatorial and meridional quadrants used separately in the data analysis with yellow dashed lines. The alignment of the first diffraction maxima was determined for every image in the dataset and the division into equatorial and meridional quadrants was done in accordance. The anisotropic diffraction pattern also increased the sensitivity of the measured data with this alignment to detector panel gaps and the beamstop holder arm. In order to minimize this problem an inversion symmetry was imposed, the result of which is shown in panel 6.7b.

The theory of how anisotropic particles are aligned with flow have been known for a hundred years [260], although complicated geometric effects are still being discovered and investigated [282, 283]. Flow-alignment, or shear-alignment, has been used effectively to orient fibres for fiber diffraction experiments [284]. Indeed, several studies of flow alignment of high aspect ratio particles have been successfully conducted at the cSAXS beamline [283, 285]. Flow alignment is more pronounced in a low Reynolds number regime, where the ratio between inertial and viscous forces is small. The Reynolds number, *Re*, is a dimensionless number that can be calculated with equation 6.1, with u as the flow velocity, L

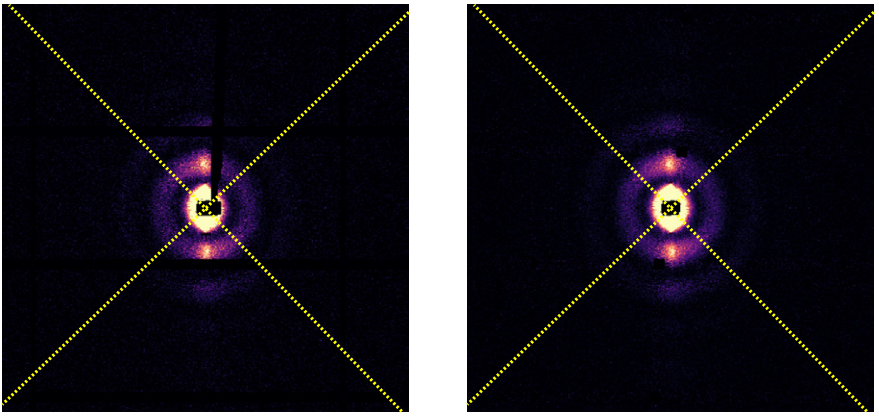

(a) Detector image from position C.

(b) Same image with inversion symmetry.

Figure 6.7: SAXS detector images with and without inversion symmetry. Yellow dashed lines mark the cutouts between equatorial in meridional and azimuthal integration sectors.

as a characteristic length scale and v as the kinematic viscosity [286].

$$Re = \frac{u \cdot L}{v} \tag{6.1}$$

With the capillary diameter taken as a characteristic length scale and the kinematic viscosity of pure water at room temperature being $\approx 9{\cdot}10^{-7}$ m^2/s, the calculated Reynolds number is $\approx 2{\cdot}10^{-7}$. When the Reynolds number is considerably smaller than 1, such as the case of our setup, viscous forces dominate over inertial forces and the flow can be assumed to be laminar. The actual viscosity of our sample is different to that of pure water, higher due to the glycerol content and the presence of microtubules and changing due to the temperature changes during a measurement cycle. Regardless of this uncertainty we can safely assume that the Reynolds number is very low.

The azimuthal distributions of the different capillary positions are shown in figure 6.8a. Separated azimuthal integrations for the equatorial and meridional quadrants of the detector image for capillary position C are shown in figure 6.8b. Both of these figures confirm what can be seen by looking at the 2D diffraction patterns.

The azimuthal distributions are different for the different capillary positions. A measure of this is the FWHM and these are reported in table 6.1. The middle

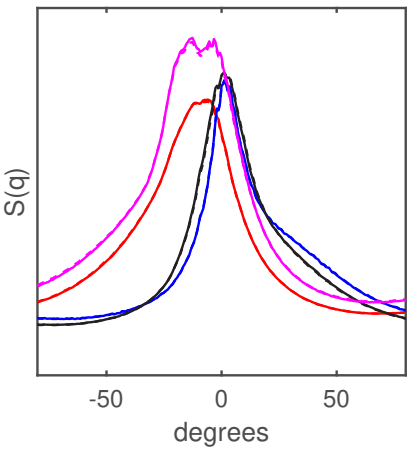

(a) Azimuthal distributions of different capillary positions **A**, **B**, **C** and **D** for the first microtubule maxima J_{01}. Solid lines show the ON part of the cycle and dashed lines the OFF.

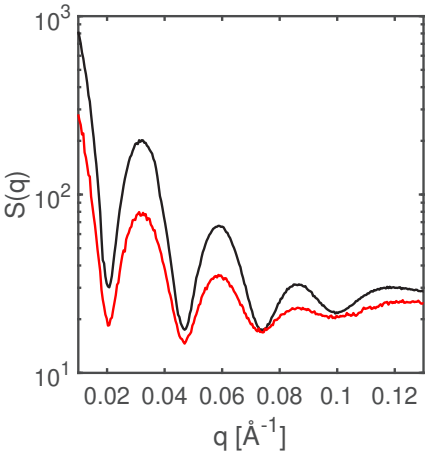

(b) Azimuthal integration of equatorial (black) and meridional (red) quadrants of capillary position C.

Figure 6.8: Anisotropic distribution of scattering

position with an estimated FWHM of ≈35 degrees was the most flow aligned and the positions closest to the waveguide were the least. This is in line with flow alignment theory.

Position	FWHM
A	52.9
B	52.4
C	34.6
D	39.3

Table 6.1: Azimuthal alignment FWHM (degrees) for the different positions in the capillary for peak J_{01}

It is worth to note that the scattering path through the capillary is not equal for physically vertical and horizontal scattering. Since the capillary is curved on the vertical axis where we have the equatorial scattering and flat in the horizontal direction where we have the meridional scattering, the meridional scattering have a longer beampath through the sample. This would act to dampen the scattered intensity in this direction. Our estimates of the difference in pathlength at the relevant scattering angles is that it is about 0.05%.

6.2.1 Modelling of anisotropy

In order to be able to relate the anisotropic distribution to the degree of flow alignment in the capillary a model of this was calculated using MATLAB [204]. A model of a microtubule was built up by isotropic spheres in place of tubulin monomers and rotated around its longitudinal axis in order to represent an average of many. This rotated fiber model was then again rotated, $\pm$ 60 degrees in different orientations perpendicular to its axis. In order to recreate a physically reasonable distribution of the rotation angles a Gaussian distribution was assumed (fig. 6.9). The theoretical scattering was calculated from density projection images of a range of such Gaussian distributions. An example of such a density projection is shown in figure 6.10. The theoretical scattering was calculated by a Fourier transform of the density projections. Examples of two such patterns are shown in figure 6.11.

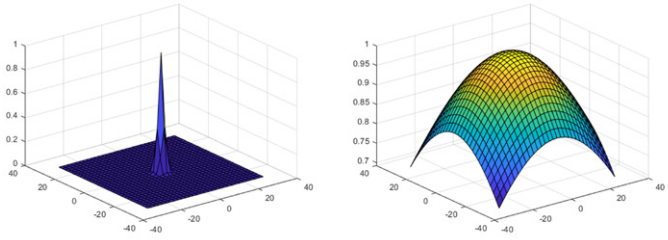

Figure 6.9: Gaussian distributions as a model of flow aligned rotational distribution. Examples of two such Gaussians, with a narrow and wide angular distribution. X and Y axis have the unit degrees.

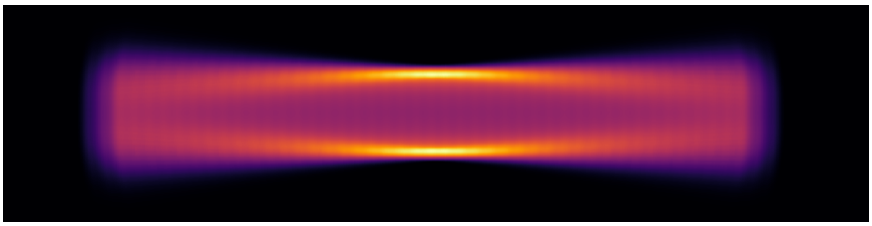

Figure 6.10: Microtubule density projection of rotated models with a Gaussian distribution with a sigma of 5 degrees.

Figure 6.12 shows the relationship between the FWHM of the calculated scattering and the projections angular distribution. Assuming a Gaussian distribution of the scattering the ratio between FWHM and sigma is 2.355. The approximately linear relationship between the two tells us that what we can relate the different

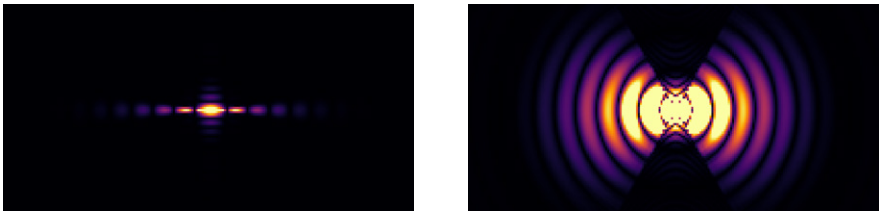

Figure 6.11: Fourier transforms of rotated fiber models. Panels shows the transforms of a projection with a Gaussian distribution of rotation angles. Left) Gaussian sigma of 5 degrees. Right) Gaussian sigma of 45 degrees

azimuthal distributions of the experimental scattering data to the angular spread of the alignment.

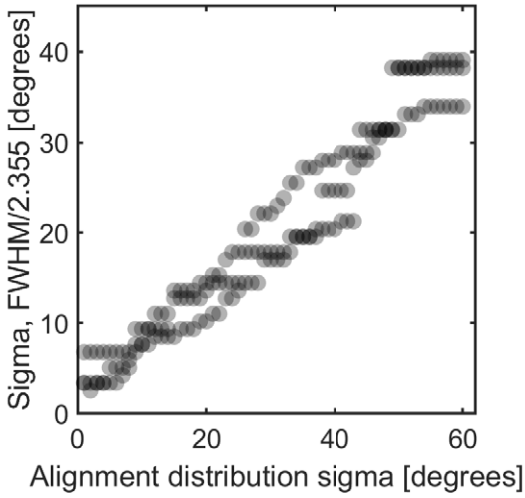

Figure 6.12: FWHM of equatorial peaks in transform of rotationally distributed fiber models vs the sigma of the angular distribution.

6.3 Results and discussion

SAXS difference scattering curves for the different capillary positions was calculated by subtracting the average data from when the microwaves were turned off from the exposed part of the cycle, $\Delta I)(q) = I(q)_{ON} - I(q)_{OFF}$. The resulting X-ray scattering difference curves from azimuthal integrations of quadrants

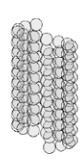

separating the equatorial and meridional scattering are shown in figure 6.13. Common for all difference curves is that the peaks and valleys align with the absolute scattering of microtubules. For position A and B, the positions closest to the waveguide, the difference curves show an increase in the equatorial scattering and a corresponding decrease in the meridional scattering, although to different extents. The data collected from the middle of the capillary, position C, is different and shows an increase in both equatorial and meridional scattering. Position D, farthest from the waveguide show no change in the equatorial quadrants but a decrease in the meridional quadrant.

The opposite sign but similar magnitude of the difference scattering for positions A and B indicate a microwave induced increase in the already preferential alignment axis of the microtubules the closer we are to the waveguide. The field experienced by microtubules farther away from the waveguide can be expected to be lower due to dielectric shielding effects. It is important to note that the differences for positions A are considerably larger than those of the other positions and that due to the overlap of the positional sampling due to the width of the X-ray beam the differences of position A would bleed over into other positions. The position C differences could be said to indicate an apparent increase in tubulin mass since both quadrants have a positive difference scattering.

6.3.1 TR-XSS

In order to understand the temporal evolution of these differences we calculated time-resolved difference signals as compared to a reference point consisting of the last 400 ms of the off period. We used SVD analysis to extract the basis spectras and time evolution of the weights in the same manner as extracted the WAXS heating signal. For this analysis we focused on the q-range with the most interesting features, $0.01 < q < 0.1$.

The first basis spectras for the equatorial and meridional detector quadrants and the time-evolution of the respectively assigned weights for position C are shown in figure 6.14. The two main basis spectra for the equatorial and meridional quadrants have a Pearson correlation of 0.98. Their shape similarly indicates an increased alignment with the already preferred direction of the flow-alignment, in that they signify an increase in equatorial scattering and a corresponding decrease in meridional scattering. However, the time evolution of the basis spectra weights show that this *alignment effect* actually decreases when the microwaves are turned on. The difference signal weights decrease during the first part of the exposure cycle when the sample is exposed to microwaves and declines slowly. The alignment happens during the off phase of the exposure cycle, but with a time-delay of ≈ 1 s. A delay in the time-evolution of the signal is to be expected

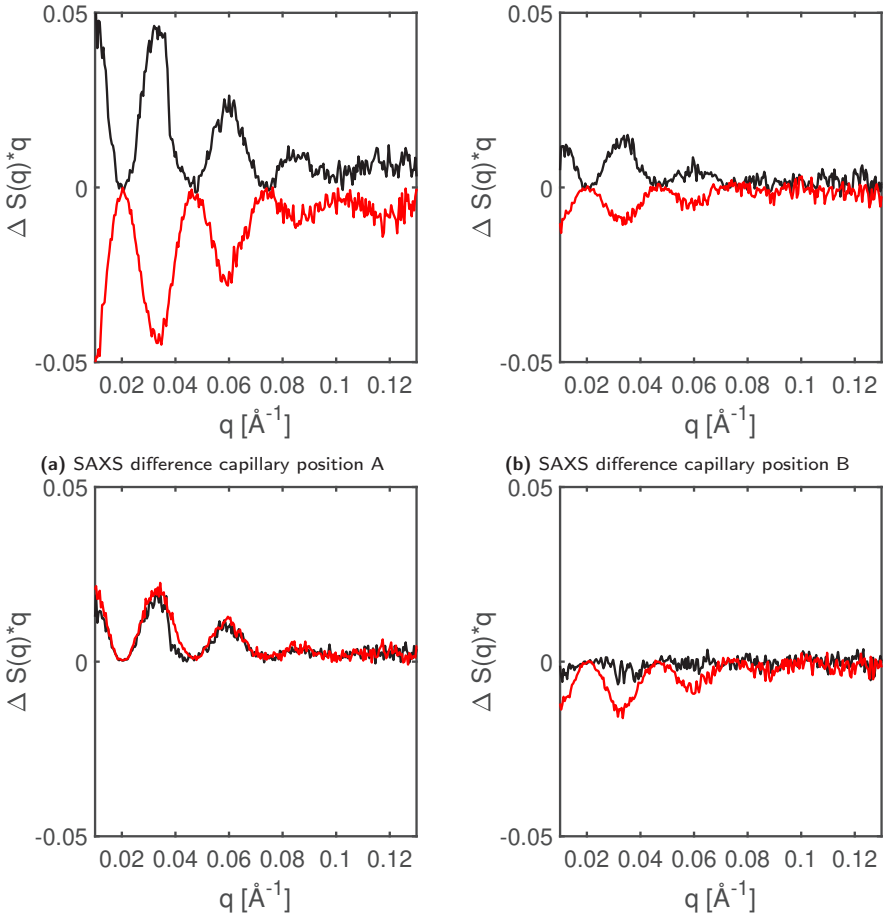

(a) SAXS difference capillary position A

(b) SAXS difference capillary position B

(c) SAXS difference capillary position C

(d) SAXS difference capillary position D

Figure 6.13: SAXS differences of the different capillary positions. Equatorial scattering in black lines and meridional scattering in red lines.

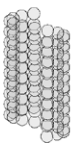

due to the flow velocity of 250 μm/s and the microwave field extending in a region around the measurement spot in the capillary Because of fluctuations in the decline and rise of the weights the average difference curve as seen in 6.13c show an increase in both the equatorial and meridional scattering, which is opposite to the effects the time-resolved analysis shows.

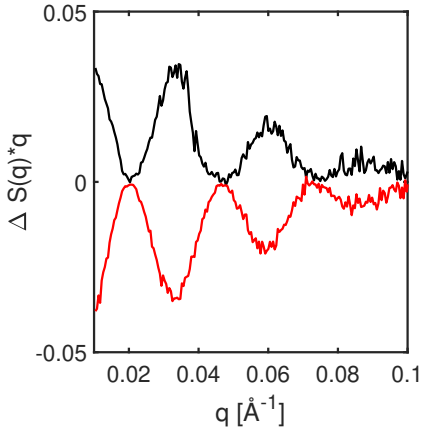

(a) Basis spectra of difference signal for equatorial and meridional scattering.

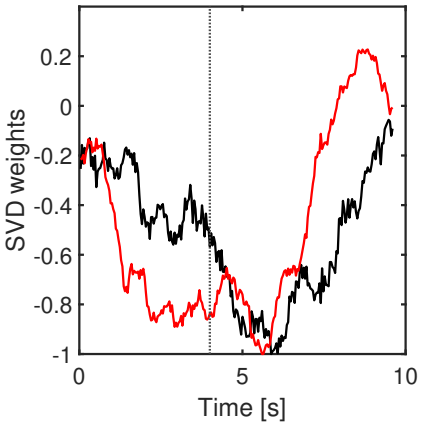

(b) Time evolution of the basis spectra weights. Cycle change switch marked with a dashed line.

Figure 6.14: SAXS basis spectra and weights for position C. Equatorial in black and meridional in red

The time evolution of the basis spectra weights for position A shows this tendency in a consistent way. The equatorial and meridional differences show a coordinated time-evolution during the exposure cycle (fig. 6.15). This pattern could also be seen in equatorial differences for position B while the time-evolution of the weights for the meridional differences was too noisy to detect a meaningful trend. The basis spectra of position D is comparable to those of the other positions, but the time-evolution was also too noisy to yield any meaningful interpretation.

Taken together this analysis suggests that position A and C show the same basic time-evolution of the difference signal, a decrease in sample equatorial alignment during microwave exposure. The main difference between them is the longer time-delay of position A before the alignment resumes its restoration. This difference can be explain by the slower flow velocities near the capillary edge which increases the time it takes to replenish the sample.

Our analysis suggests an alignment effect by the applied electromagnetic fields along the electromagnetic fields lines, perpendicular to the flow alignment. This

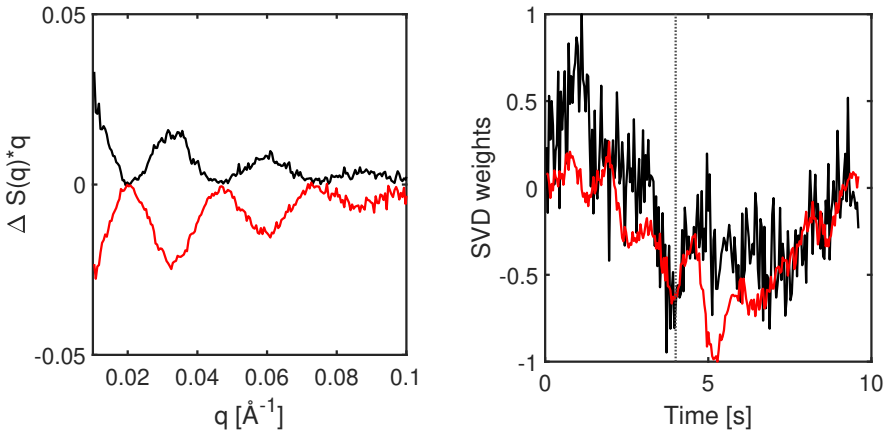

(a) Basis spectra of difference signal for equatorial and meridional scattering.

(b) Time evolution of the basis spectra weights. Cycle change switch marked with a dashed line.

Figure 6.15: SAXS basis spectra and weights for position A. Equatorial in black and meridional in red

is in line with previously published studies [177–181, 287]. A study with considerably higher field strengths at lower frequencies estimated the time to align a microtubule to the field was 1 s which aligns with the time-frame for the growth and decay of the difference signal we see [178]. Our results indicate that the dielectric properties of microtubules have a measurable effect on the alignment at the frequency and voltage applied in this experiment.

Changes in alignment and azimuthal distribution also changes how much of the data is lost between detector panels and beamstop holder which makes conventional full frame azimuthal integration insufficient. Any measurable structural perturbation must be large enough to overcome these effects. We have found no persistent indications of a structural change in the microtubule structure and we believe that a combination of the above mentioned effects was the cause of the intermittently switching difference scattering previously seen.

In summary, **PAPER III** investigated the possible structural perturbations of microtubules by an alternating electromagnetic field and found that microwaves induced microtubule alignment perpendicular to the flow alignment already in the capillary. The effect is compounded with differences in flow velocity and flow alignment in different parts of the capillary. Without a time-resolved analysis of the azimuthal redistribution of the diffraction the conclusions could have been different.

Chapter 7

Summary and Outlook

7.1 Summary

The common theme of this thesis have been investigations into microtubule structure and function. **PAPER I** was a methods development study indicating the possibilities of structure determinations on single particles. The study achieved an intermediate resolution compared to conventional methods, but signified a significant increase in resolution compared to previous single particle imaging attempts. **PAPER II** investigated the possible perturbances caused by electromagnetic fields on microtubule function. The results show that an apparent perturbation could be related to subtle temperature effects. Similarly, **PAPER III** investigated possible structural perturbations caused by microwaves, and found that the only detectable perturbations were on the microtubule alignment, an effect is biophysical rather than structural.

7.2 Comments on research on biology and electromagnetic fields

Exposure protocols using electromagnetic radiation in the microwave range will heat the sample which necessitates the introduction of proper control measurements. On the other hand, potential non-thermal effects might be smaller than the thermal effect and would then be obscured. A way to perform these kinds of experiments would be to use power levels too low to induce a noticeable temperature difference. However, biophysical considerations say that the applied power needs to be larger than the thermal energy kT in order to induce an effect that wouldn't drown in the thermal noise [271, 288]. These two approaches seems to be in contraction.

A set of publications [289–291] covering measurements on the influence of microwaves on a heat-shock reporter gene in *C. Elegans* were later retracted [292] when a small 0.2°C difference in temperature was observed between the exposed and the control group. When properly accounted for this removed the previously reported effects. This retraction did not, however, stop other researchers from citing the articles as examples of effects of microwave radiation [293]. A critical review of microwave assisted enzyme protocols [294] shows that the lack of calibrated standards for the exposure apparatuses used calls the interpretations of the results into question.

It is my view that it is still unknown if the man-made electromagnetic fields that we are surrounding ourselves with have a harmful effect, or non-thermal effects. It is of course impossible to prove a negative, that there is no immediate or long term effects. Unfortunately the research into this question is lacking in reproducibility. Decades of speculations can be found in the scientific litterature that are very intriguing but have provided very little experimental validation. The most important lesson learned is that it is very important to design proper controls.

7.3 Late additions

Due to delays caused by the pandemic a couple of related experiment that were planned to be a part of this thesis only came to fruition during the last year. The analysis of the experiments described below is not finalized as this thesis is written. But since they have constituted such a large part of my research education I wanted to introduce them in my thesis. The experiments and their current status are described below.

7.3.1 Single particle imaging of microtubules at the European X-FEL

In an attempt to follow up **PAPER I** by performing coherent diffractive imaging on single microtubules instead of bunches of microtubules we performed a repeat experiment at the European XFEL in Hamburg. The European XFEL has a substantially increased repetition rate and we hoped that this would allow us to collect a more substantial dataset. This was seen to be especially important since we also lowered the microtubule concentration in order collect data on single microtubules. This experiment was actually the first with users onsite since the pandemic related restrictions were imposed.

Brief experimental description

Microtubules were purified as described previously, see section 3.2.2. Microtubules were polymerized at a concentration of 5 mg/ml with 5% glycerol, 1 mM GTP, for 20 min at 37°C. The polymerized microtubules were then diluted to 2 mg/ml and stabilized for room temperature operation with a pre-heated buffer supplemented with Taxol (paclitaxel). Microtubule polymerization and lengths were checked onsite by electron microscopy (fig. 3.11) [295]. The sample was jetted in front of the beam focus using a GVDN with a diameter of ≈5 μm and flow speed of ≈ 40 ms^{-1}.

The beam focus had a FWHM of 200 nm and the X-ray energy was 9,3 keV with energy of each X-ray pulse of ≈ 400 μJ. The X-ray pulses are not evenly spaced in time at the EU-XFEL but come in pulse-trains with an internally high repetition rate of 1.1 MHz [296]. The detector distance was 0.7 m.

Unfortunately the high repetition rate meant that the liquid jet did not have time to stabilize after each X-ray pulse induced explosion (fig. 7.1). Our previous experience with the dataset collected using a GVDN at LCLS with a X-ray pulse repetition rate of 120Hz led us to expect a similar flow alignment of the fibrils. However, the pulse-structure of the EU-XFEL, while allowing us to collect immensely more data, also changed the nature of the sample delivery. We saw that, instead of imaging microtubules flow aligned in a liquid jet we saw scattering from microtubules preferentially aligned in other directions. A example of a single microtubule hit is shown in figure 7.2. We imaged microtubules in a disintegrating and deflecting liquid jet. The X-ray pulses that hit a sample liquid cause an explosion and a shockwave that influences the liquid around it [297]. At slower repetition rates the liquid jet, moving at tens of meters per second, have time to recover. A recent paper have reported that at high repetition rates this shockwave could also influences the structure of proteins in crystals upstream from the beamspot [298].

Data reduction and processing

In total, 143 million useful images were collected in a dataset of approximately 2 petabyte. In order to find the relevant images for processing a Machine Learning (ML) model was trained with 6000 manually selected images representing different categories (microtubule hit, jet streak, no hit). The ML approach only worked partially and had to be complemented by a sorting based on azimuthally integrated diffraction patterns and heuristically developed criteria for peak positions and distances and signal strength. This left us with approximately ten thousand images. Azimuthal integration show that we have fairly broad positions ranges for the first six peaks in the equatorial layer line (fig. 7.3).

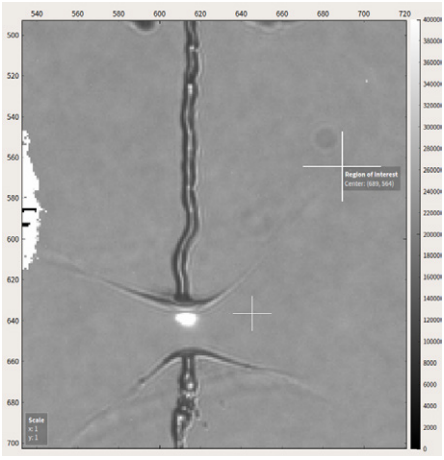

Figure 7.1: Image of liquid jet explosion after X-ray pulse hit.

Images of a chosen subset based on the 2nd and 3rd peak were aligned and merged to reduce noise. However, no higher order layer lines emerged, which we had expected from our previous experience with coherent diffractive imaging of microtubules [299]. The phase retrieval algorithm previously deployed was adapted for this dataset, but the projection that emerged were not on par with our expectations (fig. 7.4).

Further work

In order to understand our failure to recover the higher order layer lines even after averaging $\approx$ 5 000 images, we simulated diffraction patterns from single microtubules by way of a helical tube built from isotropic spheres. At the resolution we are working such a crude model would suffice. The real space rotations and simulated diffraction for a couple of rotations, both in plane and out of plane, are supplied in figure 7.5 and 7.6. Preliminary simulated diffraction patterns created using SKOPI were used when deciding on the detector panel geometry and distance before the experiment [300].

Azimuthal integrations of the simulated diffraction patterns of differently aligned fibers were done in order to understand how the orientation influences the layer line peaks (fig. 7.7). These curves shows that the first three strong equatorial layer line peaks have unchanged positions. This makes sense since their information content concerns the general size of the imaged fiber (outer and inner diameter). However, the relative intensities and positions of the higher order

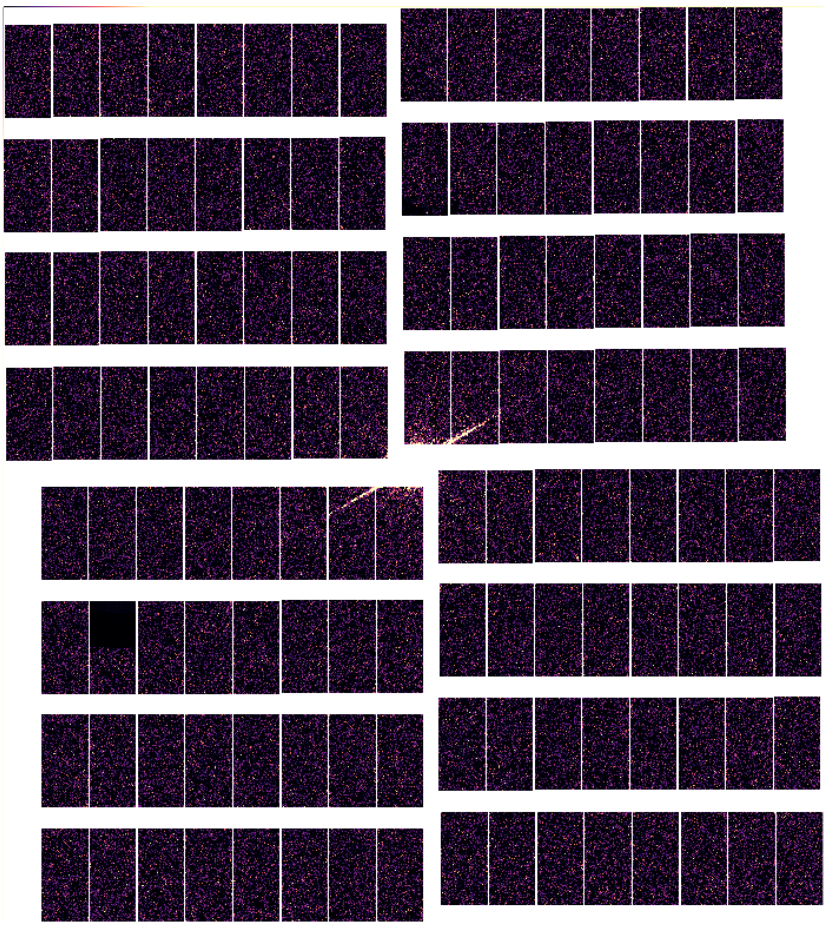

Figure 7.2: Example of a microtubule imaged at the EU-XFEL.

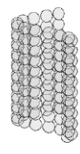

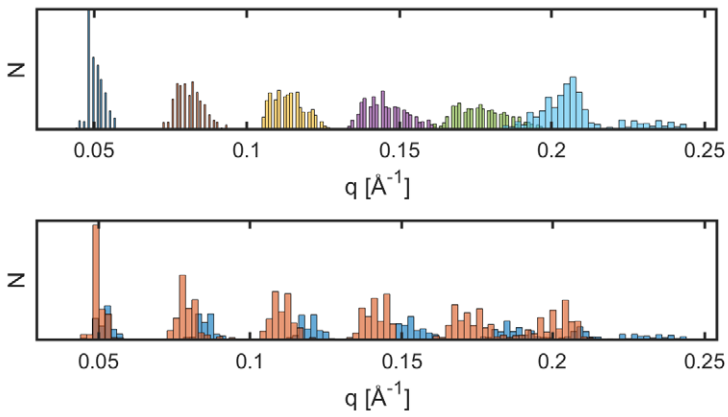

Figure 7.3: Histogram over the range of the first peaks in the equatorial layer line. Lower subplot shows examples of two subpopulations

peaks/layer lines differ substantially with the orientation of the simulated fiber. This guided our further attempts to properly sort and merge the different subsets.

We are currently working with the assumption that we can use the distributions of the higher order peaks (fig. 7.3), to sort images based on different orientations. Initial analysis suggests that position distributions for all well resolved equatorial line peaks are correlated and could be used to select further subsets of the data (fig. 7.8). The 1st is peak not well sampled on the detector and is not correlated with the other peak positions which indicate that the determined peak position is unreliable, especially since the peak intensity correlates with the neighbouring peaks. Correlation is higher between between the 2nd and 3rd peaks which is reasonable since they would represent different microtubule species with different number of protofilaments. The peak positions and intensities are not correlated with each other.

While this spreading of the sample into a larger volume decreases the hit rate it also allowed us to image microtubules from a variety of angles which could potentially enable us to reconstruct a 3D projection. Due to the different orientations of microtubules imaged in the dataset, what we ended up with was more closer to an ideal single particle imaging dataset than what we were prepared for. We are currently exploring if the dataset we collected will be enough to reconstruct such a structure.

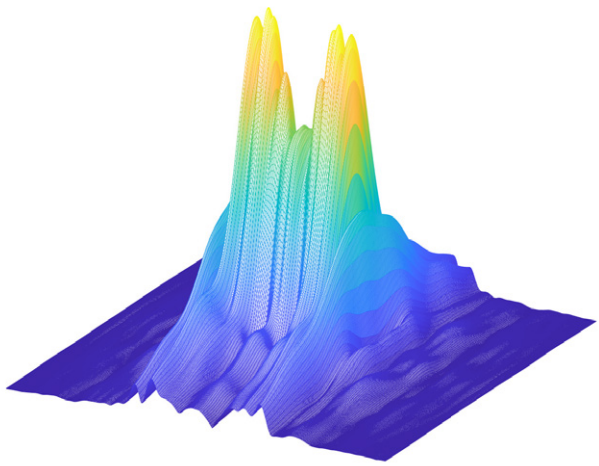

Figure 7.4: Reconstructed real space 2D density projection of a microtubule.

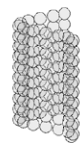

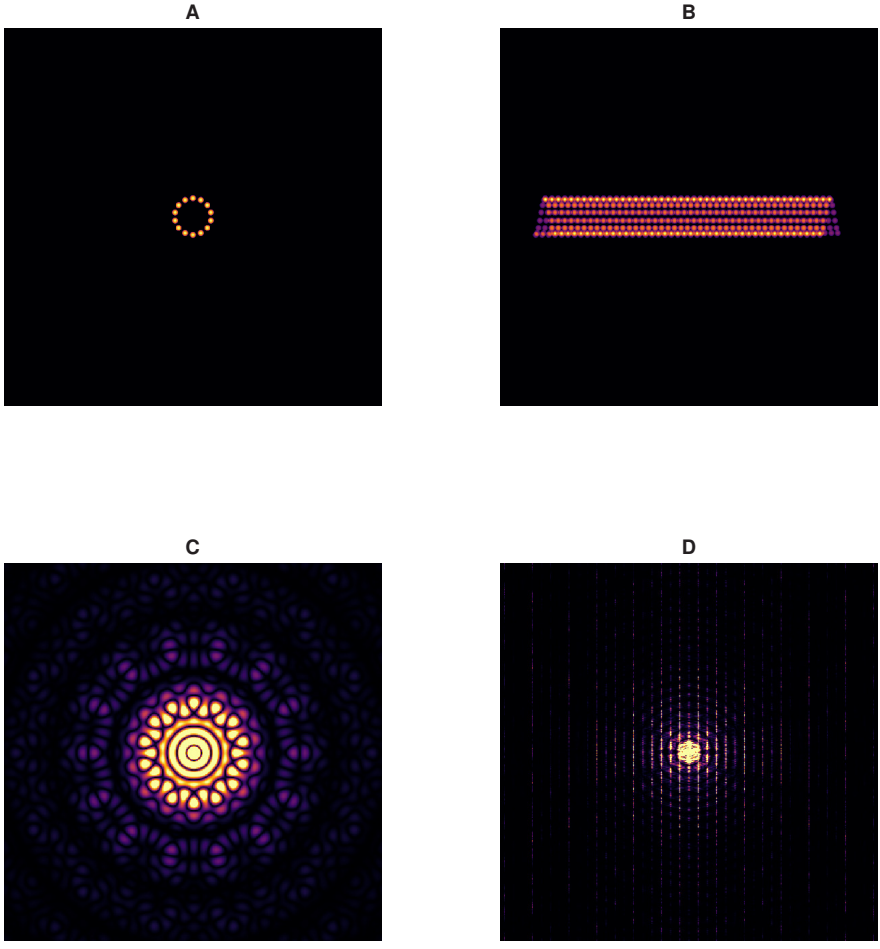

Figure 7.5: Helical sphere model and simulated scattering from right angles. Density projection of model fiber oriented into the plane (**A**) and perpendicular to it's axis (**B**). **C**) Simulated scattering of A. **D**) Simulated scattering of B

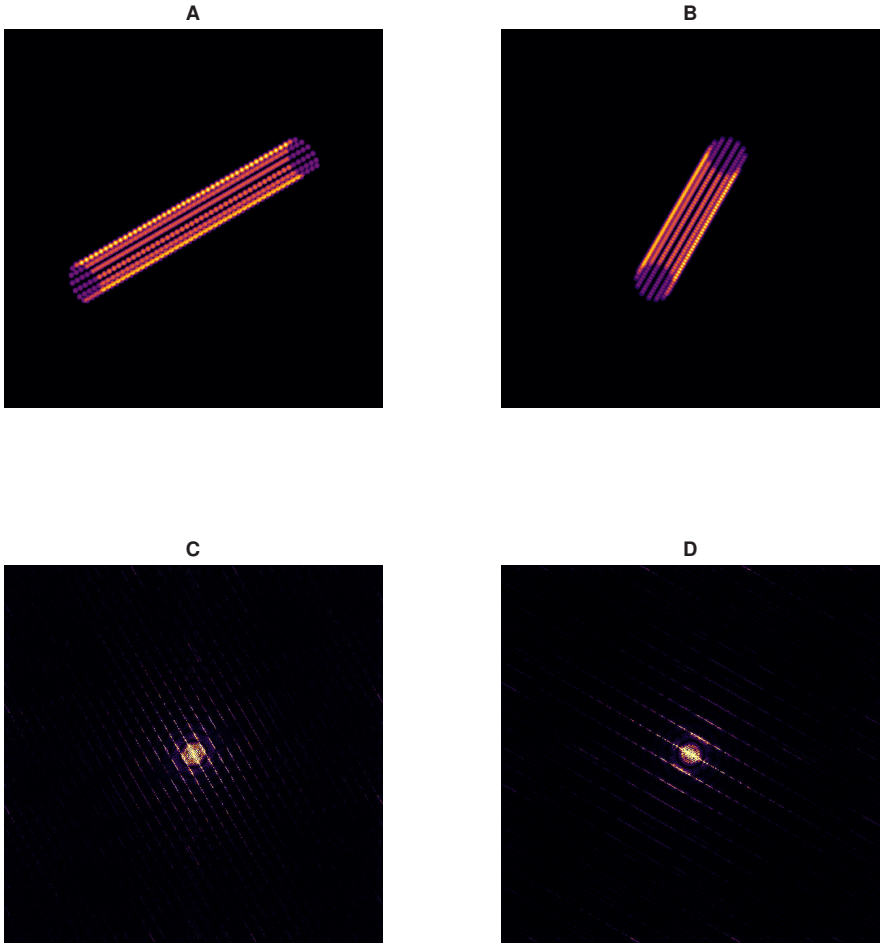

Figure 7.6: Helical sphere model and simulated scattering from simultaneous increases in rotation both into the plane and on the plane. **A**) Density projection of model fiber rotated 30 degrees into and onto the plane **B**) Density projection of model fiber oriented 60 degrees into and onto **C**) Simulated scattering of A. **D**) Simulated scattering of B

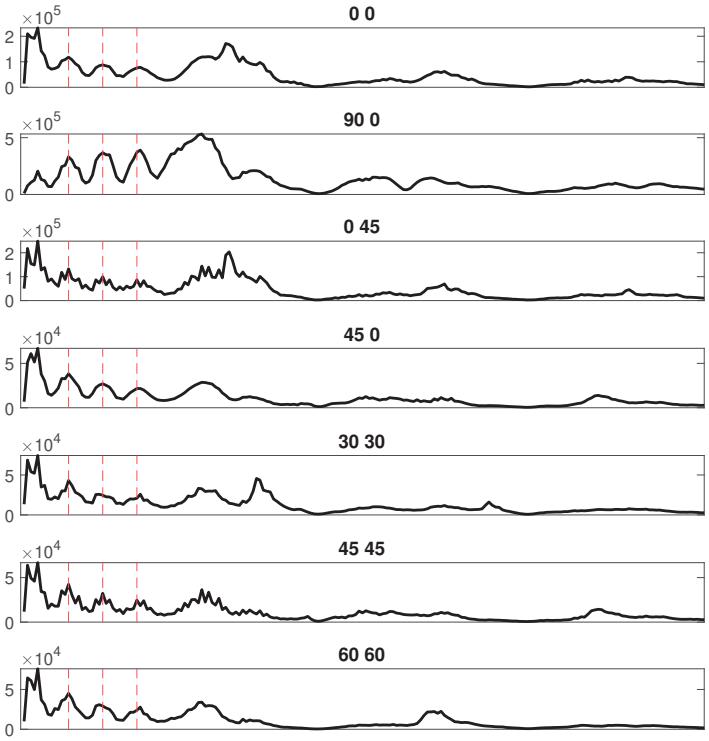

Figure 7.7: Azimuthal integrations of simulated scattering from a range of model rotations. Labels denoted for anglular rotations [into plane] [on plane]. The three first peaks positions are unchanged, while higher order peaks are rotationally dependent.

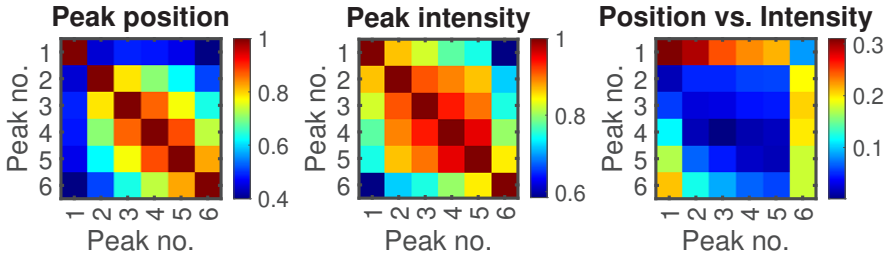

Figure 7.8: Heatmap of correlations between the first six equatorial layer line peak positions and intensities.

Methods for 3D phase retrieval reconstructions have been utilized in the previously mentioned single particle imaging studies on larger particles than microtubules. A step of noise-reduction on the diffraction images, similar to what was done in **PAPER I**, is important [255]. Other methods for sample delivery might also be preferable for future projects. The jet explosions forced our sample away from the X-ray beam rather than align it in front of it. One such method that enables a steady stream of randomly oriented samples is electrosprey [81, 301]. However, it is unclear if the droplet size is suitable for larger biomolecular fibres such as microtubules.

7.3.2 High voltage intermediate frequency electromagnetic fields influence microtubules polymerization kinetics

This is a study designed to deliver a considerably higher voltage than **PAPER II** but at frequencies that do not couple well with water and thus do not heat the sample. Preliminary results indicate that at set of four frequencies between 100 - 240 kHz induces a change in the shape of the bulk microtubule polymerization curve to various extents. The frequencies used in this study are comparable to those of the Tumor treating fields anti-cancer treatments, see section 3.3.3. Currently the mechanism of action of TTF is unknown [226]. This study might help elucidate TTFs potential influence on microtubule polymerization.

Experimental design considerations

A 3D-printed flowcell as well as a signal generator has been designed for the safe application of high voltage alternating electric fields. The final design models of the flow cell components are shown in figures 7.9a and 7.9b. The sample is kept in a 0.6 mm diameter quartz capillary and is sandwiched between a pair of copper spheres. The flowcell has inlets and stabilizers for fiberoptic cables connected to a UV source and microspectrophotometer for similar OD measurements to those done for **PAPER II**. The copper spheres are connected via Safe High Voltage (SHV) cables to a custom built signal generator capable of delivering up to 800V peak to peak in the kHz and MHz range.

Aliquots of previously purified tubulin, see section 3.2.2 for a detailed description of the purification protocols, were thawed on ice and prepared for polymerization in a similar way as for **PAPER II**. A syringe pumped sucked the sample from ice to the measurement point in the flow cell in 14 seconds. Pictures of the experimental setup are provided in figures 7.10 and 7.11. The flowcell was submerged in a bath of transformer oil, both in order to avoid electrical discharges and to control the temperature. The oil was heated using a thermostat and kept at 37°C. The sample thermal history was in this way kept identical for the different exposure protocols. The submerging of the flowcell holder in oil precluded us from measuring the temperature of the sample. But, with the holder out of the oil bath we could not detect any temperature change in a sample when exposed to the experimental frequencies using an IR camera.

Data analysis and results

Microtubule polymerization curves were measured for four frequencies, 100 kHz, 147 kHz, 193 kHz and 240 kHz as well as a control without any oscillating field. The order of the measurements was randomized using a coin toss and the

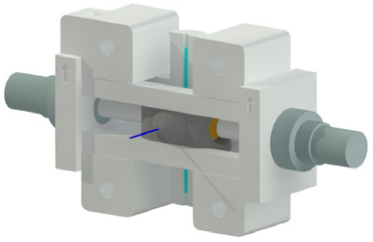

(a) Design model for high voltage flow cell. Connectors for SHV cables in gray

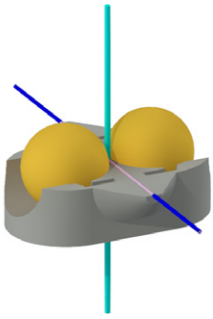

(b) Design model show placement of copper spheres inside flow cell. Quartz capillary in turquoise and fiber optics in blue

Figure 7.9: Design components of high voltage flow cell

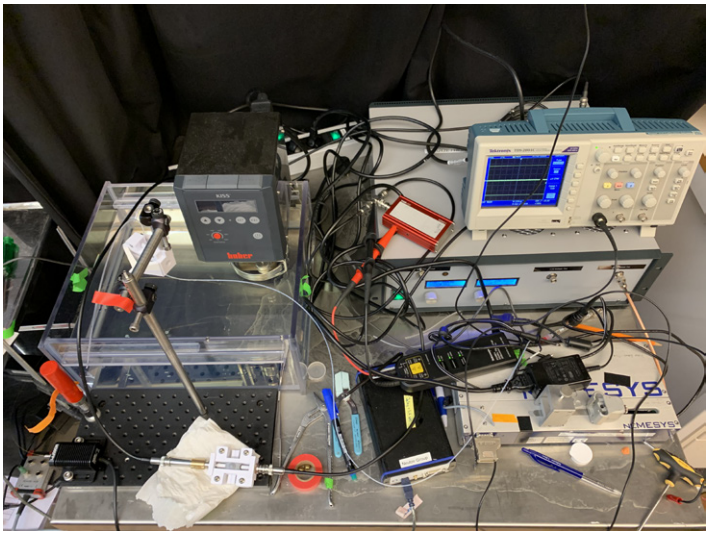

Figure 7.10: High voltage experimental setup overview

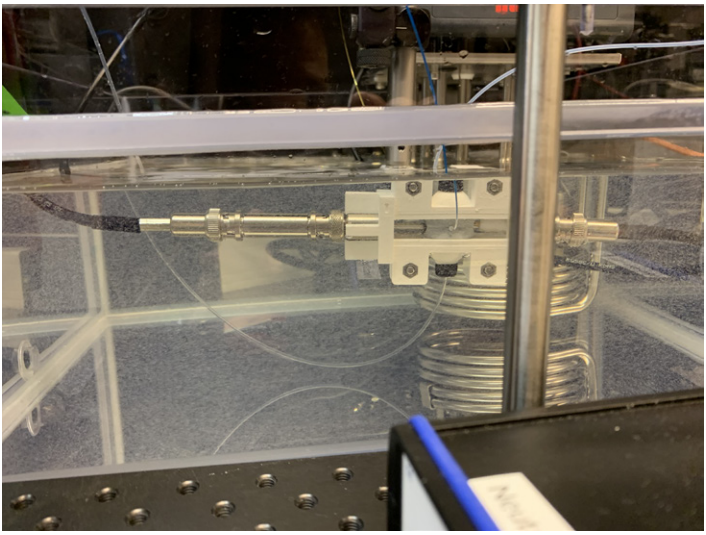

Figure 7.11: Closeup of high voltage flowcell in oil-bath.

average number of measurements for each exposure protocol was 34. A selection of parameters based on the curve shape was extracted, similar to the analysis of polymerization curves in **PAPER II**.

The average curves of the five sets is shown in figure 7.12, with inserts focusing on the difference between the curves at t_{80}, the time where the curves have reached 80% of the steady state OD. Curves were normalized and time-stretched to match t_{50} in order to focus the investigations on the shape of the curve.

The large sample to sample variation typical for microtubule polymerization necessitated the use of statistical methods to determine if the differences were significant. A two-component t-test was used to compare the different groups. Depending on the stringency of the p-value cutoff either the 147 kHZ or both 100 kHz and 147 kHz were significantly different compared to control with regards to b and t_{80}.

Complementary SAXS structural studies with the same high voltage flowcell and exposure parameters have also been performed. Figure 7.13 shows the experimental setup at the ultra-SAXS beamline ID02, ESRF. Ideally, if a functional response to electromagnetic fields could be associated with a structural perturbation, the understanding of the induced changes would be more complete. It is important to note that analysis of possible functional and structural perturbations is ongoing and the results reported here are preliminary. Either way, the

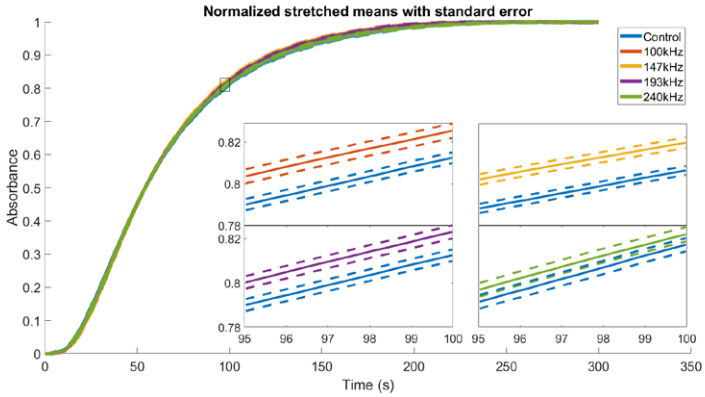

Figure 7.12: High voltage microtubule polymerization curves for a range of kHz frequencies together with the no-exposure control measurement. Average curves and selected comparisons with standard error in dashed lines.

results of this work brings an increased understanding to the potential mechanisms of TTF.

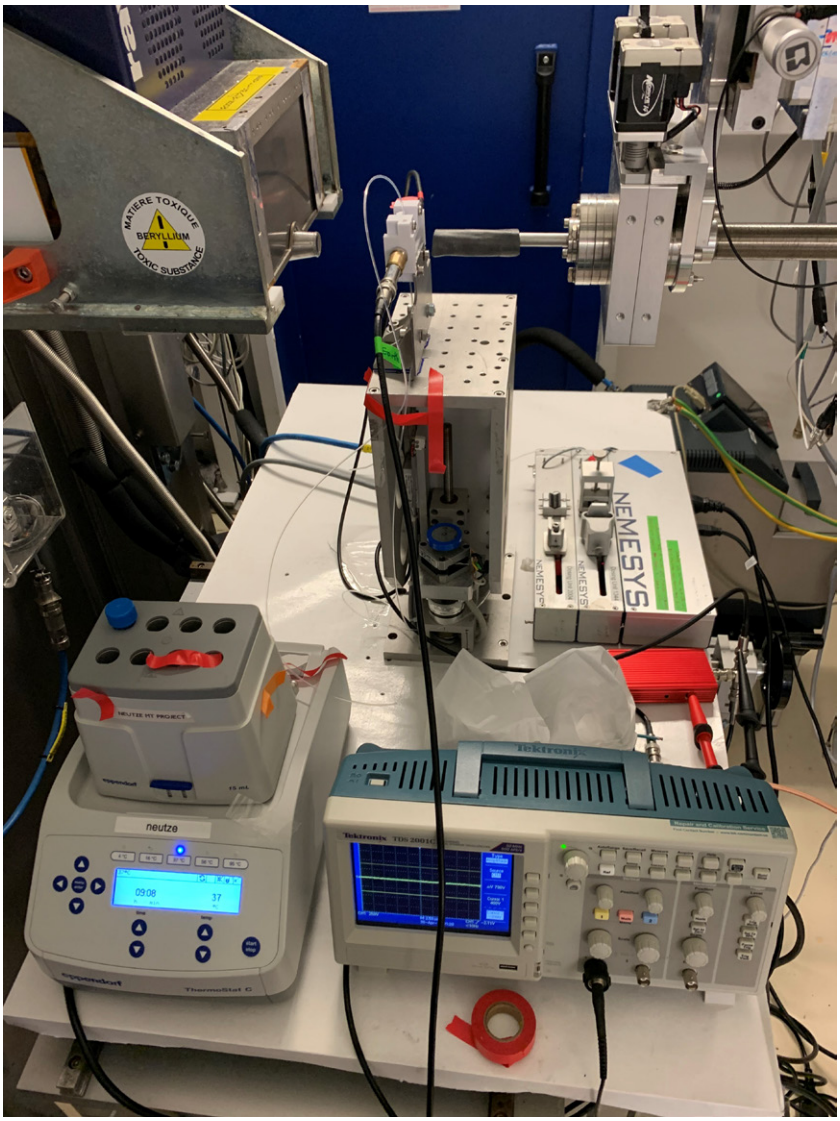

Figure 7.13: Experimental setup for the measurement of potential structural perturbations on microtubules by high voltage alternating electromagnetic fields, ID02 beamline, ESRF

7.4 Outlook

The incredible success of X-ray crystallography at solving atomic structures of biomolecules for over half a century has in, the last decades, been complemented by Cryo-EM, a method rounding the sometimes difficult process of crystallizing proteins. But, is the time for solving static protein structures soon over [302]? The AlphaFold neural network model has produced millions of new protein structures based on their amino acid sequences [303]. The model predictions seems to be in agreement with structures determined by conventional means. A recent version of this deep learning model has been able to predict protein dynamics as determined by molecular dynamics (MD) simulations [304]. This underscores the need for deep learning prediction networks as well as MD simulations to be able to baseline against actual experimental data [305]. To date, however, the time-resolved data on fast protein conformations are scarce and predominantly concern light-sensitive proteins [5, 306]. In order to determine the dynamics of proteins on a larger scale other methods for the initiation and coordination of protein movements must be further developed and utilized [6]. The hopes of a more general method for this using electric fields remain elusive [40]. Investigations of dynamics on larger assemblies of proteins might also hide population differences, something single particle imaging might be able to resolve. Theoretical studies have indicated that atomic resolution structures of single proteins might be gained from single particle imaging, estimating the number of images needed to exceed 3 billion [307]. This number seems unreasonably high, but with the repetition rate of the latest generation of XFELS [308] this is feasible [309].

This thesis covers work that have attempted to further the method of single particle imaging as well as investigated the potential to influence protein structure using electromagnetic fields. In this regard, this thesis represents but a small step on the long road towards a better understanding of our world.

"*So this is the truth as I experienced it, or as it was told to me by those I trusted. Truth, I have learned, differs for everybody. Just as no two people ever see a rainbow in exactly the same place, and yet both most certainly see it, while the person seemingly standing right underneath it does not see it at all. So truth is a question of where one stands and the direction one is looking in at the time. Of course, the reader may chose to differ from me in this belief, and is welcome to do so.*"

Iain M. Banks, *Inversions*

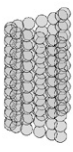

Bibliography

[1] S. Firestein, *Failure*. Oxford University Press, 2015.

[2] Y. Guo, "Be cautious with crystal structures of membrane proteins or complexes prepared in detergents," *Crystals 2020, Vol. 10, Page 86*, vol. 10, p. 86, 2 2020.

[3] H. W. Wang and J. W. Wang, "How cryo-electron microscopy and x-ray crystallography complement each other," *Protein Science*, vol. 26, pp. 32–39, 1 2017.

[4] V. P. Dandey, W. C. Budell, H. Wei, D. Bobe, K. Maruthi, M. Kopylov, E. T. Eng, P. A. Kahn, J. E. Hinshaw, N. Kundu, C. M. Nimigean, C. Fan, N. Sukomon, S. A. Darst, R. M. Saecker, J. Chen, B. Malone, C. S. Potter, and B. Carragher, "Time-resolved cryo-em using spotiton," *Nature Methods 2020 17:9*, vol. 17, pp. 897–900, 8 2020.

[5] G. Brändén and R. Neutze, "Advances and challenges in time-resolved macromolecular crystallography," *Science*, vol. 373, 8 2021.

[6] M. Levantino, B. A. Yorke, D. C. Monteiro, M. Cammarata, and A. R. Pearson, "Using synchrotrons and xfels for time-resolved x-ray crystallography and solution scattering experiments on biomolecules," *Current Opinion in Structural Biology*, vol. 35, pp. 41–48, 12 2015.

[7] K. Henzler-Wildman and D. Kern, "Dynamic personalities of proteins," *Nature 2007 450:7172*, vol. 450, pp. 964–972, 12 2007.

[8] K. A. Henzler-Wildman, M. Lei, V. Thai, S. J. Kerns, M. Karplus, and D. Kern, "A hierarchy of timescales in protein dynamics is linked to enzyme catalysis," *Nature*, vol. 450, pp. 913–916, 2007.

[9] J. D. Chavez, J. P. Mohr, M. Mathay, X. Zhong, A. Keller, and J. E. Bruce, "Systems structural biology measurements by in vivo cross-linking with mass spectrometry," *Nature Protocols 2019 14:8*, vol. 14, pp. 2318–2343, 7 2019.

[10] F. X. Gallat, N. Matsugaki, N. P. Coussens, K. J. Yagi, M. Boudes, T. Higashi, D. Tsuji, Y. Tatano, M. Suzuki, E. Mizohata, K. Tono, Y. Joti, T. Kameshima, J. Park, C. Song, T. Hatsui, M. Yabashi, E. Nango, K. Itoh, F. Coulibaly, S. Tobe, S. Ramaswamy, B. Stay, S. Iwata, and L. M. Chavas, "In vivo crystallography at x-ray free-electron lasers: the next generation of structural biology?," *Philosophical Transactions of the Royal Society B: Biological Sciences*, vol. 369, 7 2014.

[11] S. L. Miller and G. H. Jones, "A production of amino acids under possible primitive earth conditions," *Science*, vol. 117, p. 528, 1953.

[12] L. E. Orgel, "Prebiotic chemistry and the origin of the rna world," *http://dx.doi.org/10.1080/10409230490460765*, vol. 39, pp. 99–123, 3 2010.

[13] H. S. Bernhardt, "The rna world hypothesis: the worst theory of the early evolution of life (except for all the others)a," *Biology Direct*, vol. 7, pp. 1–10, 7 2012.

[14] R. Attal and L. Schwartz, "Thermally driven fission of protocells," *Biophysical Journal*, vol. 120, pp. 3937–3959, sep 2021.

[15] H. M. Harris and C. Hill, "A place for viruses on the tree of life," *Frontiers in Microbiology*, vol. 11, p. 3449, 1 2021.

[16] D. Moreira and P. López-García, "Ten reasons to exclude viruses from the tree of life," *Nature Reviews Microbiology 2009 7:4*, vol. 7, pp. 306–311, 3 2009.

[17] C. R. Woese, O. Kandler, and M. L. Wheelis, "Towards a natural system of organisms: proposal for the domains archaea, bacteria, and eucarya.," *Proceedings of the National Academy of Sciences*, vol. 87, pp. 4576–4579, 6 1990.

[18] A. E. Gorbalenya and C. Lauber, "Phylogeny of viruses," *Reference Module in Biomedical Sciences*, 2017.

[19] D. H. Bamford, J. M. Grimes, and D. I. Stuart, "What does structure tell us about virus evolution?," *Current Opinion in Structural Biology*, vol. 15, pp. 655–663, 12 2005.

[20] J. C. Venter, M. D. Adams, E. W. Myers, P. W. Li, R. J. Mural, G. G. Sutton, H. O. Smith, M. Yandell, C. A. Evans, R. A. Holt, J. D. Gocayne, P. Amanatides, R. M. Ballew, D. H. Huson, J. R. Wortman, Q. Zhang, C. D. Kodira, X. H. Zheng, L. Chen, M. Skupski, G. Subramanian, P. D. Thomas, J. Zhang, G. L. G. Miklos, C. Nelson, S. Broder, A. G. Clark, J. Nadeau, V. A. McKusick, N. Zinder, A. J. Levine, R. J. Roberts, M. Simon, C. Slayman, M. Hunkapiller, R. Bolanos, A. Delcher, I. Dew, D. Fasulo, M. Flanigan, L. Florea, A. Halpern, S. Hannenhalli, S. Kravitz, S. Levy, C. Mobarry, K. Reinert, K. Remington, J. Abu-Threideh, E. Beasley, K. Biddick, V. Bonazzi, R. Brandon, M. Cargill, I. Chandramouliswaran, R. Charlab, K. Chaturvedi, Z. Deng, V. di Francesco, P. Dunn, K. Eilbeck, C. Evangelista, A. E. Gabrielian, W. Gan, W. Ge, F. Gong, Z. Gu, P. Guan, T. J. Heiman, M. E. Higgins, R. R. Ji, Z. Ke, K. A. Ketchum, Z. Lai, Y. Lei, Z. Li, J. Li, Y. Liang, X. Lin, F. Lu, G. V. Merkulov, N. Milshina, H. M. Moore, A. K. Naik, V. A. Narayan, B. Neelam, D. Nusskern, D. B. Rusch, S. Salzberg, W. Shao, B. Shue, J. Sun, Z. Y. Wang, A. Wang, X. Wang, J. Wang, M. H. Wei, R. Wides, C. Xiao, C. Yan, A. Yao, J. Ye, M. Zhan, W. Zhang, H. Zhang, Q. Zhao, L. Zheng, F. Zhong, W. Zhong, S. C. Zhu, S. Zhao, D. Gilbert, S. Baumhueter, G. Spier, C. Carter, A. Cravchik, T. Woodage, F. Ali, H. An, A. Awe, D. Baldwin, H. Baden, M. Barnstead, I. Barrow, K. Beeson, D. Busam, A. Carver, A. Center, M. L. Cheng, L. Curry, S. Danaher, L. Davenport, R. Desilets, S. Dietz, K. Dodson, L. Doup, S. Ferriera, N. Garg, A. Gluecksmann, B. Hart, J. Haynes, C. Haynes, C. Heiner, S. Hladun, D. Hostin, J. Houck, T. Howland, C. Ibegwam, J. Johnson, F. Kalush, L. Kline, S. Koduru, A. Love, F. Mann, D. May, S. McCawley, T. McIntosh, I. McMullen, M. Moy, L. Moy, B. Murphy, K. Nelson, C. Pfannkoch, E. Pratts, V. Puri, H. Qureshi, M. Reardon, R. Rodriguez, Y. H. Rogers, D. Romblad, B. Ruhfel, R. Scott, C. Sitter, M. Smallwood, E. Stewart, R. Strong, E. Suh, R. Thomas, N. N. Tint, S. Tse, C. Vech, G. Wang, J. Wetter, S. Williams, M. Williams, S. Windsor, E. Winn-Deen, K. Wolfe, J. Zaveri, K. Zaveri, J. F. Abril, R. Guigo, M. J. Campbell, K. V. Sjolander, B. Karlak, A. Kejariwal, H. Mi, B. Lazareva, T. Hatton, A. Narechania, K. Diemer, A. Muruganujan, N. Guo, S. Sato, V. Bafna, S. Istrail, R. Lippert, R. Schwartz, B. Walenz, S. Yooseph, D. Allen, A. Basu, J. Baxendale, L. Blick, M. Caminha, J. Carnes-Stine, P. Caulk, Y. H. Chiang, M. Coyne, C. Dahlke, A. D. Mays, M. Dombroski, M. Donnelly, D. Ely, S. Esparham, C. Fosler, H. Gire, S. Glanowski, K. Glasser, A. Glodek, M. Gorokhov, K. Graham, B. Gropman, M. Harris, J. Heil, S. Henderson, J. Hoover, D. Jennings, C. Jordan, J. Jordan, J. Kasha, L. Kagan, C. Kraft, A. Levitsky, M. Lewis, X. Liu, J. Lopez, D. Ma, W. Majoros, J. McDaniel, S. Murphy, M. Newman, T. Nguyen, N. Nguyen, M. Nodell, S. Pan, J. Peck, M. Peterson, W. Rowe, R. Sanders, J. Scott, M. Simpson, T. Smith, A. Sprague, T. Stockwell, R. Turner, E. Venter, M. Wang, M. Wen, D. Wu, M. Wu, A. Xia, A. Zandieh, and X. Zhu, "The sequence of the human genome," *Science*, vol. 291, pp. 1304–1351, 2 2001.

[21] S. Nurk, S. Koren, A. Rhie, M. Rautiainen, A. V. Bzikadze, A. Mikheenko, M. R. Vollger, N. Altemose, L. Uralsky, A. Gershman, S. Aganezov, S. J. Hoyt, M. Diekhans, G. A. Logsdon, M. Alonge, S. E. Antonarakis, M. Borchers, G. G. Bouffard, S. Y. Brooks, G. V. Caldas, N. C. Chen, H. Cheng, C. S. Chin, W. Chow, L. G. de Lima, P. C. Dishuck, R. Durbin, T. Dvorkina, I. T. Fiddes, G. Formenti, R. S. Fulton, A. Fungtammasan, E. Garrison, P. G. Grady, T. A. Graves-Lindsay, I. M. Hall, N. F. Hansen, G. A. Hartley, M. Haukness, K. Howe, M. W. Hunkapiller, C. Jain, M. Jain, E. D. Jarvis, P. Kerpedjiev, M. Kirsche, M. Kolmogorov, J. Korlach, M. Kremitzki, H. Li, V. V. Maduro, T. Marschall, A. M. McCartney, J. McDaniel, D. E. Miller, J. C. Mullikin, E. W. Myers, N. D. Olson, B. Paten, P. Peluso, P. A. Pevzner, D. Porubsky, T. Potapova, E. I. Rogaev, J. A. Rosenfeld, S. L. Salzberg, V. A. Schneider, F. J. Sedlazeck, K. Shafin, C. J. Shew, A. Shumate, Y. Sims, A. F. Smit, D. C. Soto, I. Sovi, J. M. Storer, A. Streets, B. A. Sullivan, F. Thibaud-Nissen, J. Torrance, J. Wagner, B. P. Walenz, A. Wenger, J. M. Wood, C. Xiao, S. M. Yan, A. C. Young, S. Zarate, U. Surti, R. C. McCoy, M. Y. Dennis, I. A. Alexandrov, J. L. Gerton, R. J.

O'Neill, W. Timp, J. M. Zook, M. C. Schatz, E. E. Eichler, K. H. Miga, and A. M. Phillippy, "The complete sequence of a human genome," *Science*, vol. 376, pp. 44–53, 4 2022.

[22] E. A. Ponomarenko, E. V. Poverennaya, E. V. Ilgisonis, M. A. Pyatnitskiy, A. T. Kopylov, V. G. Zgoda, A. V. Lisitsa, and A. I. Archakov, "The size of the human proteome: The width and depth," *International Journal of Analytical Chemistry*, vol. 2016, 2016.

[23] B. Alberts, "The cell as a collection of protein machines: Preparing the next generation of molecular biologists," *Cell*, vol. 92, pp. 291–294, 2 1998.

[24] R. Santos, O. Ursu, A. Gaulton, A. P. Bento, R. S. Donadi, C. G. Bologa, A. Karlsson, B. Al-Lazikani, A. Hersey, T. I. Oprea, and J. P. Overington, "A comprehensive map of molecular drug targets," *Nature reviews. Drug discovery*, vol. 16, p. 19, 12 2017.

[25] A. C. Anderson, "The process of structure-based drug design," *Chemistry & Biology*, vol. 10, pp. 787–797, 9 2003.

[26] L. Hardell, "Health council of the netherlands and evaluation of the fifth generation, 5g, for wireless communication and cancer risks," *World Journal of Clinical Oncology*, vol. 12, p. 393, 6 2021.

[27] I. A. Cotgreave, "Biological stress responses to radio frequency electromagnetic radiation: are mobile phones really so (heat) shocking?," *Archives of Biochemistry and Biophysics*, vol. 435, pp. 227–240, 3 2005.

[28] K. Shrader-Frechette, *Ethics of scientific research*. Rowman & Littlefield Publishers Inc., 1994.

[29] M. Maiuri, M. Garavelli, and G. Cerullo, "Ultrafast spectroscopy: State of the art and open challenges," *Journal of the American Chemical Society*, vol. 142, pp. 3–15, 1 2020.

[30] K. Camilleri, "Heisenberg and the wave–particle duality," *Studies in History and Philosophy of Science Part B: Studies in History and Philosophy of Modern Physics*, vol. 37, pp. 298–315, 6 2006.

[31] A. Sharma, P. Berntsen, R. Harimoorthy, R. Appio, J. Sjöhamn, M. Järvå, A. Björling, G. Hammarin, S. Westenhoff, G. Brändén, and R. Neutze, "A simple adaptation to a protein crystallography station to facilitate difference x-ray scattering studies," *Journal of applied crystallography*, vol. 52, pp. 378–386, 4 2019.

[32] R. Dods, P. Båth, D. Morozov, V. A. Gagnér, D. Arnlund, H. L. Luk, J. Kübel, M. Maj, A. Vallejos, C. Wickstrand, R. Bosman, K. R. Beyerlein, G. Nelson, M. Liang, D. Milathianaki, J. Robinson, R. Harimoorthy, P. Berntsen, E. Malmerberg, L. Johansson, R. Andersson, S. Carbajo, E. Claesson, C. E. Conrad, P. Dahl, G. Hammarin, M. S. Hunter, C. Li, S. Lisova, A. Royant, C. Safari, A. Sharma, G. J. Williams, O. Yefanov, S. Westenhoff, J. Davidsson, D. P. DePonte, S. Boutet, A. Barty, G. Katona, G. Groenhof, G. Brändén, and R. Neutze, "Ultrafast structural changes within a photosynthetic reaction centre," *Nature*, vol. 589, pp. 310–314, 1 2021.

[33] O. Berntsson, A. E. Terry, and T. S. Plivelic, "A setup for millisecond time-resolved x-ray solution scattering experiments at the cosaxs beamline at the max iv laboratory," *Journal of Synchrotron Radiation*, vol. 29, pp. 555–562, 3 2022.

[34] S. Prasad, I. Mandal, S. Singh, A. Paul, B. Mandal, R. Venkatramani, and R. Swaminathan, "Near uv-visible electronic absorption originating from charged amino acids in a monomeric protein," *Chemical Science*, vol. 8, pp. 5416–5433, 7 2017.

[35] M. Lab, "Tubulin basics," 2022.

[36] C. R. Cantor and F. Gaskin, "Turbidimetric studies of the in vitro assembly and disassembly of porcine neurotubules," *J. Mol. Biol*, vol. 89, pp. 737–758, 1974.

[37] B. J. Berne, "Interpretation of the light scattering from long rods," *Journal of Molecular Biology*, vol. 89, no. 4, pp. 755–758, 1974.

[38] Huber and Frost, "Light scattering by small particles," *Aqua*, vol. 47, pp. 87–94, 10 2008.

[39] M. F. Carlier and D. Pantaloni, "Kinetic analysis of cooperativity in tubulin polymerization in the presence of guanosine di- or triphosphate nucleotides," *Biochemistry*, vol. 17, pp. 1908–1915, 5 1978. artikelkopia.

[40] D. R. Hekstra, K. I. White, M. A. Socolich, R. W. Henning, V. Šrajer, and R. Ranganathan, "Electric-field-stimulated protein mechanics.," *Nature*, vol. 540, no. 7633, pp. 400–405, 2016.

[41] J. M. Osepchuk, "A history of microwave heating applications," *IEEE Transactions on Microwave Theory and Techniques*, vol. 32, pp. 1200–1224, 1984.

[42] W. J. Ellison, "Permittivity of pure water, at standard atmospheric pressure, over the frequency range 0–25thz and the temperature range 0–100°c," *Journal of Physical and Chemical Reference Data*, vol. 36, p. 1, 2 2007.

[43] P. Lunkenheimer, S. Emmert, R. Gulich, M. Köhler, M. Wolf, M. Schwab, and A. Loidl, "Electromagnetic-radiation absorption by water," *Physical Review E*, vol. 96, p. 062607, 12 2017.

[44] G. Ziegelberger, R. Croft, M. Feychting, A. C. Green, A. Hirata, G. d'Inzeo, K. Jokela, S. Loughran, C. Marino, S. Miller, G. Oftedal, T. Okuno, E. van Rongen, M. Röösli, Z. Sienkiewicz, J. Tattersall, and S. Watanabe, "Guidelines for limiting exposure to electromagnetic fields (100 khz to 300 ghz)," *Health physics*, vol. 118, pp. 483–524, 5 2020.

[45] T. H. P. Nguyen, Y. Shamis, R. J. Croft, A. Wood, R. L. McIntosh, R. J. Crawford, and E. P. Ivanova, "18 ghz electromagnetic field induces permeability of gram-positive cocci," *Scientific Reports*, vol. 5, pp. 1–12, 2015.

[46] T. H. P. Nguyen, V. T. Pham, V. Baulin, R. J. Croft, R. J. Crawford, and E. P. Ivanova, "The effect of a high frequency electromagnetic field in the microwave range on red blood cells," *Scientific Reports*, vol. 7, pp. 1–10, 2017.

[47] S. Romanenko, P. H. Siegel, D. A. Wagenaar, and V. Pikov, "Effects of millimeter wave irradiation and equivalent thermal heating on the activity of individual neurons in the leech ganglion," *Journal of Neurophysiology*, vol. 112, pp. 2423–2431, 2014.

[48] S. Koyama, E. Narita, Y. Shimizu, Y. Suzuki, T. Shiina, M. Taki, N. Shinohara, and J. Miyakoshi, "Effects of long-term exposure to 60 ghz millimeter-wavelength radiation on the genotoxicity and heat shock protein (hsp) expression of cells derived from human eye," *International Journal of Environmental Research and Public Health 2016, Vol. 13, Page 802*, vol. 13, p. 802, 8 2016.

[49] S. Koyama, E. Narita, Y. Suzuki, T. Shiina, M. Taki, N. Shinohara, and J. Miyakoshi, "Long-term exposure to a 40-ghz electromagnetic field does not affect genotoxicity or heat shock protein expression in hce-t or sra01/04 cells," *Journal of Radiation Research*, vol. 60, pp. 417–423, 7 2019.

[50] K. Karipidis, R. Mate, D. Urban, R. Tinker, and A. Wood, "5g mobile networks and health—a state-of-the-science review of the research into low-level rf fields above 6ghz," *Journal of Exposure Science & Environmental Epidemiology 2021 31:4*, vol. 31, pp. 585–605, 3 2021.

[51] H. Fröhlich, "Long-range coherence and energy storage in biological systems," *International Journal of Quantum Chemistry*, vol. 2, pp. 641–649, 9 1968.

[52] J. R. Reimers, L. K. McKemmish, R. H. McKenzie, A. E. Mark, and N. S. Hush, "Weak, strong, and coherent regimes of fröhlich condensation and their applications to terahertz medicine and quantum consciousness," *Proceedings of the National Academy of Sciences of the United States of America*, vol. 106, pp. 4219–4224, 3 2009.

[53] I. V. Lundholm, H. Rodilla, W. Y. Wahlgren, A. Duelli, G. Bourenkov, J. Vukusic, R. Friedman, J. Stake, T. Schneider, and G. Katona, "Terahertz radiation induces non-thermal structural changes associated with fröhlich condensation in a protein crystal," *Structural Dynamics*, vol. 2, p. 054702, 10 2015.

[54] M. A. Schroer, S. Schewa, A. Y. Gruzinov, C. Rönnau, J. M. Lahey-Rudolph, C. E. Blanchet, T. Zickmantel, Y. H. Song, D. I. Svergun, and M. Roessle, "Probing the existence of non-thermal terahertz radiation induced changes of the protein solution structure," *Scientific Reports*, vol. 11, pp. 1–13, 12 2021.

[55] G. J. Wilmink and J. E. Grundt, "Invited review article: Current state of research on biological effects of terahertz radiation," *Journal of Infrared, Millimeter, and Terahertz Waves*, vol. 32, pp. 1074–1122, 2011.

[56] E. C. Watson, "The discovery of x-rays," *American Journal of Physics*, vol. 13, pp. 281–291, 10 1945.

[57] M. Eckert, "Disputed discovery: the beginnings of x-ray diffraction in crystals in 1912 and its repercussions," *Acta crystallographica. Section A, Foundations of crystallography*, vol. 68, pp. 30–39, 1 2012.

[58] J. C. Spence, "Outrunning damage: Electrons vs x-rays—timescales and mechanisms," *Structural Dynamics*, vol. 4, p. 044027, 6 2017.

[59] F. van der Veen and F. Pfeiffer, "Coherent x-ray scattering," *Journal of Physics: Condensed Matter*, vol. 16, p. 5003, 7 2004.

[60] B. Centennial and J. C. H. Spence, "Foundations of crystallography lawrence bragg, microdiffraction and x-ray lasers," *Acta Cryst*, vol. 69, pp. 25–33, 2013.

[61] P. Debye, "Zerstreuung von röntgenstrahlen," *Annalen der Physik*, vol. 351, pp. 809–823, 1 1915.

[62] M. H. Koch, P. Vachette, and D. I. Svergun, "Small-angle scattering: A view on the properties, structures and structural changes of biological macromolecules in solution," *Quarterly Reviews of Biophysics*, vol. 36, pp. 147–227, 5 2003.

[63] M. F. Perutz, M. G. Rossmann, A. F. Cullis, H. Muirhead, G. Will, and A. C. North, "Structure of hæmoglobin: A three-dimensional fourier synthesis at 5.5-. resolution, obtained by x-ray analysis," *Nature*, vol. 185, pp. 416–422, 1960.

[64] J. C. Kendrew, G. Bodo, H. M. Dintzis, R. G. Parrish, H. Wyckoff, and D. C. Phillips, "A three-dimensional model of the myoglobin molecule obtained by x-ray analysis," *Nature*, vol. 181, pp. 662–666, 3 1958.

[65] K. R. Acharya and M. D. Lloyd, "The advantages and limitations of protein crystal structures," *Trends in Pharmacological Sciences*, vol. 26, pp. 10–14, 1 2005.

[66] Z. Sun, Q. Liu, G. Qu, Y. Feng, and M. T. Reetz, "Utility of b-factors in protein science: Interpreting rigidity, flexibility, and internal motion and engineering thermostability," *Chemical Reviews*, 2019.

[67] R. Henderson, "Cryo-protection of protein crystals against radiation damage in electron and x-ray diffraction," *Proceedings of the Royal Society of London. Series B: Biological Sciences*, vol. 241, pp. 6–8, 7 1990.

[68] M. S. Doscher and F. M. Richards, "The activity of an enzyme in the crystalline state: Ribonuclease s," *Journal of Biological Chemistry*, vol. 238, pp. 2399–2406, 7 1963.

[69] C. Wickstrand, R. Dods, A. Royant, and R. Neutze, "Bacteriorhodopsin: Would the real structural intermediates please stand up?," *Biochimica et Biophysica Acta (BBA) - General Subjects*, vol. 1850, pp. 536–553, 3 2015.

[70] H. Takala, A. Björling, O. Berntsson, H. Lehtivuori, S. Niebling, M. Hoernke, I. Kosheleva, R. Henning, A. Menzel, J. A. Ihalainen, and S. Westenhoff, "Signal amplification and transduction in phytochrome photosensors," *Nature 2014 509:7499*, vol. 509, pp. 245–248, 4 2014.

[71] J. Vincent, M. Andersson, M. Eklund, A. B. Wöhri, M. Odelius, E. Malmerberg, Q. Kong, M. Wulff, R. Neutze, and J. Davidsson, "Solvent dependent structural perturbations of chemical reaction intermediates visualized by time-resolved x-ray diffraction," *The Journal of Chemical Physics*, vol. 130, p. 154502, 4 2009.

[72] M. Andersson, E. Malmerberg, S. Westenhoff, G. Katona, M. Cammarata, A. B. Wöhri, L. C. Johansson, F. Ewald, M. Eklund, M. Wulff, J. Davidsson, and R. Neutze, "Structural dynamics of light-driven proton pumps," *Structure*, vol. 17, pp. 1265–1275, 9 2009.

[73] M. C. Choi, U. Raviv, Y. Li, H. P. Miller, D. J. Needleman, M. W. Kim, L. Wilson, S. C. Feinstein, and C. R. Safinya, "Synchrotron small angle x-ray scattering quantitatively detects angstrom level changes in the average radius of taxol-stabilized microtubules decorated with the microtubule-associated-protein tau," *Journal of Physics: Conference Series*, vol. 272, 2011.

[74] R. Matesanz, J. Rodríguez-Salarichs, B. Pera, Ángeles Canales, J. M. Andreu, J. Jiménez-Barbero, W. Bras, A. Nogales, W. S. Fang, and J. F. Díaz, "Modulation of microtubule interprotofilament interactions by modified taxanes," *Biophysical Journal*, vol. 101, pp. 2970–2980, 2011.

[75] F. Merzel and J. C. Smith, "Is the first hydration shell of lysozyme of higher density than bulk water?," *Proceedings of the National Academy of Sciences of the United States of America*, vol. 99, pp. 5378–5383, 4 2002.

[76] T. Narayanan, M. Sztucki, T. Zinn, A. Homs-Puron, J. Gorini, P. V. Vaerenbergh, and P. Boesecke, "Performance of the time-resolved ultra-small-angle x-ray scattering beamline with the extremely brilliant source," *J. Appl. Cryst*, vol. 55, pp. 98–111, 2022.

[77] B. R. Pauw, "Everything saxs: small-angle scattering pattern collection and correction," *Journal of Physics: Condensed Matter*, vol. 25, p. 383201, 8 2013.

[78] Y. Hwu and G. Margaritondo, "Synchrotron radiation and x-ray free-electron lasers (x-fels) explained to all users, active and potential," *J. Synchrotron Rad*, vol. 28, pp. 1014–1029, 2021.

[79] R. Neutze, R. Wouts, D. V. D. Spoel, E. Weckert, and J. Hajdu, "Potential for biomolecular imaging with femtosecond x-ray pulses," *Nature 2000 406:6797*, vol. 406, pp. 752–757, 8 2000.

[80] D. P. DePonte, U. Weierstall, K. Schmidt, J. Warner, D. Starodub, J. C. Spence, and R. B. Doak, "Gas dynamic virtual nozzle for generation of microscopic droplet streams," *Journal of Physics D: Applied Physics*, vol. 41, p. 195505, 9 2008.

[81] J. Bielecki, M. F. Hantke, B. J. Daurer, H. K. Reddy, D. Hasse, D. S. Larsson, L. H. Gunn, M. Svenda, A. Munke, J. A. Sellberg, L. Flueckiger, A. Pietrini, C. Nettelblad, I. Lundholm, G. Carlsson, K. Okamoto, N. Timneanu, D. Westphal, O. Kulyk, A. Higashiura, G. V. D. Schot, N. T. D. Loh, T. E. Wysong, C. Bostedt, T. Gorkhover, B. Iwan, M. M. Seibert, T. Osipov, P. Walter, P. Hart, M. Bucher, A. Ulmer, D. Ray, G. Carini, K. R. Ferguson, I. Andersson, J. Andreasson, J. Hajdu, and F. R. Maia, "Electrospray sample injection for single-particle imaging with x-ray lasers," *Science Advances*, vol. 5, 2019.

[82] C. Seuring, K. Ayyer, E. Filippaki, M. Barthelmess, J.-N. Longchamp, P. Ringler, T. Pardini, D. Wojtas, M. Coleman, K. Dörner, S. Fuglerud, G. Hammarin, B. Habenstein, A. Langkilde, A. Loquet, A. Meents, R. Riek, H. Stahlberg, S. Boutet, M. Hunter, J. Koglin, M. Liang, H. Ginn, R. Millane, M. Frank, A. Barty, and H. Chapman, "Femtosecond x-ray coherent diffraction of aligned amyloid fibrils on low background grapheme," *Nature Communications*, vol. 9, 2018.

[83] R. K. Cheng, "Towards an optimal sample delivery method for serial crystallography at xfel," *Crystals 2020, Vol. 10, Page 215*, vol. 10, p. 215, 3 2020.

[84] D. M. Mills, J. R. Helliwell, A. Kvick, T. Ohta, I. A. Robinson, and A. Authier, "Report of the working group on synchrotron radiation nomenclature – brightness, spectral brightness or brilliance?," *urn:issn:0909-0495*, vol. 12, pp. 385–385, 4 2005.

[85] M. Cammarata, L. Eybert, F. Ewald, W. Reichenbach, M. Wulff, P. Anfinrud, F. Schotte, A. Plech, Q. Kong, M. Lorenc, B. Lindenau, J. Räbiger, and S. Polachowski, "Chopper system for time resolved experiments with synchrotron radiation," *The Review of scientific instruments*, vol. 80, 2009.

[86] T. Graber, S. Anderson, H. Brewer, Y. S. Chen, H. S. Cho, N. Dashdorj, R. W. Henning, I. Kosheleva, G. MacHa, M. Meron, R. Pahl, Z. Ren, S. Ruan, F. Schotte, V. Šrajer, P. J. Viccaro, F. Westferro, P. Anfinrud, and K. Moffat, "Biocars: a synchrotron resource for time-resolved x-ray science," *urn:issn:0909-0495*, vol. 18, pp. 658–670, 5 2011.

[87] S. Westenhoff, E. Malmerberg, D. Arnlund, L. Johansson, E. Nazarenko, M. Cammarata, J. Davidsson, V. Chaptal, J. Abramson, G. Katona, A. Menzel, and R. Neutze, "Rapid readout

detector captures protein time-resolved waxs," *Nature Methods 2010 7:10*, vol. 7, pp. 775–776, 9 2010.

[88] A. Björling, O. Berntsson, H. Lehtivuori, H. Takala, A. J. Hughes, M. Panman, M. Hoernke, S. Niebling, L. Henry, R. Henning, I. Kosheleva, V. Chukharev, N. V. Tkachenko, A. Menzel, G. Newby, D. Khakhulin, M. Wulff, J. A. Ihalainen, and S. Westenhoff, "Structural photoactivation of a full-length bacterial phytochrome," *Science Advances*, vol. 2, 8 2016.

[89] P. F. Tavares, E. Al-Dmour, A. K. Andersson, F. Cullinan, B. N. Jensen, D. Olsson, D. K. Olsson, M. Sjöström, H. Tarawneh, S. Thorin, and A. Vorozhtsov, "Commissioning and first-year operational results of the max iv 3 gev ring," *J. Synchrotron Rad*, vol. 25, pp. 1291–1316, 2018.

[90] D. Arnlund, L. C. Johansson, C. Wickstrand, A. Barty, G. J. Williams, E. Malmerberg, J. Davidsson, D. Milathianaki, D. P. DePonte, R. L. Shoeman, D. Wang, D. James, G. Katona, S. Westenhoff, T. A. White, A. Aquila, S. Bari, P. Berntsen, M. Bogan, T. B. V. Driel, R. B. Doak, K. S. Kjær, M. Frank, R. Fromme, I. Grotjohann, R. Henning, M. S. Hunter, R. A. Kirian, I. Kosheleva, C. Kupitz, M. Liang, A. V. Martin, M. M. Nielsen, M. Messerschmidt, M. M. Seibert, J. Sjöhamn, F. Stellato, U. Weierstall, N. A. Zatsepin, J. C. Spence, P. Fromme, I. Schlichting, S. Boutet, G. Groenhof, H. N. Chapman, and R. Neutze, "Visualizing a protein quake with time-resolved x-ray scattering at a free-electron laser," *Nature Methods 2014 11:9*, vol. 11, pp. 923–926, 8 2014.

[91] M. E. Valentinuzzi, "Highlights in the history of the fourier transform," Jan 2016.

[92] T. A. Gallagher, A. J. Nemeth, and L. Hacein-Bey, "An introduction to the fourier transform: relationship to mri," *AJR. American journal of roentgenology*, vol. 190, pp. 1396–1405, 5 2008.

[93] M. Scigelova, M. Hornshaw, A. Giannakopulos, and A. Makarov, "Fourier transform mass spectrometry," *Molecular and Cellular Proteomics*, vol. 10, p. M111.009431, 2011.

[94] C. Berthomieu and R. Hienerwadel, "Fourier transform infrared (ftir) spectroscopy," *Photosynthesis Research*, vol. 101, pp. 157–170, 9 2009.

[95] A. Alfalou and C. Brosseau, "Optical image compression and encryption methods," *Advances in Optics and Photonics, Vol. 1, Issue 3, pp. 589-636*, vol. 1, pp. 589–636, 11 2009.

[96] J. W. Cooley and J. W. Tukey, "An algorithm for the machine calculation of complex fourier series," *Mathematics of Computation*, vol. 19, p. 297, 4 1965.

[97] W. A. Hendrickson, "Anomalous diffraction in crystallographic phase evaluation," *Quarterly reviews of biophysics*, vol. 47, p. 49, 2014.

[98] R. W. Gerchberg and W. O. Saxton, "Practical algorithm for determination of phase from image and diffraction plane pictures," *OPTIK*, vol. 35, no. 2, pp. 237–&, 1972.

[99] T. Latychevskaia, "Iterative phase retrieval in coherent diffractive imaging: practical issues," *Applied Optics, Vol. 57, Issue 25, pp. 7187-7197*, vol. 57, pp. 7187–7197, 9 2018.

[100] S. Marchesini, "A unified evaluation of iterative projection algorithms for phase retrieval," *Review of Scientific Instruments*, vol. 78, p. 011301, 1 2007.

[101] J. Miao, T. Ishikawa, I. K. Robinson, and M. M. Murnane, "Beyond crystallography: Diffractive imaging using coherent x-ray light sources," *Science*, vol. 348, pp. 530–535, 5 2015.

[102] E. Frixione, "Recurring views on the structure and function of the cytoskeleton: A 300-year epic," *Cell Motility and the Cytoskeleton*, vol. 46, pp. 73–94, 6 2000.

[103] N. Koltzoff, "Experimental biology and the work of the moscow institute," *Science*, vol. 59, pp. 497–502, 6 1924.

[104] P. Wintrebert, "La rotation immédiate de l'oeuf pondu et la rotation d'activation chez discoglossus pictus otth," *CR Soc. Biol*, vol. 106, pp. 439–442, 1931.

[105] F. Zampieri, M. Coen, and G. Gabbiani, "The prehistory of the cytoskeleton concept," *Cytoskeleton*, vol. 71, pp. 464–471, 8 2014.

[106] R. S. Bear, F. O. Schmitt, and J. Z. Young, "The ultrastructure of nerve axoplasm," *Proceedings of the Royal Society of London. Series B - Biological Sciences*, vol. 123, pp. 505–519, 8 1937.

[107] E. de Robertis and F. O. Schmitt, "An electron microscope analysis of certain nerve axon constituents," *Journal of Cellular and Comparative Physiology*, vol. 31, pp. 1–23, 2 1948.

[108] D. B. Slautterback, "Cytoplasmic microtubules. i. hydra.," *The Journal of cell biology*, vol. 18, pp. 367–388, 8 1963.

[109] S. Inoué and H. Sato, "Cell motility by labile association of molecules: The nature of mitotic spindle fibers and their role in chromosome movement," *Journal of General Physiology*, vol. 50, pp. 259–292, 1 1967.

[110] G. Borisy, R. Heald, J. Howard, C. Janke, A. Musacchio, and E. Nogales, "Microtubules: 50 years on from the discovery of tubulin," *Nature Reviews Molecular Cell Biology*, vol. 17, pp. 322–328, 4 2016.

[111] B. Wickstead and K. Gull, "The evolution of the cytoskeleton," *Journal of Cell Biology*, vol. 194, pp. 513–525, 8 2011.

[112] P. D. Boer, R. Crossley, and L. Rothfield, "The essential bacterial cell-division protein ftsz is a gtpase," *Nature*, vol. 359, pp. 254–256, 1992.

[113] D. RayChaudhuri and J. T. Park, "Escherichia coli cell-division gene ftsz encodes a novel gtp-binding protein," *Nature*, vol. 359, pp. 251–254, 1992.

[114] A. I. Derman, E. C. Becker, B. D. Truong, A. Fujioka, T. M. Tucey, M. L. Erb, P. C. Patterson, and J. Pogliano, "Phylogenetic analysis identifies many uncharacterized actin-like proteins (alps) in bacteria: Regulated polymerization, dynamic instability and treadmilling in alp7a," *Molecular Microbiology*, vol. 73, pp. 534–552, 8 2009.

[115] J. Löwe and L. A. Amos, "Evolution of cytomotive filaments: The cytoskeleton from prokaryotes to eukaryotes," *International Journal of Biochemistry and Cell Biology*, vol. 41, pp. 323–329, 2 2009.

[116] A. Desai and T. J. Mitchison, "Microtubule polymerization dynamics," *Annual Review of Cell and Developmental Biology*, vol. 13, pp. 83–117, 1997.

[117] R. Dominguez and K. C. Holmes, "Actin structure and function," *Annual Review of Biophysics*, vol. 40, pp. 169–186, 6 2011.

[118] N. Dhanyasi, K. VijayRaghavan, B. Shilo, and E. D. Schejter, "Microtubules provide guidance cues for myofibril and sarcomere assembly and growth," *Developmental Dynamics*, vol. 250, pp. 60–73, 1 2021.

[119] S. Boudriau, M. Vincent, C. H. Cote, and P. A. Rogers, "Cytoskeletal structure of skeletal muscle: Identification of an intricate exosarcomeric microtubule lattice in slow- and fast-twitch muscle fibers," *Journal of Histochemistry and Cytochemistry*, vol. 41, pp. 1013–1021, 1993.

[120] H. Herrmann, H. Bär, L. Kreplak, S. V. Strelkov, and U. Aebi, "Intermediate filaments: From cell architecture to nanomechanics," *Nature Reviews Molecular Cell Biology*, vol. 8, pp. 562–573, 7 2007.

[121] R. G. Burns, "alpha-, beta-, and gamma-tubulins: Sequence comparisons and structural constraints," *Cell Motility and the Cytoskeleton*, vol. 20, pp. 181–189, 1 1991.

[122] L. G. Tilney, J. Bryan, D. J. Bush, K. Fujiwara, M. S. Mooseker, D. B. Murphy, and D. H. Snyder, "Microtubules: Evidence for 13 protofilaments," *Journal of Cell Biology*, vol. 59, pp. 267–275, 11 1973.

[123] G. B. Pierson, P. R. Burton, and R. H. Himes, "Alterations in number of protofilaments in microtubules assembled in vitro.," *The Journal of Cell Biology*, vol. 76, pp. 223–228, 1 1978.

[124] H. Li, D. J. DeRosier, W. V. Nicholson, E. Nogales, and K. H. Downing, "Microtubule structure at 8 Å resolution," *Structure*, vol. 10, pp. 1317–1328, 10 2002.

[125] S. Chaaban and G. J. Brouhard, "A microtubule bestiary: Structural diversity in tubulin polymers," *Molecular Biology of the Cell*, vol. 28, pp. 2924–2931, 11 2017.

[126] R. A. Walker, E. T. O'Brien, N. K. Pryer, M. F. Soboeiro, W. A. Voter, H. P. Erickson, and E. D. Salmon, "Dynamic instability of individual microtubules analyzed by video light microscopy: rate constants and transition frequencies.," *Journal of Cell Biology*, vol. 107, pp. 1437–1448, 10 1988.

[127] M. A. Tischfield and E. C. Engle, "Distinct α - and β-tubulin isotypes are required for the positioning, differentiation and survival of neurons: New support for the 'multi-tubulin' hypothesis," *Bioscience Reports*, vol. 30, pp. 319–330, 10 2010.

[128] Z. X. Wang, L. Tan, and J. T. Yu, "Axonal transport defects in alzheimer's disease," *Molecular Neurobiology*, vol. 51, pp. 1309–1321, 6 2015.

[129] J. Mizushima-Sugano, T. Maeda, and T. Miki-Noumura, "Flexural rigidity of singlet microtubules estimated from statistical analysis of their contour lengths and end-to-end distances," *BBA - General Subjects*, vol. 755, pp. 257–262, 1 1983.

[130] P. Venier, A. C. Maggs, M. F. Carlier, and D. Pantaloni, "Analysis of microtubule rigidity using hydrodynamic flow and thermal fluctuations," *Journal of Biological Chemistry*, vol. 269, pp. 13353–13360, 5 1994.

[131] M. D. Koch, N. Schneider, P. Nick, and A. Rohrbach, "Single microtubules and small networks become significantly stiffer on short time-scales upon mechanical stimulation," *Scientific Reports*, pp. 1–15, 2017.

[132] T. Hawkins, M. Mirigian, M. S. Yasar, and J. L. Ross, "Mechanics of microtubules," *Journal of Biomechanics*, vol. 43, pp. 23–30, 1 2010.

[133] M. L. Gardel, K. E. Kasza, C. P. Brangwynne, J. Liu, and D. A. Weitz, "Chapter 19 mechanical response of cytoskeletal networks," *Methods in Cell Biology*, vol. 89, pp. 487–519, 1 2008.

[134] M. Wieczorek, S. Bechstedt, S. Chaaban, and G. J. Brouhard, "Microtubule-associated proteins control the kinetics of microtubule nucleation," *Nature Cell Biology*, vol. 17, pp. 907–916, 2015.

[135] K. Tsuchiya and G. Goshima, "Microtubule-associated proteins promote microtubule generation in the absence of γ-tubulin in human colon cancer cells," *The Journal of cell biology*, vol. 220, 12 2021.

[136] A. K. Singla, A. Garg, and D. Aggarwal, "Paclitaxel and its formulations," *International Journal of Pharmaceutics*, vol. 235, pp. 179–192, 3 2002.

[137] I. Arnal and R. H. Wade, "How does taxol stabilize microtubules?," *Current Biology*, vol. 5, pp. 900–908, 1995.

[138] V. Martin, "Overview of paclitaxel (taxol®)," *Seminars in Oncology Nursing*, vol. 9, pp. 2–5, 11 1993.

[139] C. Dumontet and M. A. Jordan, "Microtubule-binding agents: a dynamic field of cancer therapeutics," *Nature Reviews. Drug Discovery*, vol. 9, p. 790, 2010.

[140] D. Zabeo, J. T. Croft, and J. L. Höög, "Axonemal doublet microtubules can split into two complete singlets in human sperm flagellum tips," *FEBS Letters*, vol. 593, pp. 892–902, 5 2019.

[141] A. J. Roberts, T. Kon, P. J. Knight, K. Sutoh, and S. A. Burgess, "Functions and mechanics of dynein motor proteins," *Nature Reviews Molecular Cell Biology 2013 14:11*, vol. 14, pp. 713–726, 9 2013.

[142] R. D. Vale and R. A. Milligan, "The way things move: Looking under the hood of molecular motor proteins," *Science*, vol. 288, p. 88, 4 2000.

[143] H. T. Vu, Z. Zhang, R. Tehver, and D. Thirumalai, "Plus and minus ends of microtubules respond asymmetrically to kinesin binding by a long-range directionally driven allosteric mechanism," *Science Advances*, vol. 8, p. 856, 4 2022.

[144] P. Guedes-Dias and E. L. Holzbaur, "Axonal transport: Driving synaptic function," *Science*, vol. 366, 10 2019.

[145] S. E. Siegrist and C. Q. Doe, "Microtubule-induced cortical cell polarity," *Genes and Development*, vol. 21, pp. 483–496, 3 2007.

[146] E. J. Cuenca-Zamora, F. Ferrer-Marín, J. Rivera, and R. Teruel-Montoya, "Tubulin in platelets: When the shape matters," *International Journal of Molecular Sciences*, vol. 20, 7 2019.

[147] L. O'Donnell and M. K. O'Bryan, "Microtubules and spermatogenesis," *Seminars in Cell & Developmental Biology*, vol. 30, pp. 45–54, 6 2014.

[148] P. G. Wilson and G. G. Borisy, "Evolution of the multi-tubulin hypothesis," *BioEssays*, vol. 19, pp. 451–454, 1997.

[149] R. F. Ludueña, "Are tubulin isotypes functionally significant," *Molecular Biology of the Cell*, vol. 4, pp. 445–457, 10 1993.

[150] C. Janke and M. M. Magiera, "The tubulin code and its role in controlling microtubule properties and functions," *Nature Reviews Molecular Cell Biology*, vol. 21, pp. 307–326, 6 2020.

[151] E. H. Kellogg, N. M. Hejab, S. Poepsel, K. H. Downing, F. DiMaio, and E. Nogales, "Near-atomic model of microtubule-tau interactions," *Science*, vol. 360, pp. 1242–1246, 6 2018.

[152] H. G. N. Committee, "HUGO Gene Nomenclature Committee. Gene group: Tubulins." `https://www.genenames.org/data/genegroup/#!/group/778`, 2022. [Online; accessed 2022-08-26].

[153] H. Ponstingl, E. Krauhs, M. Little, and T. Kempf, "Complete amino acid sequence of alpha-tubulin from porcine brain.," *Proceedings of the National Academy of Sciences of the United States of America*, vol. 78, p. 2757, 1981.

[154] H. D. Schwer, P. Lecine, S. Tiwari, J. E. Italiano, J. H. Hartwig, and R. A. Shivdasani, "A lineage-restricted and divergent β-tubulin isoform is essential for the biogenesis, structure and function of blood platelets," *Current Biology*, vol. 11, pp. 579–586, 4 2001.

[155] S. C. Ti, G. M. Alushin, and T. M. Kapoor, "Human β-tubulin isotypes can regulate microtubule protofilament number and stability," *Developmental Cell*, vol. 47, pp. 175–190.e5, 10 2018.

[156] S. Chaaban, S. Jariwala, C. T. Hsu, S. Redemann, J. M. Kollman, T. Müller-Reichert, D. Sept, K. H. Bui, and G. J. Brouhard, "The structure and dynamics of c. elegans tubulin reveals the mechanistic basis of microtubule growth," *Developmental Cell*, vol. 47, pp. 191–204.e8, 10 2018.

[157] J. G. Cueva, J. Hsin, K. C. Huang, and M. B. Goodman, "Posttranslational acetylation of α-tubulin constrains protofilament number in native microtubules," *Current Biology*, vol. 22, pp. 1066–1074, 6 2012.

[158] J. G. Gall, "Microtubule fine structure.," *The Journal of cell biology*, vol. 31, pp. 639–643, 12 1966.

[159] L. A. Amos and T. S. Baker, "The three-dimensional structure of tubulin protofilaments," *Nature*, vol. 279, pp. 607–612, 1979.

[160] L. Beese, G. Stubbs, and C. Cohen, "Microtubule structure at 18 Å resolution," *Journal of Molecular Biology*, vol. 194, pp. 257–264, 3 1987.

[161] E. Nogales, S. G. Wolf, and K. H. Downing, "Structure of the $\alpha\beta$ tubulin dimer by electron crystallography," *Nature*, vol. 391, pp. 199–203, 1 1998.

[162] G. M. Alushin, G. C. Lander, E. H. Kellogg, R. Zhang, D. Baker, and E. Nogales, "High-resolution microtubule structures reveal the structural transitions in $\alpha\beta$-tubulin upon gtp hydrolysis," *Cell*, vol. 157, pp. 1117–1129, 5 2014.

[163] D. Zabeo, J. M. Heumann, C. L. Schwartz, A. Suzuki-Shinjo, G. Morgan, P. O. Widlund, and J. L. Höög, "A lumenal interrupted helix in human sperm tail microtubules," *Scientific Reports*, vol. 8, pp. 1–11, 12 2018.

[164] J. Bordas, E. M. Mandelkow, and E. Mandelkow, "Stages of tubulin assembly and disassembly studied by time-resolved synchrotron x-ray scattering," *Journal of Molecular Biology*, vol. 164, pp. 89–135, 1983.

[165] J. M. Andreu, J. Bordas, J. F. Diaz, J. G. de Ancos, R. Gil, F. J. Medrano, E. Nogales, E. Pantos, and E. Towns-Andrews, "Low resolution structure of microtubules in solution. synchrotron x-ray scattering and electron microscopy of taxol-induced microtubules assembled from purified tubulin in comparison with glycerol and map-induced microtubules," *Journal of Molecular Biology*, vol. 226, pp. 169–184, 1992.

[166] J. R. Zabrecky and R. D. Cole, "Binding of atp to tubulin," *Nature 1982 296:5859*, vol. 296, pp. 775–776, 1982.

[167] T. W. Traut, "Physiological concentrations of purines and pyrimidines," *Molecular and Cellular Biochemistry 1994 140:1*, vol. 140, pp. 1–22, 11 1994.

[168] V. Barsegov, J. L. Ross, and R. I. Dima, "Dynamics of microtubules: Highlights of recent computational and experimental investigations," *Journal of Physics Condensed Matter*, vol. 29, 2017.

[169] M. Kirschner and T. Mitchison, "Beyond self-assembly: From microtubules to morphogenesis," *Cell*, vol. 45, pp. 329–342, 5 1986.

[170] U. S. Tulu, C. Fagerstrom, N. P. Ferenz, and P. Wadsworth, "Molecular requirements for kinetochore-associated microtubule formation in mammalian cells," *Current Biology*, vol. 16, pp. 536–541, 3 2006.

[171] H. Bowne-Anderson, A. Hibbel, and J. Howard, "Regulation of microtubule growth and catastrophe: Unifying theory and experiment," *Trends in Cell Biology*, vol. 25, pp. 769–779, 12 2015.

[172] N. A. Baker, D. Sept, S. Joseph, M. J. Holst, and J. A. McCammon, "Electrostatics of nanosystems: Application to microtubules and the ribosome," *Proceedings of the National Academy of Sciences of the United States of America*, vol. 98, pp. 10037–10041, 8 2001.

[173] J. A. Tuszyński, J. A. Brown, E. Crawford, E. J. Carpenter, M. L. Nip, J. M. Dixon, and M. V. Satarić, "Molecular dynamics simulations of tubulin structure and calculations of electrostatic properties of microtubules," *Mathematical and Computer Modelling*, vol. 41, pp. 1055–1070, 2005.

[174] A. P. Kalra, B. B. Eakins, S. D. Patel, G. Ciniero, V. Rezania, K. Shankar, and J. A. Tuszynski, "All wired up: An exploration of the electrical properties of microtubules and tubulin," *ACS Nano*, vol. 14, pp. 16301–16320, 12 2020.

[175] R. Tucker, P. Katira, and H. Hess, "Herding nanotransporters: Localized activation via release and sequestration of control molecules," *Nano Letters*, vol. 8, pp. 221–226, 1 2008.

[176] D. V. Nicolau, M. Lard, T. Korten, F. C. V. Delft, M. Persson, E. Bengtsson, A. Månsson, S. Diez, H. Linke, and D. V. Nicolau, "Parallel computation with molecular-motor-propelled agents in nanofabricated networks," *Proceedings of the National Academy of Sciences of the United States of America*, vol. 113, pp. 2591–2596, 3 2016.

[177] M. G. V. D. Heuvel, M. P. D. Graaff, S. G. Lemay, and C. Dekker, "Electrophoresis of individual microtubules in microchannels," *Proceedings of the National Academy of Sciences of the United States of America*, vol. 104, pp. 7770–7775, 5 2007.

[178] K. J. Böhm, N. E. Mavromatos, A. Michette, R. Stracke, and E. Unger, "Movement and alignment of microtubules in electric fields and electric-dipole-moment estimates," *Electromagnetic Biology and Medicine*, vol. 24, pp. 319–330, 1 2005.

[179] T. Kim, M. T. Kao, E. F. Hasselbrink, and E. Meyhöfer, "Active alignment of microtubules with electric fields," *Nano Letters*, vol. 7, pp. 211–217, 1 2007.

[180] M. Uppalapati, Y. M. Huang, T. N. Jackson, and W. O. Hancock, "Microtubule alignment and manipulation using ac electrokinetics," *Small*, vol. 4, pp. 1371–1381, 9 2008.

[181] A. Mershin, A. A. Kolomenski, H. A. Schuessler, and D. V. Nanopoulos, "Tubulin dipole moment, dielectric constant and quantum behavior: computer simulations, experimental results and suggestions," *Biosystems*, vol. 77, pp. 73–85, 11 2004.

[182] C. E. Felder, J. Prilusky, I. Silman, and J. L. Sussman, "A server and database for dipole moments of proteins," *Nucleic Acids Research*, vol. 35, pp. W512–W521, 7 2007.

[183] R. C. Weisenberg, G. G. Borisy, and E. W. Taylor, "The colchicine-binding protein of mammalian brain and its relation to microtubules," *Biochemistry*, vol. 7, pp. 4466–4479, 12 1968.

[184] R. C. Weisenberg, "Microtubule formation in vitro in solutions containing low calcium concentrations," *Science*, vol. 177, pp. 1104–1105, 9 1972.

[185] J. F. Díaz, J. M. Valpuesta, P. Chacón, G. Diakun, and J. M. Andreu, "Changes in microtubule protofilament number induced by taxol binding to an easily accessible site: Internal microtubule dynamics," *Journal of Biological Chemistry*, vol. 273, pp. 33803–33810, 1998.

[186] G. G. Borisy, J. M. Marcum, J. B. Olmsted, D. B. Murphy, and K. A. Johnson, "Purification of Tubulin and associated high molecular weight proteins from porcine brain and charachterization of microtubule assembly in vitro.," *Annals of the New York Academy of Sciences*, vol. 253, no. 1, pp. 107–132, 1975.

[187] K. A. Johnson and G. G. Borisy, "Kinetic analysis of microtubule self-assembly in vitro," *Journal of Molecular Biology*, vol. 117, pp. 1–31, 1977.

[188] W. A. Voter and H. P. Erickson, "The kinetics of microtubule assembly. evidence for a two-stage nucleation mechanism," *Journal of Biological Chemistry*, vol. 259, pp. 10430–10438, 8 1984.

[189] D. K. Fygenson, H. Flyvbjerg, K. Sneppen, A. Libchaber, and S. Leibler, "Spontaneous nucleation of microtubules," *Physical Review E*, vol. 51, pp. 5058–5063, 5 1995.

[190] D. K. Fygenson, E. Braun, A. Libchaber, and S. Barbara, "Phase-diagram of microtubules," *Physical Review E*, vol. 50, pp. 1579–1588, 1994.

[191] F. Oosawa and M. Kasai, "A theory of linear and helical aggregations of macromolecules," *Journal of Molecular Biology*, vol. 4, pp. 10–21, 1 1962.

[192] T. Mitchison and M. Kirschner, "Dynamic instability of microtubule growth," *Nature*, vol. 312, pp. 237–242, 1984.

[193] T. Mitchison and M. Kirschner, "Microtubule assembly nucleated by isolated centrosomes," *Nature*, vol. 312, pp. 232–237, 1984.

[194] T. Horio and H. Hotani, "Visualization of the dynamic instability of individual microtubules by dark-field microscopy," *Nature*, vol. 321, pp. 605–607, 1986.

[195] R. C. Weisenberg, W. J. Deery, and P. J. Dickinson, "Tubulin-nucleotide interactions during the polymerization and depolymerization of microtubules," *Biochemistry*, vol. 15, pp. 4248–4254, 9 1976.

[196] A. A. Hyman, S. Salser, D. N. Drechsel, N. Unwin, and T. J. Mitchison, "Role of gtp hydrolysis in microtubule dynamics: information from a slowly hydrolyzable analogue, gmpcpp.," *https://doi.org/10.1091/mbc.3.10.1155*, vol. 3, pp. 1155–1167, 10 1992.

[197] D. J. Odde, "Estimation of the diffusion-limited rate of microtubule assembly," *Biophysical Journal*, vol. 73, pp. 88–96, 1997.

[198] H. T. Schek, M. K. Gardner, J. Cheng, D. J. Odde, and A. J. Hunt, "Microtubule assembly dynamics at the nanoscale," *Current Biology*, vol. 17, pp. 1445–1455, 9 2007.

[199] R. J. Ellis, "Macromolecular crowding: obvious but underappreciated," *Trends in Biochemical Sciences*, vol. 26, pp. 597–604, 10 2001.

[200] M. L. Shelanski, F. Gaskin, and C. R. Cantor, "Microtubule assembly in the absence of added nucleotides.," *Proceedings of the National Academy of Sciences of the United States of America*, vol. 70, pp. 765–768, 1973.

[201] R. A. Keates, "Effects of glycerol on microtubule polymerization kinetics," *Biochemical and Biophysical Research Communications*, vol. 97, pp. 1163–1169, 12 1980.

[202] M. Wieczorek, S. Chaaban, and G. J. Brouhard, "Macromolecular crowding pushes catalyzed microtubule growth to near the theoretical limit," *Cellular and Molecular Bioengineering*, vol. 6, pp. 383–392, 12 2013.

[203] M. K. Gardner, B. D. Charlebois, I. M. Jánosi, J. Howard, A. J. Hunt, and D. J. Odde, "Rapid microtubule self-assembly kinetics," *Cell*, vol. 146, pp. 582–592, 2011.

[204] The Mathworks, Inc., Natick, Massachusetts, *MATLAB version 9.13.0.2049777 (R2022b)*, 2022.

[205] D. B. Murphy and R. R. Hiebsch, "Purification of microtubule protein from beef brain and comparison of the assembly requirements for neuronal microtubules isolated from beef and hog," *Analytical Biochemistry*, vol. 96, pp. 225–235, jul 1979.

[206] M. Castoldi and A. V. Popov, "Purification of brain tubulin through two cycles of polymerization-depolymerization in a high-molarity buffer," *Protein Expression and Purification*, vol. 32, pp. 83–88, 2003.

[207] F. O. Morin, F. Rose, P. Martin, M. C. Tarhan, H. Kawakatsu, and H. Fujita, "Combing and self-assembly phenomena in dry films of taxol-stabilized microtubules," *Nanoscale Research Letters*, vol. 2, pp. 135–143, 2007.

[208] C. Elie-Caille, F. Severin, J. Helenius, J. Howard, D. J. Muller, and A. A. Hyman, "Straight gdp-tubulin protofilaments form in the presence of taxol," *Current Biology*, vol. 17, pp. 1765–1770, 2007.

[209] I. Cytoskeleton, "Comparison of the biochemical characteristics of bovine brain and porcine brain tubulin," 2008.

[210] D. K. Cullen, J. P. Harris, K. D. Browne, J. A. Wolf, J. E. Duda, D. F. Meaney, S. S. Margulies, and D. H. Smith, "A porcine model of traumatic brain injury via head rotational acceleration," in *Methods in Molecular Biology*, vol. 1462, pp. 289–324, Humana Press Inc., 2016.

[211] B. Hoffe and M. R. Holahan, "The use of pigs as a translational model for studying neurodegenerative diseases," *Frontiers in Physiology*, vol. 10, p. 838, 7 2019.

[212] M. Cifra, J. Pokorný, D. Havelka, and O. Kučera, "Electric field generated by axial longitudinal vibration modes of microtubule," *BioSystems*, vol. 100, pp. 122–131, 5 2010.

[213] D. Havelka, M. Cifra, O. Kučera, J. Pokorný, and J. Vrba, "High-frequency electric field and radiation characteristics of cellular microtubule network," *Journal of Theoretical Biology*, vol. 286, pp. 31–40, 2011.

[214] I. B. Santelices, D. E. Friesen, C. Bell, C. M. Hough, J. Xiao, A. Kalra, P. Kar, H. Freedman, V. Rezania, J. D. Lewis, K. Shankar, and J. A. Tuszynski, "Response to alternating electric fields of tubulin dimers and microtubule ensembles in electrolytic solutions," *Scientific Reports*, vol. 7, 2017.

[215] S. Sahu, S. Ghosh, D. Fujita, and A. Bandyopadhyay, "Live visualizations of single isolated tubulin protein self-assembly via tunneling current: effect of electromagnetic pumping during spontaneous growth of microtubule," *Scientific Reports 2014 4:1*, vol. 4, pp. 1–9, 12 2014.

[216] A. Afrasiabi, G. H. Riazi, A. Dadras, E. Tavili, B. Ghalandari, A. Naghshineh, H. Mobasheri, and S. Ahmadian, "Electromagnetic fields with 217 hz and 0.2 mt as hazardous factors for tubulin structure and assembly (in vitro study)," *Journal of the Iranian Chemical Society*, vol. 11, pp. 1295–1304, 12 2014.

[217] P. Marracino, D. Havelka, J. Průša, M. Liberti, J. Tuszynski, A. T. Ayoub, F. Apollonio, and M. Cifra, "Tubulin response to intense nanosecond-scale electric field in molecular dynamics simulation," *Scientific Reports*, vol. 9, pp. 1–14, 2019.

[218] J. J. Timmons, J. Preto, J. A. Tuszynski, and E. T. Wong, "Tubulin's response to external electric fields by molecular dynamics simulations," *PLoS ONE*, vol. 13, 9 2018.

[219] H. R. Saeidi, A. Lohrasebi, and K. Mahnam, "External electric field effects on the mechanical properties of the $\alpha\beta$-tubulin dimer of microtubules: A molecular dynamics study," *Journal of Molecular Modeling*, vol. 20, pp. 1–7, 8 2014.

[220] S. S. Setayandeh and A. Lohrasebi, "Influence of ghz electric fields on the mechanical properties of a microtubule," *Journal of Molecular Modeling*, vol. 21, pp. 1–7, 2015.

[221] K. R. Foster and J. W. Baish, "Viscous damping of vibrations in microtubules," *Journal of Biological Physics*, vol. 26, pp. 255–260, 2000.

[222] H. Jafari, M. H. Yazdi, and M. M. S. Fakhrabadi, "Damping effects on wave-propagation characteristics of microtubule-based bio-nano-metamaterials," *International Journal of Mechanical Sciences*, vol. 184, 10 2020.

[223] O. Kučera, D. Havelka, and M. Cifra, "Vibrations of microtubules: Physics that has not met biology yet," *Wave Motion*, vol. 72, pp. 13–22, 2017.

[224] E. D. Kirson, Z. Gurvich, R. Schneiderman, E. Dekel, A. Itzhaki, Y. Wasserman, R. Schatzberger, and Y. Palti, "Disruption of cancer cell replication by alternating electric fields," *Cancer research*, vol. 64, pp. 3288–3295, 5 2004.

[225] A. M. Davies, U. Weinberg, and Y. Palti, "Tumor treating fields: a new frontier in cancer therapy," *Annals of the New York Academy of Sciences*, vol. 1291, pp. 86–95, 7 2013.

[226] F. A. Carrieri, C. Smack, I. Siddiqui, L. R. Kleinberg, and P. T. Tran, "Tumor treating fields: At the crossroads between physics and biology for cancer treatment," *Frontiers in Oncology*, vol. 10, p. 1991, 10 2020.

[227] J. A. Tuszynski, C. Wenger, D. E. Friesen, and J. Preto, "An overview of sub-cellular mechanisms involved in the action of ttfields," *International Journal of Environmental Research and Public Health 2016, Vol. 13, Page 1128*, vol. 13, p. 1128, 11 2016.

[228] R. Penrose, *The Emperor's new mind*. Oxford University Press, 1989.

[229] R. Penrose, *The Shadows of the mind*. Oxford University Press, 1994.

[230] D. Chalmers, "Facing up to the problem of consciousness," *Journal of Consciousness Studies*, vol. 2, pp. 200–219, 1995.

[231] S. Hameroff and R. Penrose, "Consciousness in the universe: A review of the 'orch or' theory," *Physics of Life Reviews*, vol. 11, pp. 39–78, 2014.

[232] M. Tegmark, "Importance of quantum decoherence in brain processes," *Physical Review E*, vol. 61, p. 4194, 4 2000.

[233] T. J. Craddock, P. Kurian, J. Preto, K. Sahu, S. R. Hameroff, M. Klobukowski, and J. A. Tuszynski, "Anesthetic alterations of collective terahertz oscillations in tubulin correlate with clinical potency: Implications for anesthetic action and post-operative cognitive dysfunction," *Scientific Reports*, vol. 7, pp. 1–12, 2017.

[234] N. Lambert, Y. N. Chen, Y. C. Cheng, C. M. Li, G. Y. Chen, and F. Nori, "Quantum biology," *Nature Physics 2012 9:1*, vol. 9, pp. 10–18, 12 2012.

[235] E. Collini, C. Y. Wong, K. E. Wilk, P. M. Curmi, P. Brumer, and G. D. Scholes, "Coherently wired light-harvesting in photosynthetic marine algae at ambient temperature," *Nature 2010 463:7281*, vol. 463, pp. 644–647, 2 2010.

[236] J. Cao, R. J. Cogdell, D. F. Coker, H. G. Duan, J. Hauer, U. Kleinekathöfer, T. L. Jansen, T. Mančal, R. J. D. Miller, J. P. Ogilvie, V. I. Prokhorenko, T. Renger, H. S. Tan, R. Tempelaar, M. Thorwart, E. Thyrhaug, S. Westenhoff, and D. Zigmantas, "Quantum biology revisited," *Science Advances*, vol. 6, p. eaaz4888, 4 2020.

[237] H. W. Rathbone, J. A. Davis, K. A. Michie, S. C. Goodchild, N. O. Robertson, and P. M. Curmi, "Coherent phenomena in photosynthetic light harvesting: part two—observations in biological systems," *Biophysical Reviews*, vol. 10, p. 1443, 10 2018.

[238] A. Ourmazd, "Cryo-em, xfels and the structure conundrum in structural biology," *Nature Methods 2019 16:10*, vol. 16, pp. 941–944, 9 2019.

[239] S. C. Shoemaker and N. Ando, "X-rays in the cryo-electron microscopy era: Structural biology's dynamic future," *Biochemistry*, vol. 57, pp. 277–285, 1 2018.

[240] R. Dods, P. Båth, D. Arnlund, K. R. Beyerlein, G. Nelson, M. Liang, R. Harimoorthy, P. Berntsen, E. Malmerberg, L. Johansson, R. Andersson, R. Bosman, S. Carbajo, E. Claesson, C. E. Conrad, P. Dahl, G. Hammarin, M. S. Hunter, C. Li, S. Lisova, D. Milathianaki, J. Robinson, C. Safari, A. Sharma, G. Williams, C. Wickstrand, O. Yefanov, J. Davidsson, D. P. DePonte, A. Barty, G. Brändén, and R. Neutze, "From macrocrystals to microcrystals: A strategy for membrane protein serial crystallography," *Structure*, vol. 25, pp. 1461–1468.e2, 9 2017.

[241] P. Bath, A. Banacore, P. Börjesson, R. Bosman, C. Wickstrand, C. Safari, R. Dods, S. Ghosh, P. Dahl, G. Ortolani, T. B. Ulfarsdottir, G. Hammarin, M. G. Bonete, A. Vallejos, L. Ostojic, P. Edlund, J. B. Linse, R. Andersson, E. Nango, S. Owada, R. Tanaka, K. Tono, Y. Joti, O. Nureki, F. Luo, D. James, K. Nass, P. J. Johnson, G. Knopp, D. Ozerov, C. Cirelli, C. Milne, S. Iwata, G. Brändén, and R. Neutze, "Lipidic cubic phase serial femtosecond crystallography structure of a photosynthetic reaction centre," *Acta Crystallographica Section D: Structural Biology*, vol. 78, pp. 698–708, 6 2022.

[242] J. S. Fraser, K. Lindorff-Larsen, and M. Bonomi, "What will computational modeling approaches have to say in the era of atomistic cryo-em data?," *Journal of Chemical Information and Modeling*, vol. 60, pp. 2410–2412, 5 2020.

[243] L. V. Bock and H. Grubmüller, "Effects of cryo-em cooling on structural ensembles," *Nature Communications 2022 13:1*, vol. 13, pp. 1–13, 3 2022.

[244] A. Hosseinizadeh, G. Mashayekhi, J. Copperman, P. Schwander, A. Dashti, R. Sepehr, R. Fung, M. Schmidt, C. H. Yoon, B. G. Hogue, G. J. Williams, A. Aquila, and A. Ourmazd, "Conformational landscape of a virus by single-particle x-ray scattering," *Nature Methods 2017 14:9*, vol. 14, pp. 877–881, 8 2017.

[245] A. Doerr, "Diffraction before destruction," *Nature Methods 2011 8:4*, vol. 8, pp. 283–283, 3 2011.

[246] H. N. Chapman, C. Caleman, and N. Timneanu, "Diffraction before destruction," *Philosophical Transactions of the Royal Society B: Biological Sciences*, vol. 369, 7 2014.

[247] H. N. Chapman, A. Barty, M. J. Bogan, S. Boutet, M. Frank, S. P. Hau-Riege, S. Marchesini, B. W. Woods, S. Bajt, W. H. Benner, R. A. London, E. Plönjes, M. Kuhlmann, R. Treusch, S. Düsterer, T. Tschentscher, J. R. Schneider, E. Spiller, T. Möller, C. Bostedt, M. Hoener, D. A. Shapiro, K. O. Hodgson, D. V. D. Spoel, F. Burmeister, M. Bergh, C. Caleman, G. Huldt, M. M. Seibert, F. R. Maia, R. W. Lee, A. Szöke, N. Timneanu, and J. Hajdu, "Femtosecond diffractive imaging with a soft-x-ray free-electron laser," *Nature Physics 2006 2:12*, vol. 2, pp. 839–843, 11 2006.

[248] P. Emma, R. Akre, J. Arthur, R. Bionta, C. Bostedt, J. Bozek, A. Brachmann, P. Bucksbaum, R. Coffee, F. J. Decker, Y. Ding, D. Dowell, S. Edstrom, A. Fisher, J. Frisch, S. Gilevich, J. Hastings, G. Hays, P. Hering, Z. Huang, R. Iverson, H. Loos, M. Messerschmidt, A. Miahnahri, S. Moeller, H. D. Nuhn, G. Pile, D. Ratner, J. Rzepiela, D. Schultz, T. Smith, P. Stefan, H. Tompkins, J. Turner, J. Welch, W. White, J. Wu, G. Yocky, and J. Galayda, "First lasing and operation of an ångstrom-wavelength free-electron laser," *Nature Photonics 2010 4:9*, vol. 4, pp. 641–647, 8 2010.

[249] H. N. Chapman, P. Fromme, A. Barty, T. A. White, R. A. Kirian, A. Aquila, M. S. Hunter, J. Schulz, D. P. Deponte, U. Weierstall, R. B. Doak, F. R. Maia, A. V. Martin, I. Schlichting, L. Lomb, N. Coppola, R. L. Shoeman, S. W. Epp, R. Hartmann, D. Rolles, A. Rudenko, L. Foucar, N. Kimmel, G. Weidenspointner, P. Holl, M. Liang, M. Barthelmess, C. Caleman, S. Boutet, M. J. Bogan, J. Krzywinski, C. Bostedt, S. Bajt, L. Gumprecht, B. Rudek, B. Erk, C. Schmidt, A. Hömke, C. Reich, D. Pietschner, L. Ströder, G. Hauser, H. Gorke, J. Ullrich, S. Herrmann, G. Schaller, F. Schopper, H. Soltau, K. U. Kühnel, M. Messerschmidt, J. D. Bozek, S. P. Hau-Riege, M. Frank, C. Y. Hampton, R. G. Sierra, D. Starodub, G. J. Williams, J. Hajdu, N. Timneanu, M. M. Seibert, J. Andreasson, A. Rocker, O. Jönsson, M. Svenda, S. Stern,

K. Nass, R. Andritschke, C. D. Schröter, F. Krasniqi, M. Bott, K. E. Schmidt, X. Wang, I. Grotjohann, J. M. Holton, T. R. Barends, R. Neutze, S. Marchesini, R. Fromme, S. Schorb, D. Rupp, M. Adolph, T. Gorkhover, I. Andersson, H. Hirsemann, G. Potdevin, H. Graafsma, B. Nilsson, and J. C. Spence, "Femtosecond x-ray protein nanocrystallography," *Nature 2011 470:7332*, vol. 470, pp. 73–77, 2 2011.

[250] S. Boutet, L. Lomb, G. J. Williams, T. R. Barends, A. Aquila, R. B. Doak, U. Weierstall, D. P. DePonte, J. Steinbrener, R. L. Shoeman, M. Messerschmidt, A. Barty, T. A. White, S. Kassemeyer, R. A. Kirian, M. M. Seibert, P. A. Montanez, C. Kenney, R. Herbst, P. Hart, J. Pines, G. Haller, S. M. Gruner, H. T. Philipp, M. W. Tate, M. Hromalik, L. J. Koerner, N. V. Bakel, J. Morse, W. Ghonsalves, D. Arnlund, M. J. Bogan, C. Caleman, R. Fromme, C. Y. Hampton, M. S. Hunter, L. C. Johansson, G. Katona, C. Kupitz, M. Liang, A. V. Martin, K. Nass, L. Redecke, F. Stellato, N. Timneanu, D. Wang, N. A. Zatsepin, D. Schafer, J. Defever, R. Neutze, P. Fromme, J. C. Spence, H. N. Chapman, and I. Schlichting, "High-resolution protein structure determination by serial femtosecond crystallography," *Science*, vol. 337, pp. 362–364, 7 2012.

[251] A. Munke, J. Andreasson, A. Aquila, S. Awel, K. Ayyer, A. Barty, R. J. Bean, P. Berntsen, J. Bielecki, S. Boutet, M. Bucher, H. N. Chapman, B. J. Daurer, H. Demirci, V. Elser, P. Fromme, J. Hajdu, M. F. Hantke, A. Higashiura, B. G. Hogue, A. Hosseinizadeh, Y. Kim, R. A. Kirian, H. K. Reddy, T. Y. Lan, D. S. Larsson, H. Liu, N. D. Loh, F. R. Maia, A. P. Mancuso, K. Mühlig, A. Nakagawa, D. Nam, G. Nelson, C. Nettelblad, K. Okamoto, A. Ourmazd, M. Rose, G. V. D. Schot, P. Schwander, M. M. Seibert, J. A. Sellberg, R. G. Sierra, C. Song, M. Svenda, N. Timneanu, I. A. Vartanyants, D. Westphal, M. O. Wiedorn, G. J. Williams, P. L. Xavier, C. H. Yoon, and J. Zook, "Coherent diffraction of single rice dwarf virus particles using hard x-rays at the linac coherent light source," *Scientific Data 2016 3:1*, vol. 3, pp. 1–12, 8 2016.

[252] T. Ekeberg, M. Svenda, C. Abergel, F. R. Maia, V. Seltzer, J. M. Claverie, M. Hantke, O. Jönsson, C. Nettelblad, G. V. D. Schot, M. Liang, D. P. Deponte, A. Barty, M. M. Seibert, B. Iwan, I. Andersson, N. D. Loh, A. V. Martin, H. Chapman, C. Bostedt, J. D. Bozek, K. R. Ferguson, J. Krzywinski, S. W. Epp, D. Rolles, A. Rudenko, R. Hartmann, N. Kimmel, and J. Hajdu, "Three-dimensional reconstruction of the giant mimivirus particle with an x-ray free-electron laser," *Physical Review Letters*, vol. 114, p. 098102, 3 2015.

[253] Y. Kim, C. Kim, O. Y. Kwon, D. Nam, S. S. Kim, J. H. Park, S. Kim, M. Gallagher-Jones, Y. Kohmura, T. Ishikawa, C. Song, G. Tae, and D. Y. Noh, "Visualization of a mammalian mitochondrion by coherent x-ray diffractive imaging," *Scientific Reports 2017 7:1*, vol. 7, pp. 1–9, 5 2017.

[254] D. Popp, N. D. Loh, H. Zorgati, U. Ghoshdastider, L. T. Liow, M. I. Ivanova, M. Larsson, D. P. DePonte, R. Bean, K. R. Beyerlein, C. Gati, D. Oberthuer, D. Arnlund, G. Brändén, P. Berntsen, D. Cascio, L. M. G. Chavas, J. P. J. Chen, K. Ding, H. Fleckenstein, L. Gumprecht, R. Harimoorthy, E. Mossou, M. R. Sawaya, A. S. Brewster, J. Hattne, N. K. Sauter, M. Seibert, C. Seuring, F. Stellato, T. Tilp, D. S. Eisenberg, M. Messerschmidt, G. J. Williams, J. E. Koglin, L. Makowski, R. P. Millane, T. Forsyth, S. Boutet, T. A. White, A. Barty, H. Chapman, S. L. Chen, M. Liang, R. Neutze, and R. C. Robinson, "Flow-aligned, single-shot fiber diffraction using a femtosecond x-ray free-electron laser," *Cytoskeleton*, vol. 74, pp. 472–481, 12 2017.

[255] I. V. Lundholm, J. A. Sellberg, T. Ekeberg, M. F. Hantke, K. Okamoto, G. V. D. Schot, J. Andreasson, A. Barty, J. Bielecki, P. Bruza, M. Bucher, S. Carron, B. J. Daurer, K. Ferguson, D. Hasse, J. Krzywinski, D. S. Larsson, A. Morgan, K. Mühlig, M. Müller, C. Nettelblad, A. Pietrini, H. K. Reddy, D. Rupp, M. Sauppe, M. Seibert, M. Svenda, M. Swiggers, N. Timneanu, A. Ulmer, D. Westphal, G. Williams, A. Zani, G. Faigel, H. N. Chapman, T. Möller, C. Bostedt, J. Hajdu, T. Gorkhover, and F. R. Maia, "Considerations for three-dimensional image reconstruction from experimental data in coherent diffractive imaging," *IUCrJ*, vol. 5, pp. 531–541, 9 2018.

[256] W. Cochran, F. Crick, V. Vand, and IUCr, "The structure of synthetic polypeptides. i. the transform of atoms on a helix," *urn:issn:0365-110X*, vol. 5, pp. 581–586, 9 1952.

[257] J. D. Watson and F. H. Crick, "Molecular structure of nucleic acids: A structure for deoxyribose nucleic acid," *Nature 1953 171:4356*, vol. 171, pp. 737–738, 4 1953.

[258] R. E. Franklin and R. G. Gosling, "Molecular configuration in sodium thymonucleate," *Nature*, vol. 171, pp. 740–741, 1953.

[259] B. Maddox, "The double helix and the 'wronged heroine'," *Nature 2003 421:6921*, vol. 421, pp. 407–408, 1 2003.

[260] G. B. Jeffery, "The motion of ellipsoidal particles immersed in a viscous fluid," *Proceedings of the Royal Society of London. Series A, Containing Papers of a Mathematical and Physical Character*, vol. 102, pp. 161–179, 11 1922.

[261] S. Boutet and G. J. Williams, "The coherent x-ray imaging (cxi) instrument at the linac coherent light source (lcls)," *New Journal of Physics*, vol. 12, p. 035024, 3 2010.

[262] A. Barty, R. A. Kirian, F. R. Maia, M. Hantke, C. H. Yoon, T. A. White, and H. Chapman, "Cheetah: software for high-throughput reduction and analysis of serial femtosecond x-ray diffraction data," *urn:issn:1600-5767*, vol. 47, pp. 1118–1131, 5 2014.

[263] S. H. Scheres, R. Núñez-Ramírez, C. O. Sorzano, J. M. Carazo, and R. Marabini, "Image processing for electron microscopy single-particle analysis using xmipp," *Nature Protocols 2008 3:6*, vol. 3, pp. 977–990, 5 2008.

[264] C. O. Sorzano, R. Marabini, J. Velázquez-Muriel, J. R. Bilbao-Castro, S. H. Scheres, J. M. Carazo, and A. Pascual-Montano, "Xmipp: a new generation of an open-source image processing package for electron microscopy," *Journal of Structural Biology*, vol. 148, pp. 194–204, 11 2004.

[265] The Mathworks, Inc., Natick, Massachusetts, *MATLAB version (R2018b)*, 2018.

[266] E. H. Kellogg, N. M. Hejab, S. Howes, P. Northcote, J. H. Miller, J. F. Díaz, K. H. Downing, and E. Nogales, "Insights into the distinct mechanisms of action of taxane and non-taxane microtubule stabilizers from cryo-em structures," *Journal of Molecular Biology*, vol. 429, pp. 633–646, 3 2017.

[267] R. H. Wade, D. Chrétien, and D. Job, "Characterization of microtubule protofilament numbers: How does the surface lattice accommodate?," *Journal of Molecular Biology*, vol. 212, pp. 775–786, 4 1990.

[268] R. Harimoorthy, *Effect of microwaves on microtubule structure and function probed by light and x-ray scattering*. PhD thesis, University of Gothenburg, 2018.

[269] O. Kučera and M. Cifra, "Radiofrequency and microwave interactions between biomolecular systems," *Journal of Biological Physics 2015 42:1*, vol. 42, pp. 1–8, 7 2015.

[270] H. Fröhlich, "The biological effects of microwaves and related questions," *Advances in Electronics and Electron Physics*, vol. 53, pp. 85–152, 1 1980.

[271] R. K. Adair, "Biophysical limits on athermal effects of rf and microwave radiation," *Bioelectromagnetics*, vol. 24, pp. 39–48, 2003.

[272] W. H. G E.P. Box, J.S. Hunter, *Statistics for experimenters. Design, Innovation and Discovery. S.E.* Wiley, 2005.

[273] M. J. Ortner, M. J. Galvin, and R. D. Irwin, "The effect of 2450-mhz microwave radiation during microtubular polymerization in vitro," *Radiation Research*, vol. 93, pp. 353–363, 2 1983.

[274] P. Reineck, C. J. Wienken, and D. Braun, "Thermophoresis of single stranded dna," *Electrophoresis*, vol. 31, pp. 279–286, 2010.

[275] J. H. Liu, K. C. Hsia, R. Yokokawa, and Y. W. Lu, "Microtubule polymerization in alignment by an on-chip temperature gradient platform," *Sensors and Actuators B: Chemical*, vol. 298, p. 126813, 11 2019.

[276] H. W. Bergh, E. S. W. Simpson, J. G. Sclater, B. Parsons, I. W. . Norton, B. E. Tucholke, G. B. . J. L. Carpenter, D. V. Kent, and S. C. Cande, "X-ray kinetic studies of microtubule assembly using synchrotron radiation," *Nature 1980 287:5783*, vol. 287, pp. 595–599, 1980.

[277] O. Berntsson, R. P. Diensthuber, M. R. Panman, A. Björling, E. Gustavsson, M. Hoernke, A. J. Hughes, L. Henry, S. Niebling, H. Takala, J. A. Ihalainen, G. Newby, S. Kerruth, J. Heberle, M. Liebi, A. Menzel, R. Henning, I. Kosheleva, A. Möglich, and S. Westenhoff, "Sequential conformational transitions and α-helical supercoiling regulate a sensor histidine kinase," *Nature Communications 2017 8:1*, vol. 8, pp. 1–8, 8 2017.

[278] D. Sarabi, L. Ostojić, R. Bosman, A. Vallejos, J.-B. Linse, M. Wulff, M. Levantino, and R. Neutze, "Modeling difference x-ray scattering observations from an integral membrane protein within a detergent micelle," *Structural Dynamics*, vol. 9, p. 054102, 10 2022.

[279] A. G. Kikhney and D. I. Svergun, "A practical guide to small angle x-ray scattering (saxs) of flexible and intrinsically disordered proteins," *FEBS Letters*, vol. 589, pp. 2570–2577, 9 2015.

[280] D. Schneidman-Duhovny, M. Hammel, J. A. Tainer, and A. Sali, "Foxs, foxsdock and multifoxs: Single-state and multi-state structural modeling of proteins and their complexes based on saxs profiles," *Nucleic Acids Research*, vol. 44, pp. W424–W429, 7 2016.

[281] D. Schneidman-Duhovny, M. Hammel, J. A. Tainer, and A. Sali, "Accurate saxs profile computation and its assessment by contrast variation experiments," *Biophysical journal*, vol. 105, pp. 962–974, 8 2013.

[282] M. Trebbin, D. Steinhauser, J. Perlich, A. Buffet, S. V. Roth, W. Zimmermann, J. Thiele, and S. Förster, "Anisotropic particles align perpendicular to the flow direction in narrow microchannels," *Proceedings of the National Academy of Sciences of the United States of America*, vol. 110, pp. 6706–6711, 4 2013.

[283] P. T. Corona, B. Berke, M. Guizar-Sicairos, L. G. Leal, M. Liebi, and M. E. Helgeson, "Fingerprinting soft material nanostructure response to complex flow histories," *Physical Review Materials*, vol. 6, p. 045603, 4 2022.

[284] T. Sugiyama, D. Miyashiro, D. Takao, H. Iwamoto, Y. Sugimoto, K. Wakabayashi, and S. Kamimura, "Quick shear-flow alignment of biological filaments for x-ray fiber diffraction facilitated by methylcellulose," *Biophysical Journal*, vol. 97, pp. 3132–3138, 12 2009.

[285] V. Lutz-Bueno, J. Zhao, R. Mezzenga, T. Pfohl, P. Fischer, and M. Liebi, "Scanning-saxs of microfluidic flows: nanostructural mapping of soft matter," *Lab on a Chip*, vol. 16, pp. 4028–4035, 10 2016.

[286] S. W. NT Nguyen, *Funamentals and applications of microfluidics. S.E.* Artech House integrated microsystems series, 2006.

[287] R. R. Ramalho, H. Soares, and L. V. Melo, "Microtubule behavior under strong electromagnetic fields," *Materials Science and Engineering: C*, vol. 27, pp. 1207–1210, 9 2007.

[288] K. R. Foster, "Thermal and nonthermal mechanisms of interaction of radio-frequency energy with biological systems," *IEEE Transactions on Plasma Science*, vol. 28, pp. 15–23, 2000.

[289] C. Daniells, I. Duce, D. Thomas, P. Sewell, J. Tattersall, and D. D. Pomerai, "Transgenic nematodes as biomonitors of microwave-induced stress," *Mutation Research/Fundamental and Molecular Mechanisms of Mutagenesis*, vol. 399, pp. 55–64, 3 1998.

[290] D. D. Pomerai, C. Daniells, H. David, J. Allan, I. Duce, M. Mutwakil, D. Thomas, P. Sewell, J. Tattersall, D. Jones, and P. Candido, "Non-thermal heat-shock response to microwaves," *Nature 2000 405:6785*, vol. 405, pp. 417–418, 5 2000.

[291] D. D. Pomerai, C. Daniells, H. David, J. Allan, L. Duce, M. Mutwakil, and D. Thomas, "Microwave radiation induces a heat-shock response and enhances growth in the nematode caenorhabditis elegans," *IEEE Transactions on Microwave Theory and Techniques*, vol. 48, pp. 2076–2081, 2000.

[292] A. S. Dawe, B. Smith, D. W. Thomas, S. Greedy, N. Vasic, A. Gregory, B. Loader, and D. I. D. Pomerai, "A small temperature rise may contribute towards the apparent induction by microwaves of heat-shock gene expression in the nematode caenorhabditis elegans," *Bioelectromagnetics*, vol. 27, pp. 88–97, 2 2006.

[293] P. Bhartiya, S. Mumtaz, J. S. Lim, N. Kaushik, P. Lamichhane, L. N. Nguyen, J. H. Jang, S. H. Yoon, J. J. Choi, N. K. Kaushik, and E. H. Choi, "Pulsed 3.5 ghz high power microwaves irradiation on physiological solution and their biological evaluation on human cell lines," *Scientific Reports 2021 11:1*, vol. 11, pp. 1–16, 4 2021.

[294] M. Damm, C. Nusshold, D. Cantillo, G. N. Rechberger, K. Gruber, W. Sattler, and C. O. Kappe, "Can electromagnetic fields influence the structure and enzymatic digest of proteins? a critical evaluation of microwave-assisted proteomics protocols," *Journal of Proteomics*, vol. 75, pp. 5533–5543, 10 2012.

[295] H. Han, E. Round, R. Schubert, Y. Gul, J. Makroczyova, D. Meza, P. Heuser, M. Aepfelbacher, I. Barak, C. Betzel, P. Fromme, I. Kursula, P. Nissen, E. Tereschenko, J. Schulz, C. Uetrecht, J. U. M. Wilmanns, J. Hajdu, V. S. Lamzi, and K. Lorenzen, "The xbi biolab for life science experiments at the european xfel han huijong," *Journal of Applied Crystallography*, vol. 54, pp. 7–21, 2 2021.

[296] E. Sobolev, S. Zolotarev, K. Giewekemeyer, J. Bielecki, K. Okamoto, H. K. Reddy, J. Andreasson, K. Ayyer, I. Barak, S. Bari, A. Barty, R. Bean, S. Bobkov, H. N. Chapman, G. Chojnowski, B. J. Daurer, K. Dörner, T. Ekeberg, L. Flückiger, O. Galzitskaya, L. Gelisio, S. Hauf, B. G. Hogue, D. A. Horke, A. Hosseinizadeh, V. Ilyin, C. Jung, C. Kim, Y. Kim, R. A. Kirian, H. Kirkwood, O. Kulyk, J. Küpper, R. Letrun, N. D. Loh, K. Lorenzen, M. Messerschmidt, K. Mühlig, A. Ourmazd, N. Raab, A. V. Rode, M. Rose, A. Round, T. Sato, R. Schubert, P. Schwander, J. A. Sellberg, M. Sikorski, A. Silenzi, C. Song, J. C. Spence, S. Stern, J. Sztuk-Dambietz, A. Teslyuk, N. Timneanu, M. Trebbin, C. Uetrecht, B. Weinhausen, G. J. Williams, P. L. Xavier, C. Xu, I. A. Vartanyants, V. S. Lamzin, A. Mancuso, and F. R. Maia, "Megahertz single-particle imaging at the european xfel," *Communications Physics 2020 3:1*, vol. 3, pp. 1–11, 5 2020.

[297] C. A. Stan, D. Milathianaki, H. Laksmono, R. G. Sierra, T. A. McQueen, M. Messerschmidt, G. J. Williams, J. E. Koglin, T. J. Lane, M. J. Hayes, S. A. Guillet, M. Liang, A. L. Aquila, P. R. Willmott, J. S. Robinson, K. L. Gumerlock, S. Botha, K. Nass, I. Schlichting, R. L. Shoeman, H. A. Stone, and S. Boutet, "Liquid explosions induced by x-ray laser pulses," *Nature Physics 2016 12:10*, vol. 12, pp. 966–971, 5 2016.

[298] M. L. Grünbein, A. Gorel, L. Foucar, S. Carbajo, W. Colocho, S. Gilevich, E. Hartmann, M. Hilpert, M. Hunter, M. Kloos, J. E. Koglin, T. J. Lane, J. Lewandowski, A. Lutman, K. Nass, G. N. Kovacs, C. M. Roome, J. Sheppard, R. L. Shoeman, M. Stricker, T. van Driel, S. Vetter, R. B. Doak, S. Boutet, A. Aquila, F. J. Decker, T. R. Barends, C. A. Stan, and I. Schlichting, "Effect of x-ray free-electron laser-induced shockwaves on haemoglobin microcrystals delivered in a liquid jet," *Nature Communications 2021 12:1*, vol. 12, pp. 1–11, 3 2021.

[299] G. Brändén, G. Hammarin, R. Harimoorthy, A. Johansson, D. Arnlund, E. Malmerberg, A. Barty, S. Tångefjord, P. Berntsen, D. P. DePonte, C. Seuring, T. A. White, F. Stellato, R. Bean, K. R. Beyerlein, L. M. G. Chavas, H. Fleckenstein, C. Gati, U. Ghoshdastider, L. Gumprecht, D. Oberthür, D. Popp, M. Seibert, T. Tilp, M. Messerschmidt, G. J. Williams, N. D. Loh, H. N. Chapman, P. Zwart, M. Liang, S. Boutet, R. C. Robinson, and R. Neutze, "Coherent diffractive imaging of microtubules using an x-ray laser," *Nature Communications*, vol. 10, p. 2589, 12 2019.

[300] A. Peck, H. Y. Chang, A. Dujardin, D. Ramalingam, M. Uervirojnangkoorn, Z. Wang, A. Mancuso, F. Poitevin, and C. H. Yoon, "Skopi: A simulation package for diffractive imaging of non-crystalline biomolecules," *Journal of Applied Crystallography*, vol. 55, pp. 1002–1010, 8 2022.

[301] K. Ayyer, K. Ayyer, K. Ayyer, P. L. Xavier, P. L. Xavier, P. L. Xavier, J. Bielecki, Z. Shen, B. J. Daurer, A. K. Samanta, S. Awel, R. Bean, A. Barty, M. Bergemann, T. Ekeberg, A. D. Estillore, H. Fangohr, K. Giewekemeyer, M. S. Hunter, M. Karnevskiy, R. A. Kirian, H. Kirkwood, Y. Kim, J. Koliyadu, H. Lange, H. Lange, R. Letrun, J. Lübke, J. Lübke, J. Lübke, T. Michelat, A. J. Morgan, N. Roth, N. Roth, T. Sato, M. Sikorski, F. Schulz, J. C. H. Spence, P. Vagovic, P. Vagovic, T. Wollweber, T. Wollweber, T. Wollweber, L. Worbs, L. Worbs, O. Yefanov, Y. Zhuang, Y. Zhuang, F. R. N. C. Maia, F. R. N. C. Maia, D. A. Horke, D. A. Horke, D. A. Horke, J. Küpper, J. Küpper, J. Küpper, J. Küpper, N. D. Loh, N. D. Loh, A. P. Mancuso, A. P. Mancuso, H. N. Chapman, H. N. Chapman, and H. N. Chapman, "3d diffractive imaging of nanoparticle ensembles using an x-ray laser," *Optica, Vol. 8, Issue 1, pp. 15-23*, vol. 8, pp. 15–23, 1 2021.

[302] A. Ourmazd, K. Moffat, and E. E. Lattman, "Structural biology is solved — now what?," *Nature Methods 2022 19:1*, vol. 19, pp. 24–26, 1 2022.

[303] J. Jumper, R. Evans, A. Pritzel, T. Green, M. Figurnov, O. Ronneberger, K. Tunyasuvunakool, R. Bates, A. Žídek, A. Potapenko, A. Bridgland, C. Meyer, S. A. Kohl, A. J. Ballard, A. Cowie, B. Romera-Paredes, S. Nikolov, R. Jain, J. Adler, T. Back, S. Petersen, D. Reiman, E. Clancy, M. Zielinski, M. Steinegger, M. Pacholska, T. Berghammer, S. Bodenstein, D. Silver, O. Vinyals, A. W. Senior, K. Kavukcuoglu, P. Kohli, and D. Hassabis, "Highly accurate protein structure prediction with alphafold," *Nature 2021 596:7873*, vol. 596, pp. 583–589, 7 2021.

[304] H. B. Guo, A. Perminov, S. Bekele, G. Kedziora, S. Farajollahi, V. Varaljay, K. Hinkle, V. Molinero, K. Meister, C. Hung, P. Dennis, N. Kelley-Loughnane, and R. Berry, "Alphafold2 models indicate that protein sequence determines both structure and dynamics," *Scientific Reports 2022 12:1*, vol. 12, pp. 1–15, 6 2022.

[305] D. S. Cerutti and D. A. Case, "Molecular dynamics simulations of macromolecular crystals," *Wiley interdisciplinary reviews. Computational molecular science*, vol. 9, 7 2019.

[306] H. Poddar, D. J. Heyes, G. Schirò, M. Weik, D. Leys, and N. S. Scrutton, "A guide to time-resolved structural analysis of light-activated proteins," *The FEBS Journal*, vol. 289, pp. 576–595, 2 2022.

[307] B. V. Ardenne, M. Mechelke, and H. Grubmüller, "Structure determination from single molecule x-ray scattering with three photons per image," *Nature Communications*, vol. 9, pp. 1–9, 2018.

[308] R. W. Schoenlein, S. Boutet, M. P. Minitti, and A. M. Dunne, "The linac coherent light source: Recent developments and future plans," *Applied Sciences 2017, Vol. 7, Page 850*, vol. 7, p. 850, 8 2017.

[309] T. Ekeberg, D. Assalauova, J. Bielecki, R. Boll, B. J. Daurer, L. A. Eichacker, L. E. Franken, D. E. Galli, L. Gelisio, L. Gumprecht, L. H. Gunn, J. Hajdu, R. Hartmann, D. Hasse, A. Ignatenko, J. Koliyadu, O. Kulyk, R. Kurta, M. Kuster, W. Lugmayr, J. Lübke, A. P. Mancuso, T. Mazza, C. Nettelblad, Y. Ovcharenko, D. E. Rivas, A. K. Samanta, P. Schmidt, E. Sobolev, N. Timneanu, S. Usenko, D. Westphal, T. Wollweber, L. Worbs, P. L. Xavier, H. Yousef, K. Ayyer, H. N. Chapman, J. A. Sellberg, C. Seuring, I. A. Vartanyants, J. Küpper, M. Meyer, and F. R. Maia, "Observation of a single protein by ultrafast x-ray diffraction," *bioRxiv*, p. 2022.03.09.483477, 11 2022.

"We climbed this hill. Each step up we could see farther, so of course we kept going. Now we're at the top. Science has been at the top for a few centuries now. And we look out across the plain and we see this other tribe dancing around above the clouds, even higher than we are. Maybe it's a mirage, maybe it's a trick. Or maybe they just climbed a higher peak we can't see because the clouds are blocking the view. So we head off to find out—but every step takes us downhill. No matter what direction we head, we can't move off our peak without losing our vantage point. So we climb back up again. We're trapped on a local maximum. But what if there is a higher peak out there, way across the plain? The only way to get there is to bite the bullet, come down off our foothill and trudge along the riverbed until we finally start going uphill again. And it's only then you realize: Hey, this mountain reaches way higher than that foothill we were on before, and we can see so much better from up here. But you can't get there unless you leave behind all the tools that made you so successful in the first place. You have to take that first step downhill."

Peter Watts, *Echopraxia*